

CONTENTS

INTRODUCTION	1
i MUOGRAPHY: PHYSICS, PRINCIPLES AND DETECTORS	2
1 IMAGING WITH μ PARTICLES	4
1.1 Cosmic Rays	5
1.2 Flux of Muons at the sea level	6
1.3 Energy Loss of Muons into the Matter	8
1.4 Modeling the Muons Flux	11
1.5 Technique for Muon Radiography with Cosmic Muons	13
2 THE STATE OF ART OF DETECTORS FOR THE MUOGRAPHY	18
2.1 Requirements of a Detector for the Muon Radiography	20
2.2 Background's Rejection as a Further Requirement	21
2.3 Detectors in Muography	22
2.3.1 Japanese Detectors	22
2.3.1.1 PAC System at Mt. Asama.	25
2.3.1.2 Emulsion Chamber Detector at Mt. Asama and Mt. Usu.	25
2.3.2 DIAPHANE: RaCoon and MusTang telescopes	26
2.3.3 TOMUVOL Muon Tracker	27
ii THE MU-RAY MOUN TELESCOPE	30
3 DETECTOR DESIGN, CONSTRUCTION AND PERFORMANCES	32
3.1 The Basic Module	34
3.2 Mounting Modules on the Chassis	35
3.3 The Silicon Photomultipliers	37
3.4 Hybrid Board for SiPMs	40
3.5 Temperature Control of the SiPMs	40
3.6 Front-end Electronics and Data Acquisition System	43
3.7 Performances and Characterization of the Detector	44
3.8 The Remote Automated System MuBot	46
3.9 Campaigns at Mt. Vesuvius and at the Puy de Dôme	47
4 TECHNOLOGY	51
4.1 Front-end Electronic Upgrades	51
4.1.1 Improvements to the Slave Boards	51
4.1.2 The Master Board-RPi Direct Link	54
4.2 Measure of the Time of Flight	54
4.2.1 The TOF model	54
4.2.2 A simple toy Monte Carlo for the TOF model	57
4.3 Peltier Cells Temperature Control System	62
CONCLUSIONS	68
iii APPENDIX	72
LISTINGS	73
1 muDog.py	73

2	simulazioneDetectorMod.cpp	77
3	MuBotIRQ.c	81
4	map.h	84

LIST OF FIGURES

Figure 1.1	Energy Spectrum of Muons at 0° and 90°	4
Figure 1.2	Example of a diagram of cosmic rays shower.	6
Figure 1.3	Cosmic rays flux as a function of energy.	7
Figure 1.4	The angles θ and θ^* formed by an incoming muon, respectively, with the normal axis to the earth surface and with the normal axis to the top of the atmosphere.	8
Figure 1.5	Stopping power vs kinetic energy diagram of e^\mp on Iron.	9
Figure 1.6	Stopping power vs kinetic energy diagram of muon on Cu.	10
Figure 1.7	Probability Distribution Function of Muons at $45^\circ < \theta < 90^\circ$	11
Figure 1.8	Modified Gaisser model fitting experimental data.	12
Figure 1.9	Trends of the ratio between the flux at different altitudes h and the flux at sea level as a function of the muons energy.	14
Figure 1.10	Schematic measurement of the <i>free sky</i> flux by means of the backward flux.	15
Figure 1.11	Integrated flux of cosmic-ray muons at various zenith angles penetrating through a given thickness of rock with a density of 2.5 g/cm^3	16
Figure 2.1	Muography obtained at Mt. Asama with electronic detector in 2003 and with emulsion in 2007.	18
Figure 2.2	La Soufrière de Guadeloupe radiography	19
Figure 2.3	Tracking capability and background rejection of a muon detector.	21
Figure 2.4	Schematic of a photomultiplier tube.	23
Figure 2.5	Experimental measurement of the gain of a repaired Hamamatsu PMT.	24
Figure 2.6	Analysis of tracks in OPERA emulsions.	24
Figure 2.7	Detectors used by Japanese researchers.	25
Figure 2.8	DIAPHANE detector.	26
Figure 2.9	Schematic of a GRPC.	27
Figure 2.10	Map of the scaled transmission through the Puy de Dôme [Carloganu 2013].	28
Figure 2.11	The TOMUVOL detector.	28
Figure 3.1	Glue's defects.	33
Figure 3.2	Mu-Ray detector featured materials.	34
Figure 3.3	Mu-Ray detector assembly.	35
Figure 3.4	rontal view of the Mu-Ray detector.	36
Figure 3.5	Lateral view of the Mu-Ray detector.	36
Figure 3.6	SiPM inner structure.	37
Figure 3.7	SiPM produced by FBK-IRST.	39
Figure 3.8	Experimental dark counts rate in function of the discriminator threshold for different overvoltages.	39
Figure 3.9	Dark counts rate in function of the overvoltage for different temperature.	39
Figure 3.10	Temperature Local Monitoring Board.	40

Figure 3.11	Top and bottom view of the heat exchanger. It was realized gluing with Araldite an Inox bar with a copper base. The upper part and all sides are caulked with Armaflex insulator.	41
Figure 3.12	Hydraulic heat exchanger.	41
Figure 3.13	Plot of the SiPMs temperature versus the temperature set by the chiller.	41
Figure 3.14	Plot of the temperature when the system moves to room temperature, without thermal conditioning.	42
Figure 3.15	Laboratory tests for the reliability of the cooling system.	42
Figure 3.16	The Mu-Ray front-end electronic boards.	43
Figure 3.17	The Mu-Ray detector's planes have been mounted in horizontal to make a precise calibration of the detector.	44
Figure 3.18	Chart of the overall trigger efficiency of the detector.	45
Figure 3.19	The comparison between the measured flux of muons as a function of the zenith angle and the expected one assuming the $\cos^2\theta$ dependence of the flux on the zenith angle.	46
Figure 3.20	Logical schema of the remote automated system MuBot.	47
Figure 3.21	Some parts of the remote automatic system used at the Puy de Dôme.	47
Figure 3.22	The transmission map of the Vesuvius.	48
Figure 3.23	Trigger rate during data acquisition at the Puy de Dôme.	48
Figure 3.24	The rate of golden tracks.	49
Figure 3.25	The transmission map of the Puy de Dôme.	49
Figure 4.1	8 bit DAC and slow shaper time constant responses in function of the slow control register settings	52
Figure 4.2	Example of the time expansion technique.	53
Figure 4.3	Plot of the experimental data of the sizing of the time expansion circuit.	53
Figure 4.4	The Raspberry Pi wired in direct link to the master board.	54
Figure 4.5	Example of the trajectories and directions of the muons crossing a 2 planes detector.	56
Figure 4.6	TOF model expected distributions.	56
Figure 4.7	Simulated histograms of events with respect of azimuth and zenith angles.	58
Figure 4.8	Simulated histogram of the number of events recorded in each bin.	58
Figure 4.9	Comparison between counts distributions in 4 planes trigger logic and 2 planes trigger logic.	60
Figure 4.10	Reconstructed counts distributions in a 2 planes trigger logic for horizontal tracks.	61
Figure 4.11	Reconstructed counts distributions in a 2 planes trigger logic for transverse tracks.	61
Figure 4.12	Reconstructed counts distributions for the plane in a 4 planes trigger logic for transverse tracks.	62
Figure 4.14	Experimental setup used for the measure of the temperature during a Peltier cells test.	64
Figure 4.15	Arrangement of the temperature sensors on the SiPM housing pad.	65
Figure 4.16	Different models of Peltier cells.	65
Figure 4.17	The temperature control system mounted on the dummy module.	66

Figure 4.18 Chart of the ΔT_{env} in function of the electric power. 67

INTRODUCTION

The muon radiography, or muography, is an example of how the high energy physics can be used for technological purposes. From the experience acquired since the discovery of the cosmic rays, in particular of the muon, scientists tried to take advantage of the high penetrating power of this radiation to look inside large objects.

The first attempt to use the high penetrating power of muons dates back to the late '60, when Luis Alvarez try to measure the absorption of these particles through the Chephren's pyramid. He was searching for an unknown burial chamber and the proof of its existence would be manifested by the presence of a "dark spot" in the reconstructed data, related to a greater flow of muons in that area. He didn't succeed in the discovery of the hidden chamber, but this trial shown the feasibility of a technique that is based on the measure of the cosmic muons inside the matter.

The intuition of Alvarez was, probably, the first contribution to the technique today known as muon radiography. Since the early years of the new millennium, work on this technique have increased mainly due to the possibility of applying the muon radiography in the field of geology and volcanology. The advantage of this new methodology is to provide direct images of the interior of the geological structures, while traditional methods provide indirect measures of the physical quantities of interest.

The first chapter will be dedicated to the understanding of muons capability to pass through matter. The Energy spectrum of the muons of cosmic origin is very wide and the intensity of the flux varies a lot in function of the zenith angle. Since the discovery of the muon, physicists had well understand its phenomenology and have formulated different models that take into account the production of muons starting from their parents, the dependence of the flux of muons from the zenith and azimuth angles, the physics of muons depending on their energy, the modulation of the flux in function of the solar activity, the dependence on the altitude of the point of observation. The formulation of models that include these phenomena, allows to better study the interaction of muons with matter and, according to this, evaluates the expectations.

In the case of the horizontal flux, *i.e.* the flux we measure when our target is a volcano, the expected rate pointing a muon detector with sensitive area of 1 m^2 to the free sky, is only $\sim 4 \text{ Hz}$ and the rate expected pointing the volcano is $\sim 1 \text{ Hz}$. On the contrary, these few muons have enough energy to be detected beyond the geological edifice. Thus, the detectors for muography must have the necessary features to be as efficient as possible to detect this faint flux. In the second chapter, we will discuss how scientists have until today designed the detectors for the muon radiography and what were the results achieved.

Both electronic detector and nuclear emulsion chambers have been used. The latter allows for impressive resolution but present different problems when used outdoor and, moreover, the reconstruction of the tracks is often difficult to do. The electronic detectors

are more suitable for this kind of employment and, differently from the emulsion chambers, they are real time system. The real time capability allows for the quality check of the data acquisition, in order to act quickly if and when needed. Electronic detectors have been improved during years and step by step, also by virtue of new studies in the field of muon radiography, they have been equipped with disparate features. These are related to the ease of use in volcanic environments, to the improvements of the performances and to the background rejection capabilities of the detectors.

The detectors assembled up today come from the experience gained within existing experiments, while the Mu-Ray detector is the first detector designed and developed for the muon radiography. In the third chapter we will see how the Mu-Ray detector fulfill all the requirements of the muon radiography. The Mu-Ray detector have an active area of $1 \times 1 \text{ m}^2$ and 384 channels on 3 planes. The basic module has 32 scintillators which are read by silicon photomultipliers. The module is light ($\sim 25 \text{ Kg}$) and allows for the assembly of large area detectors. The detector is equipped with fast electronics to measure, with high resolution, the time of flight of the muon crossing the detector. Moreover, the detector has a sets of temperature and humidity sensors read by a local monitoring board. The detector has been provided with a water chiller for the thermal conditioning of the silicon photomultipliers. This is necessary to grant the silicon photomultiplies performance.

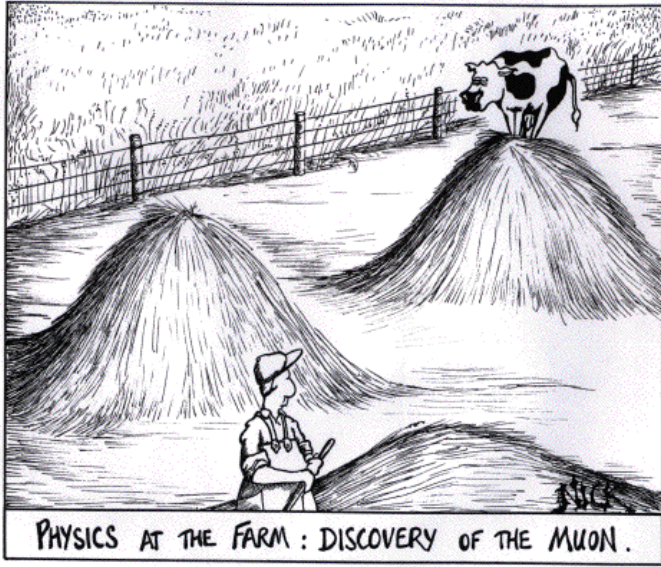
A raspberry Pi computer manage the data acquisition electronics and the slow control. It has been developed a software that implements an remote automatic system in order to make the detector autonomous by human intervention. This system, called MuBot, has allowed us to work uninterruptedly during the two measurement campaigns had at the Vesuvius and the Puy de Dôme in 2013.

In the forth, and last, chapter we will show the latest progresses, regarding the upgrade of the front-end electronics, the temperature control of the silicon photomultipliers and the improvement of the time of flight capabilities of the detector. These upgrades are not yet employed by the detector, we are currently working to implement them as soon as possible. We report about the temperature control system designed and prototyped to reduce drastically the high power consumption due to the employment of a water chiller to thermally control the silicon photomultipliers. We made a series of test to improve the design and to verify the performances of the Peltier cells working with passive cooling. We develop a system capable of good performances with 2 W per module of power consumption.

We report about the features and the characterization of the electronic. Together with the upgrade of the front-end electronics, we improve the time expansion circuit for the time of flight measurement. In the same time, we developed a time of flight model that has been verified using a suitable toy Monte Carlo. The latter simulate the response of the Mu-Ray detector when crossed by the bidirectional flux of muons. With our software tools and thanks to the proposed model, we were able to reconstruct muon tracks and discriminate between those coming from different direction. In this way we can remove those tracks coming from the albedo from our golden tracks sample, having in principle a rejection of the background never implemented on a detector for the muon radiography.

Part I

MUOGRAPHY: PHYSICS, PRINCIPLES AND DETECTORS



PHYSICS AT THE FARM : DISCOVERY OF THE MUON .

1

IMAGING WITH μ PARTICLES

Natural muons are generated from the so-called primary cosmic radiation. The primary cosmic rays are composed of stable charged particles and of nuclei with millions of years lifetime.

Once this radiation reaches the Earth atmosphere, it starts to interact with the atoms all along the stratosphere¹ and below, producing showers of new particles called secondary cosmic rays². At the sea level, the principal component of the secondary radiation is comprised of electrons, positrons, muons and protons.³

The decay of intermediate mesons π and K is such to generate high energy muons, which can reach 10^{21} eV. They are leptons, ~ 200 times heavier than the electrons, with a large energy spectrum and high penetrating power. The fraction of muons capable to pass through few thousands of meters of matter increases in the range of angles close to the horizon. In the figure 1.1 are shown the fluxes of vertical and quasi-horizontal muons; it shows an upper shift in energy of the flux spectrum at 90° in respect of the flux at 0° , in function of the muons momentum, hence of their energy. This means that the horizontal muon flux is more energetic than the vertical one, but the latter arrives with a greater average intensity with respect to the first.

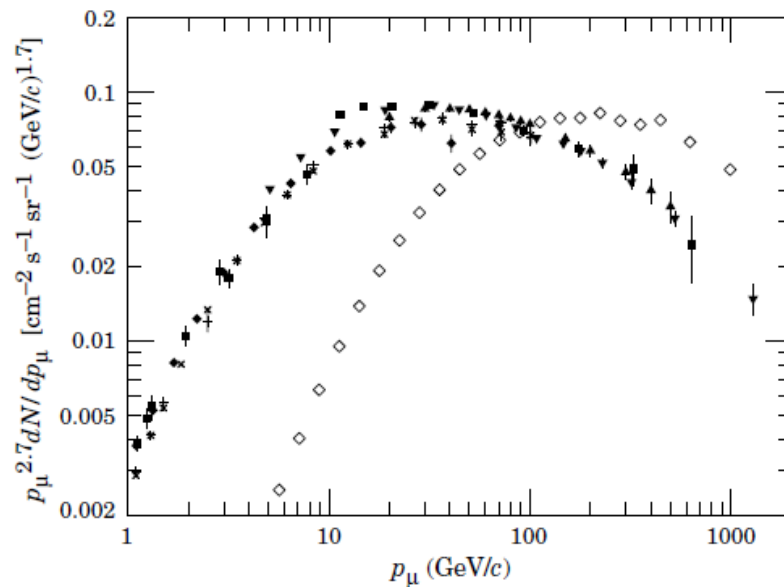


Figure 1.1: Energy Spectrum of Muons at 0° (black dots) and 90° (white dots). [PDG 2012]

- 1 The part of Earth's atmosphere that extends for 40 Km from 10 Km above sea level, is called stratosphere.
- 2 In general, secondary cosmic rays are generated by primary radiation during the interaction with interstellar gasses.
- 3 Protons and muons are respectively the most numerous particles in primary and secondary radiation.

The detection of muons at the Earth's surface is due to the time dilatation effect of the Theory of Relativity, because their mean lifetime in the muon's proper system of reference⁴ is $\tau = 2.2 \mu\text{s}$. Muons are mostly generated in the altitudes range between 26 Km and 15 Km and the mean energy of the muons at the sea level is 4 GeV, after they lost about 2 GeV reaching the ground. According to the Special Theory of Relativity, since the muon's mass at rest is $m_0 = 105.7 \text{ MeV}/c^2$, for a muon produced with energy $E = 6 \text{ GeV}$ one obtains

$$\gamma = \frac{E}{m_0 c^2} = \frac{6 \text{ GeV}}{105.7 \text{ MeV}} = 56.8 \quad t = \gamma \times \tau = 56.8 \times 2.2 \mu\text{s} = 125.0 \mu\text{s}$$

where γ is the relativistic term. By reverting the $\gamma(v)$ expression, we find the muon's speed to be $v = 0.9998c$ and so the resultant decay length is approximately 37.5 Km. This is reduced to 25 Km due to energy loss caused by the interaction with the atmosphere.

1.1 COSMIC RAYS

We make a distinction between two kind of cosmic rays: primary and secondary. To the first group belong stable charge particles originated by cosmic events, such as the Big Bang itself or, as it has been recently discovered, the Gamma Ray Bursts and other. This radiation is made of electrons, protons and Helium nuclei and it includes also other kind of nuclei such as those of Carbon, Oxygen and Iron. The presence of the Sun in Earth neighborhood leads us to consider to the anti-correlation between the flux of low energy primary rays and the sun's activities related to its magnetic field⁵.

When high energy primary cosmic rays interact with the upper Earth's atmosphere, they produce showers of secondary cosmic rays. As in the example in figure 1.2, a single incoming particle interacts with atoms in the atmosphere and, losing its energy or because it reached the end of its life, decays in products. A shower is originated from the decays of all incoming particles at a certain time and its composition depends upon the nature and the initial energy of each primary particle.

The flux Φ , in $\text{m}^{-2} \text{sr}^{-1} \text{s}^{-1}$, of the primary cosmic rays depends upon the energy E of the incoming particles, by means of the relation $\Phi = P_0 E^{-2.7}$ [Gaisser 1990]. The factor P_0 it is found to be approximately $1.8 \times 10^4 \text{ m}^{-2} \text{sr}^{-1} \text{s}^{-1} \text{GeV}^{2.7}$ for nucleons with energy in the range of few GeV up to hundreds of TeV [PDG 2012]. As shown in figure 1.3, the more the particles are slow, the more their flux is great. Typical rate of low energy particles is 1 particle per second in a surface of 1 cm^2 . On the other hand, high energy events are really rare and they can occur with a rate of 1 particle per Km^2 per year.

⁴ In the Special Theory of Relativity, with the proper time one refers to the lifetime measured in the frame of reference in which the muon is at rest.

⁵ Sunspots on the surface of the star and solar flares are phenomena regarding in different ways the magnetic behavior of the sun. These interfere with the magnetic field of Earth, giving rise the the so called solar modulation effect of cosmic rays. The modulation affects all cosmic rays with energy below 1 GeV and it is due to the compression that the solar wind exerts on the Earth's magnetosphere on the side exposed to the Sun. The reduction rate goes of incoming cosmic ray from 3% up to 20% depending on solar activity and it is know as the Forbush decrease [PDG 2012].

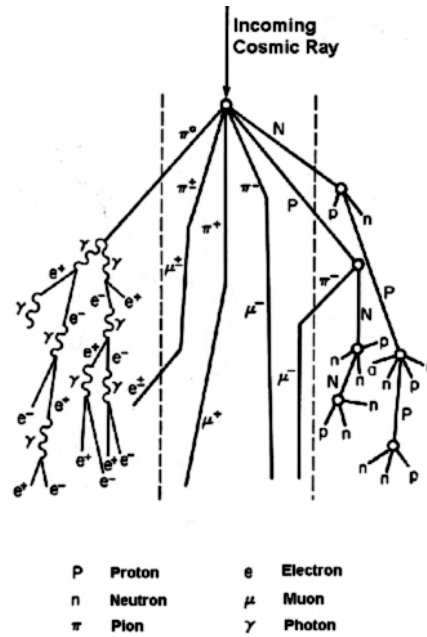
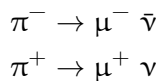


Figure 1.2: Example of a diagram of cosmic rays shower.

Starting from the primary radiation's components, hadronic processes generate pions (π) and kaons (K) which weakly decay giving rise to muons. The main reactions producing muons involve charged pions, through decays



with a $\sim 100\%$ branching ratio, where pion's mean lifetime is 26.03 ns. The other direct source of muons are charged kaons, which produce them in a similar way, with the branching ratio 63.5% (mean lifetime is 12.38 ns)⁶.

1.2 FLUX OF MUONS AT THE SEA LEVEL

While cosmic radiation has been studied since the early years of twelfth century, muons were discovered in 1937. Muons belong to the secondary cosmic rays and, at the sea level, they are the most abundant component of the charged cosmic radiation.

The number of cosmic particle that pass through unit area during unit time is by definition the flux of cosmic rays $\phi = \int_0^{2\pi} \int_0^{\pi/2} i(\theta, \varphi) \sin\theta \, d\theta \, d\varphi = \int i(\Omega) d\Omega$, where θ and φ are respectively the zenith and the azimuth angle and $i(\theta, \varphi)$ is the infinitesimal flux

⁶ A considerable flux of low energy muons comes from the reaction $K^\pm \rightarrow \pi^\pm \pi^0$ with branching ratio 21.3%, that produces μ^\pm through the decay of π^\pm

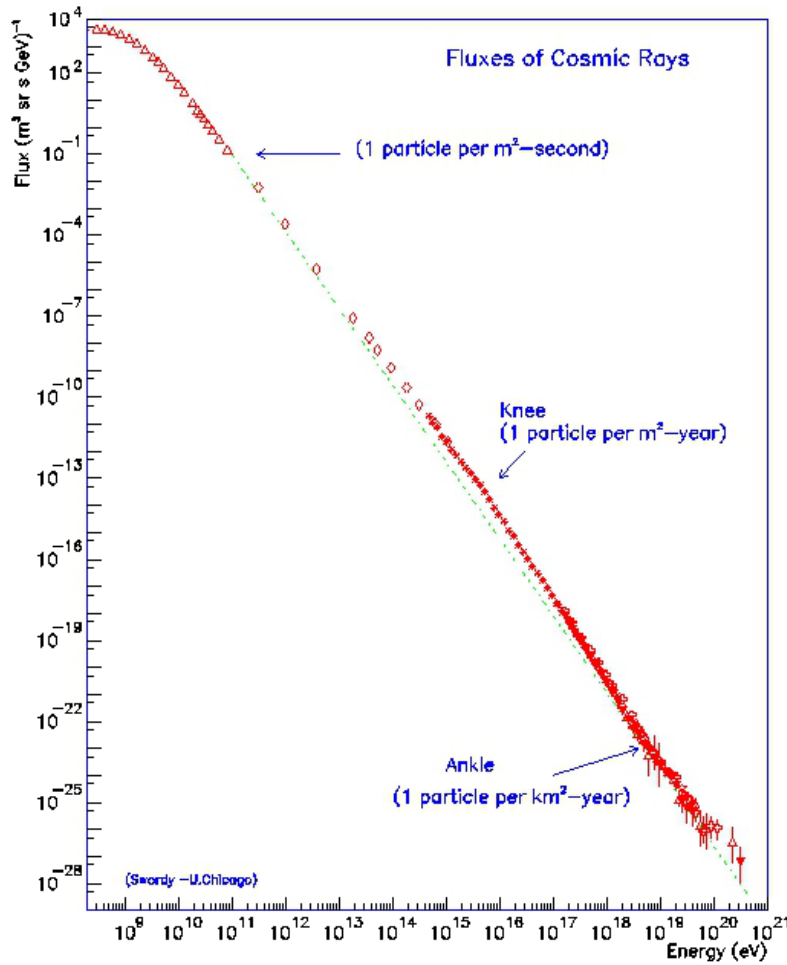


Figure 1.3: Cosmic rays flux as a function of energy. (Cronin, Gaisser, Swordy[©] [Cronin 1997])

per unit solid angle. The latter can be taken as a function of the thickness x passed by a cosmic ray at a given θ angle and, without loss of generality, we consider⁷

$$i_{\theta}(x) = i_{\perp} \left(\frac{x}{\cos\theta} \right) \quad (1.1)$$

where $i_{\perp} \left(\frac{x}{\cos\theta} \right)$ is the vertical flux function of the slant depth $\frac{x}{\cos\theta}$.

The formula 1.1 represents a good approximation of the flux for $\theta > 70^{\circ}$, while in the case of muons energy E_{μ} less than tens of GeV and for zenith angles smaller than 70° , experimental data [Grieder 2001] lead to consider

$$i_{\theta}(x) = i_{\perp} \cos^{\bar{n}}\theta \quad (1.2)$$

with $\bar{n} = 1.85$, being the mean value of n when we consider angles up to 70° and muons with energy greater than 1 GeV, which allows us to take $n = 2$ over a wide energy range.

⁷ We are assuming that secondary cosmic radiation is isotropic and, since they have been produced, the particles travel in straight line all along the atmosphere. Neglecting the dependence of the flux by the azimuth angle φ and being the attenuation of the flux an exponential function of the depth x in the atmosphere with mean attenuation length λ , one has $i(\theta, \varphi) = i_{\perp} e^{-x/(\lambda \cos\theta)}$. So, if the flux varies only in dependence of x , one considers the infinitesimal flux at depth x as the vertical flux in respect of the slant depth $x/\cos\theta$.

$i_{\perp} = i_{\theta=0}(0)$ is the vertical muons flux and at the sea level it is $\sim 70 \text{ m}^{-2} \text{ s}^{-1} \text{ sr}^{-1}$ [De Pascale 1993, Grieder 2001].

The differential flux per unit area and time is $d\varphi = P_{\mu} E^{-2.7} dE_{\mu} d\Omega$, where the factor P_{μ} takes into account the contribution of the particles π and K to the muons flux and it results

$$P_{\mu} \propto \left(1 + \frac{1.1 E_{\mu} \cos\theta}{\epsilon_{\pi}}\right)^{-1} + 0.054 \left(1 + \frac{1.1 E_{\mu} \cos\theta}{\epsilon_{K}}\right)^{-1} \quad (1.3)$$

where $\epsilon_{\pi} = 115 \text{ GeV}$ and $\epsilon_{K} = 850 \text{ GeV}$ are the critical energies⁸ of the two mesons and above these energies they decay before interact with the atmosphere. The same proportionality holds for muons arriving with $\theta > 70^{\circ}$, but, by meaning of figure 1.4, we have to consider

$$\cos\theta^* = \sqrt{1 - \frac{1 - \cos^2\theta}{(1+r)^2}} \quad (1.4)$$

which includes r as the dimensionless constant ratio between the muon's production altitude H ($\sim 30 \text{ Km}$) at zenith angles close to the horizon and the Earth radius R , both in the same unit [Lesparre 2012b]. Here θ and θ^* are such that $0 \leq \cos\theta \leq 1$ and $0.103 \leq \cos\theta^* \leq 1$ [Tang 2006].

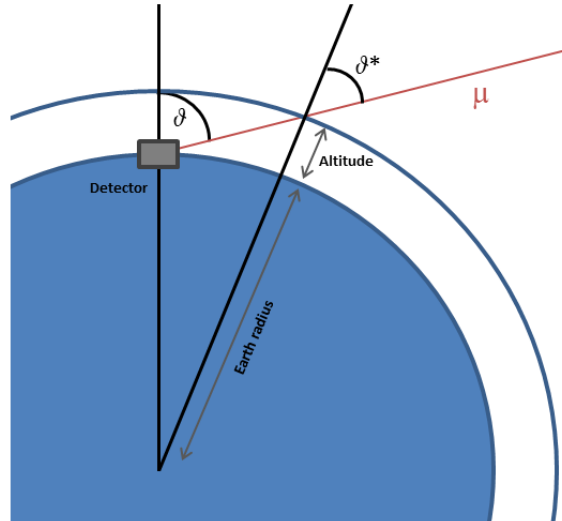


Figure 1.4: The angles θ and θ^* formed by an incoming muon, respectively, with the normal axis to the earth surface and with the normal axis to the top of the atmosphere.

1.3 ENERGY LOSS OF MUONS INTO THE MATTER

The energy loss of muons within the matter is often expressed in more general terms, in the form

$$-\frac{dE}{dx} = a(E) + b(E) E \quad (1.5)$$

⁸ "Critical energy" is variously defined as the energy at which the collision loss rate equals the bremsstrahlung rate. (source http://pdg.lbl.gov/2013/AtomicNuclearProperties/critical_energy.html)

where the parameters $a(E)$ and $b(E)$ take into account, respectively, ionization and radiative energy loss of the muon in function of the muons kinetic energy.

The main processes occurring in the passage of charged particles are inelastic collisions and elastic scattering. They determine energy losses and deflection from the original trajectory of the incident particles. We are not considering the phenomena of scattering, because we assume that the particles do not deviate significantly from their initial trajectory. However, the scattering deviates the muons less than 10 mrad along all the path they take.

Moreover, because of their small mass, electrons (e) and positrons (e^+) as well as having energy losses that depend on the interaction with the matter that they pass through, lose energy due to a predominant radiative effect called *bremstrahlung*⁹. This radiative energy loss (fig. 1.5), occurring for e and e^+ with energy above few tens of MeV, arises from the acceleration that they suffer from the electric field of the nuclei. Since the effect is inversely proportional to the square of the particle's mass and since muon's mass is 200 times the mass of the electron, a muon experiences a radiative energy loss 40000 times smaller than electron. So the loss of energy due to radiative effect in heavy charged particles is negligible in a wide energy range, up to 10^2 GeV.

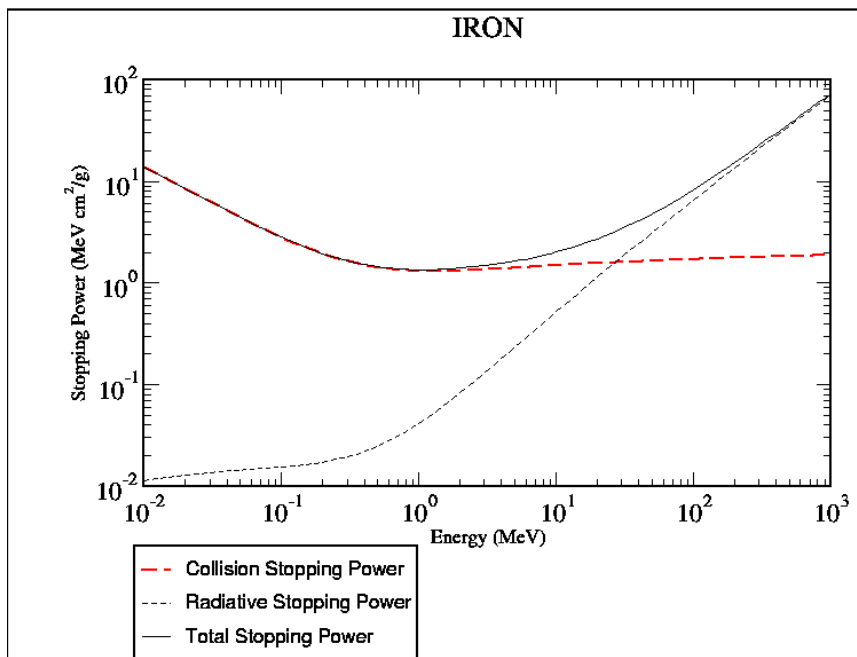


Figure 1.5: Stopping power vs kinetic energy diagram of e^\mp on Iron.
(Source <http://physics.nist.gov/PhysRefData/Star/Text/ESTAR.html>)

High energy heavy charged particles, like muons, do not suffer from the Coulomb scattering of the nucleus and penetrate atoms along their path up to few kilometers too. The passage of such particles into the matter produce the ionization of atoms resulting in the progressive energy loss of the passing particles. Those particles having energy loss

⁹ The *Bremstrahlung* is a Coulomb scattering process, that occurs in charged particle-nuclei interaction under the effect of the nucleus electric field. The moving particle experiences an acceleration that leads to the loss of part or all of its energy, by emission of electromagnetic radiation.

rates close to the minimum of the energy loss curve in figure 1.6 are called minimum ionizing particles (*mip*'s).

Consider a volume V , being A the area offered by a target to a radiative flux and δl its thickness, and the flux φ of particles per unit area and time. Then, the total number of particles scattered in all angles inside V is $N = \varphi A P_i(\delta l)$, where $P_i(\delta l)$ is the probability of interaction of the particles along δl . This probability depends upon the density ρ of the target's centers contained in V and the cross section σ , so $P_i(\delta l) = \rho \sigma \delta l$. Here, the cross section σ is commonly represented as a function of the energy E of the incoming particle and its value represent the probability whereby a certain process occurs.

But "what's the probability for a particle not to suffer an interaction in a distance x "? [Leo 1987] We easily find this probability to have the exponential form $e^{-x/\lambda}$, where the mean absorption length parameter $\lambda = (\rho \sigma)^{-1}$. The physical quantity corresponds to the mean path covered by the particle without having an interaction. In the case of muography, the length of the path of muons is a great multiple of the mean absorption length. The number of interactions of the muons with the matter is of order x/λ so is preferable to use the average energy loss per unit length. This physical quantity is called stopping power $-dE/dx$ and one of its expressions is commonly referred to the Bethe-Bloch Formula. In the center of the figure 1.6 is reported Bethe-Bloch diagram for muons on copper.

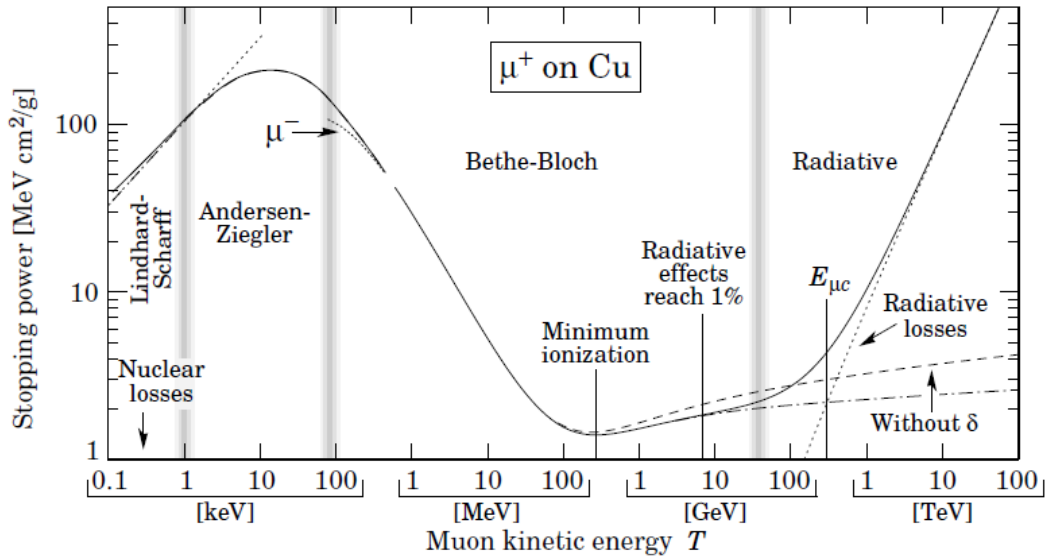


Figure 1.6: Stopping power vs kinetic energy diagram of muon on Cu. [Groom 2001]

Radiative processes occurs by meaning of *bremstrahlung*, $e^+ - e^-$ pair production and photonuclear interactions. A complete analysis concerning muon's radiative effects inside matter can be found in the work of Groom, Mohkov and Strikanov [Groom 2001]. The radiative energy loss contribution in the stopping power is no more negligible when energies are over 100 GeV. In this case a and b are approximately constant and the stopping power increases steeply, as it is shown on the right in figure 1.6. For muons with energy below 100 GeV, the contribution of $b(E)$ in equation (1.5) is negligible and $a(E)$ is constant at the first order [Hayakawa 1969]. So, the stopping power for muons with energy above some GeV is

$$-\frac{dE}{dx} \approx 2.1 \text{ MeVg}^{-1} \text{ cm}^2 \quad (1.6)$$

in dense materials, while it is less than $2 \text{ KeV g}^{-1} \text{ cm}^2$ in air. As stated at the beginning of the chapter, that explain 2 GeV of energy loss of the muon reaching the surface of the Earth.

1.4 MODELING THE MUONS FLUX

There are different models, both analytical and theoretical, to describe the muons energy spectra [Lesparre 2010]. The very basic theoretical one, which doesn't take into account the Earth's curvature and the attenuation of the muons flux along the atmosphere, is commonly attributed to Gaisser [Gaisser 1990, PDG 2012], and expressed in terms of the 1.3

$$\frac{dN}{dE_\mu d\Omega} \approx 0.14 \times 10^4 E_\mu^{-2.7} \left[\left(1 + \frac{1.1 E_\mu \cos\theta}{\epsilon_\pi}\right)^{-1} + 0.054 \left(1 + \frac{1.1 E_\mu \cos\theta}{\epsilon_\kappa}\right)^{-1} \right] \quad (1.7)$$

in units of flux, i.e. $\text{m}^{-2} \text{ s}^{-1} \text{ sr}^{-1}$. If one considers a vertical detector with 45° angular aperture, the probability distribution function (PDF) of the muons reaching the ground with energy in the range from 1 GeV to 10 TeV, in figure 1.7 is obtained by integration of the 1.7.

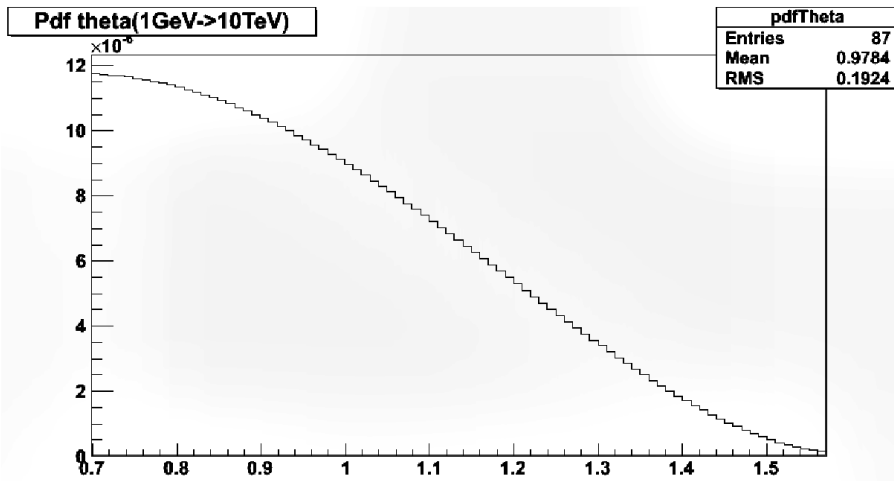


Figure 1.7: Probability Distribution Function of Muons at $45^\circ < \theta < 90^\circ$.

This represents a first approximation, that is somewhat valid for $\theta < 70^\circ$ and energy greater than $\frac{100}{\cos\theta}$ GeV. A more general formula can be derived from 1.7 and is given by

$$\frac{dN}{dE_\mu d\Omega} \approx 0.14 \times 10^4 E_\mu^\gamma \left[\left(1 + \frac{1.1 E_\mu^* \cos\theta}{\epsilon_\pi}\right)^{-1} + 0.054 \left(1 + \frac{1.1 E_\mu^* \cos\theta}{\epsilon_\kappa}\right)^{-1} + p \right] W(E, \theta^*) \quad (1.8)$$

that reduces to the original one for $W(E, \theta^*) = 1$, $\gamma = 2.7$ and $p = 0$. Here, these three factors are respectively the probability of muons to reach Earth's surface (survival rate of muons), the power index and the ratio of prompt muons to pions [Tang 2006]. Moreover, in the Gaisser model it is assumed $E_\mu^* = E_\mu$, where E_μ^* represents the initial energy of the muons and E_μ is their energy at the surface, once they have been revealed by a

detector after being passing through ordinary matter. This correction is important in the energy range above 10 GeV to take into account the energy loss due to the muons passage through the matter.

Thus, taking advantage of 1.2, with $n = 2$, and 1.4, when one considers at every θ angle the whole spectrum of muons, i.e. for energies $E_\mu > (100/\cos\theta^*)$ GeV and $E_\mu \leq (100/\cos\theta^*)$ GeV, it is required to choose the parametrization that fits at the best experimental data.

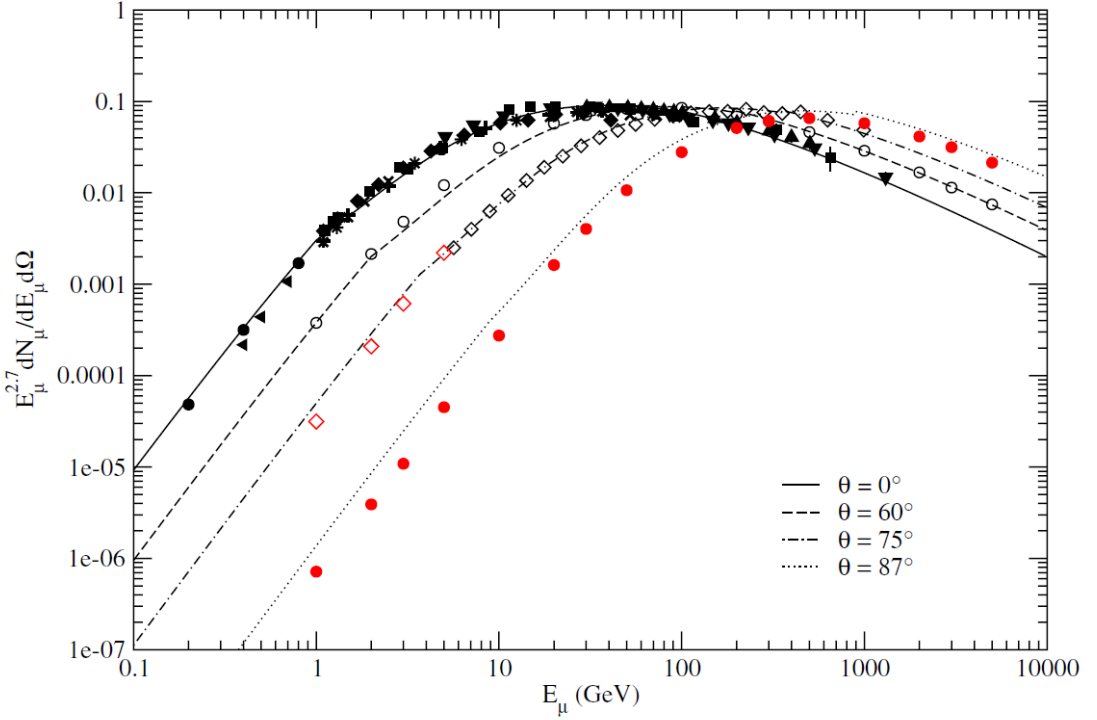


Figure 1.8: Modified Gaisser model fitting experimental data [Tang 2006].

In figure 1.8 it is shown the fit of data from different experiment, when we choose the Tang's corrections [Tang 2006] to the Gaisser model:

$$W(E, \theta^*) = 1.1 \left(\frac{90 \sqrt{\cos\theta + 0.001}}{1030} \right)^{\frac{4.5}{E_\mu \cos\theta^*}} \quad (1.9)$$

$$E_\mu^* = E_\mu + 2.06 \times 10^{-3} \left(\frac{950}{\cos\theta^*} - 90 \right)$$

$$p = 10^{-4}$$

in which we are neglecting the contribution of muons with energy below tens of GeV. Here, the additional factor appearing in the second equation must be linked to the 1.6, that is multiplied for the mean slant depth from the zenith angle θ^* ; this gives an estimate of the mean energy loss of muons along their paths. Recently, based on Kudryavtzev's work, it has been proposed [Lesparre 2010] to use the different parametrization

$$W(E, \theta^*) = \left(\frac{120 \cos\theta^*}{1030} \right)^{\frac{1.04}{E_\mu \cos\theta^*}} \quad (1.10)$$

$$E_{\mu}^* = E_{\mu} + 2.06 \times 10^{-3} \left(\frac{1030}{\cos\theta^*} - 120 \right)$$

$$\bar{E}_{\mu} = E_{\mu} + 1.03 \times 10^{-3} \left(\frac{1030}{\cos\theta^*} - 120 \right)$$

$$p = 10^{-4}.$$

Another model often used [Tanaka 2007, Lesparre 2010], and supported by Tanaka in his works, is based on the Matsuno model [Matsuno 1984]

$$\frac{dN}{dE_{\mu} d\Omega} \approx A (E_{\mu}^*)^{\gamma} \left[\frac{r_{\pi}^{\gamma-1} \epsilon_{\pi} \sec\theta}{E_{\mu}^* + \epsilon_{\pi} \sec\theta} + \left(\frac{K}{\pi} \right) b_r \frac{r_{\kappa}^{\gamma-1} \epsilon_{\kappa} \sec\theta}{E_{\mu}^* + \epsilon_{\kappa} \sec\theta} \right] W(E_{\mu}, \theta) \quad (1.11)$$

where $r_{\pi} = 0.78$ and $r_{\kappa} = 0.52$ are the fractions of energy transferred to the muon, respectively, in a pion decay or in a kaon one, $\frac{K}{\pi} = 0.36$ represents the ratio production rate of kaons to pions and $b_r = 0.635$ is the branching ratio of kaons. The muon's energy $E_{\mu}^* = E_{\mu} + \Delta E$, being ΔE the energy lost by the muon along its path. Moreover, the survival probability of muons to pass a length L is expressed as

$$W_{\mu}(E_{\mu}, \theta) = e^{-\frac{\sqrt{R^2 \cos^2\theta + 2 R H + H^2} - R \cos\theta}{6.2 E_{\mu}}}$$

A different choice of parameters can be done for this model too, although it should be noted that for *quasi-horizontal* flux the percentage variation among all models is of order $\pm 10\%$. In addition to these models, we could take into account the effect of altitude within 1000 m. It results [Hebbeker 2002] that the muons flux at h meters above the sea level is

$$\Phi(h) = e^{\frac{h}{4900 + 750 p_{\mu}}} \Phi$$

where p_{μ} is the momentum of the muon expressed in GeV/c and Φ is the flux of muons at the sea level described in terms of the corrected Gaisser's model. This further correction takes into account an increase in the flux of muons with energies up to ~ 100 GeV. As shown in figure 1.9, the increment in muons flux at higher altitudes is of some percent in respect of the flux at the sea level and it is more appreciable at energy below 100 GeV.

1.5 TECHNIQUE FOR MUON RADIOGRAPHY WITH COSMIC MUONS

The muon radiography (muography) is a technique based on the measure of the absorption of cosmic muons in the matter for direct imaging of large structures. In the case of geological structures, the muography is complementary to the traditional gravimetric, electrometric and seismological imaging methods. A muon detector¹⁰ placed on the slope of a volcano or, more in general, disposed opposite to an appropriate target, detects the muons, tracks their routes and counts them. This allows to calculate the average density along the paths taken by the muons.

¹⁰ We will use the next chapter to report about the state of art of the detectors for the muography. Here, the detector must be intended like a device composed of two planes, that are made of some material sensible to ionizing radiation and placed at a certain distance from one another. We use to call front plane the one who is in front of the target and back plane the other one.

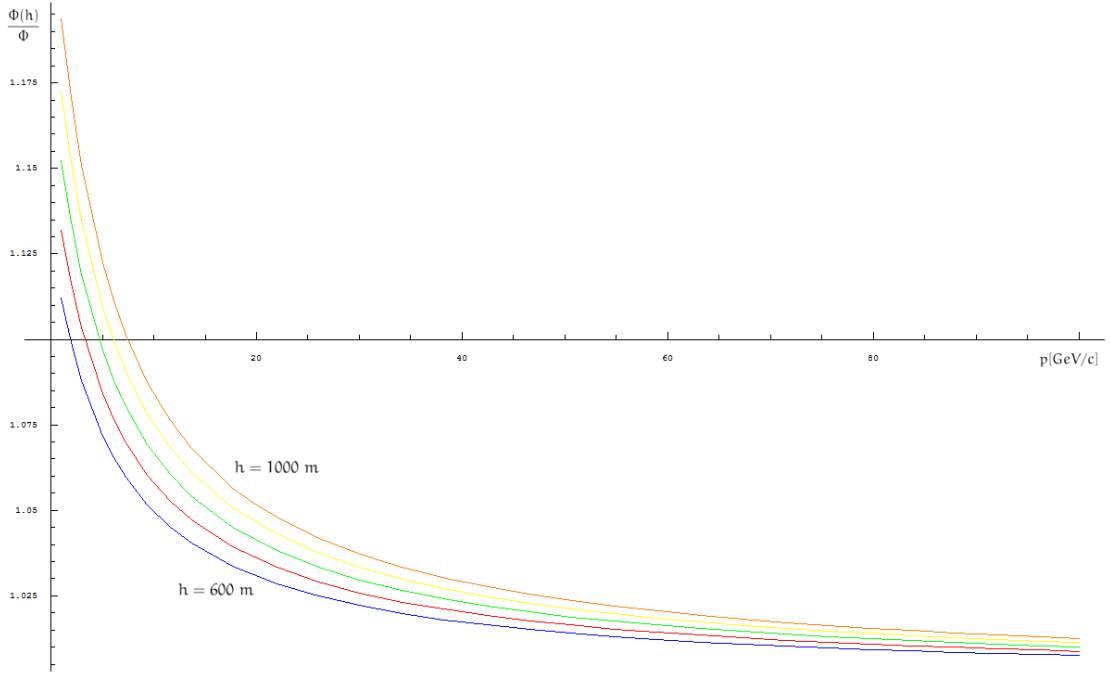


Figure 1.9: Trends of the ratio between the flux at different altitudes h and the flux at sea level as a function of the muons energy. The comparison of the curves gives the expected percentage change in the flux of muons at different altitudes.

Vertical detectors are required in muography because one needs to use the quasi-horizontal muons flux, which is characterized by being highly energetic. Muons having energy above 100 GeV have stopping power $\sim 2.5 \text{ MeV g}^{-1} \text{ cm}^2$ [Tanaka 2013].

As well as the known technique of radiography, based on X-rays, is used to have a direct image of the interior of a small body, the radiography with muons is, in principle, useful when the transverse length of the target is few kilometers thick. But, differently from X radiography, the source of the radiation is not tunable; to improve the signal-to-noise ratio, muography requires large instrumentation, long data tacking time and high background rejection capability. As an example, the rate of mouns in a vertical tracker, with 1 m^2 area, is about 4 Hz/m^2 . The rate decreases, when we want count the muons survived to the passage through a target.

Under ideal conditions, the transmittance in function of the zenith and azimuth angles, can be defined as

$$T(\theta, \varphi) = \frac{N(\theta, \varphi)}{N_{\text{exp}}(\theta, \varphi)} \quad (1.12)$$

that is the fraction between the number $N(\theta, \varphi)$ of muons that pass through the target and the number $N_{\text{exp}}(\theta, \varphi)$ of expected ones without the target. The expected number of muons can be evaluated with Monte Carlo software or with a data acquisition, pointing to the *free sky*. The latter measure has the advantage to include the detector efficiencies and geometrical factor, while in a Monte Carlo simulation must be a priori well known. The measure of the transmittance with the *free sky* measurement involves two different

measures, in different time, so that the detector looks to the target and then, after it has been turn of an angle φ_0 , to the *free sky*. The equation 1.12 becomes

$$T(\theta, \varphi) = \frac{t_{fs}}{t} \frac{N(\theta, \varphi)}{N(\theta, \varphi + \varphi_0)} \quad (1.13)$$

in which

- t_{fs} : time taken to perform the *free sky* data taking
- t : time taken to perform the data taking
- $N(\theta, \varphi)$: number of detected muons passed through the target
- $N(\theta, \varphi + \varphi_0)$: number of muons counted during the *free sky* run

where the ratio $\frac{t}{t_{fs}} = 1$ taken equal 1, if it normalizes the flux of the *free sky* to the time t .

Another method is often used to measure the *free sky* flux, when the back of the detector is free from objects and the forward and backward acceptances, ϵ_{fw} and ϵ_{bw} respectively, are known. It consists in the measure of the flow of particles crossing the detector from the back, while the front heads off the flux coming from the target (fig. 1.10). In this case, the form of the transmittance is

$$T = \frac{\epsilon_{fw}}{\epsilon_{bw}} \frac{N(\theta, \varphi)}{N(-\theta, \varphi)}. \quad (1.14)$$

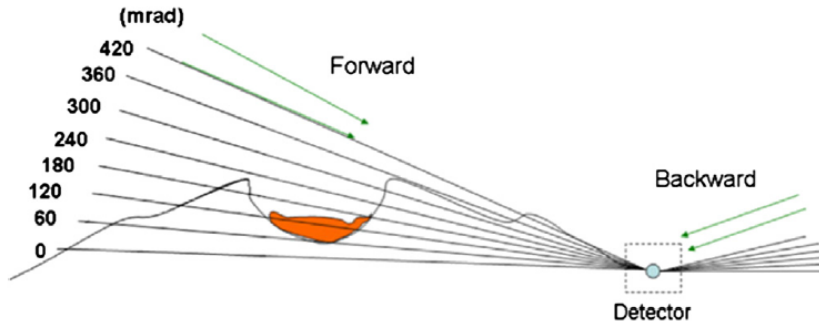


Figure 1.10: Schematic measurement of the *free sky* flux by means of the backward flux. [Tanaka 2007]

where $N(-\theta, \varphi)$ is the number of muons which come from the back.

Once the transmission map of the target has been reconstructed, we can obtain the expected depth in kilometers water equivalent (Kmwe) penetrated by muons at different zenith angles. This is useful because water constitutes an homogeneous medium, with unit density ρ_w by default, and the depth measured using water can be easily compared to inhomogeneous material [Hayakawa 1969]. Muons with energy of order 100 GeV can penetrate into matter less than 1 Kmwe, while more energetic muons can pass few Kmwe [Tanaka 2007].

The expected depth in Kmwe could be evaluated, for example, with a simulation in GEANT4 []. In this case, the expected transmission, as a function of the different path length at different zenith angles, is evaluated as the ratio of the number of the survived

muons to the number of injected ones. The energy spectrum at different θ of the injected flux is the equation 1.11 and the curves, parametrized by the zenith angle, in 1.11 are plotted counting the number of survived muons at each path length¹¹ passed in a given volume of material of known density. If we assume the density of the water $\rho_m = 1$, the real path length is equal to the depth in kilometers water equivalent (Kmwe) penetrated by muons.

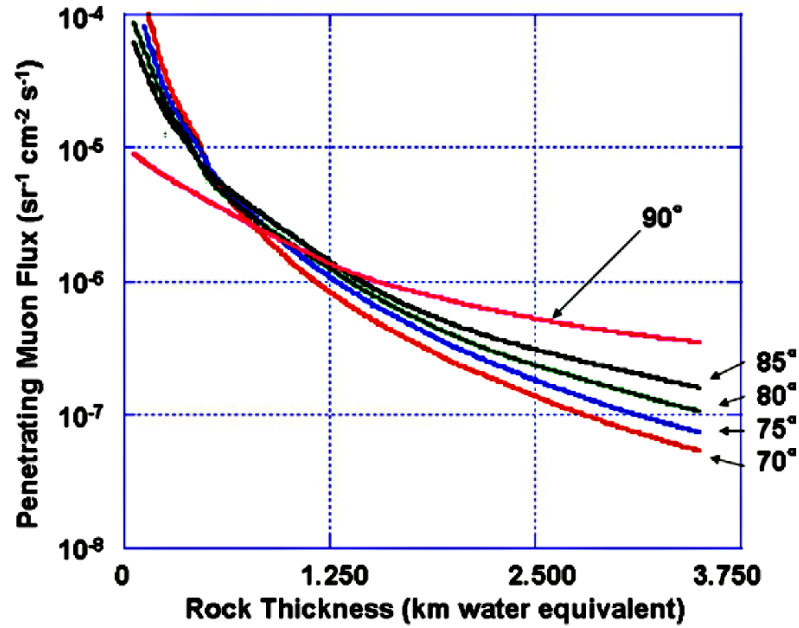


Figure 1.11: Integrated flux of cosmic-ray muons at various zenith angles penetrating through a given thickness of rock with a density of 2.5 g/cm^3 . [Tanaka 2007]

Once all values of the transmittance at every angle have been measured, inverting these curves, one obtains the related map of path length $x_\theta = \Lambda_\theta$. Since $x_\theta = L_\theta \rho$ and being L_θ the thickness of matter, of unknown density ρ , traversed by the muon at angle θ , we have

$$\rho = \frac{\Lambda_\theta}{L_\theta} \quad (1.15)$$

where, in the case we are dealing with a large target like a volcano, L_θ is commonly measured with the aid a digital elevation model (DEM).

¹¹ The path length represents the total amount of a material, with mean density ρ_m , passed by cosmic rays.

2

THE STATE OF ART OF DETECTORS FOR THE MUOGRAPHY

It was 1995 when the first modern application of the muon radiography was tested by Nagamine and its team at the Mt. Tsukuba in Japan [Nagamine 1995]. Since the beginning of the new millennium, many trials have been conducted around the world by team of researchers from Japan, Europe and North America. Within the muon radiography applications are included the radiography of large object such as volcanoes and geological structures, for extraterrestrial uses too [Kedar 2013], underground inspection for mining [Malmqvist 1979] and archaeological purposes [Alvarez 1970], estimation of nuclear waste in silos¹ [Mahon 2013], scanning of cargo for nuclear contraband [Morris 2012] and very recently scanning of the Fukushima Daiichi nuclear power station² [Perry 2013].

We will deal exclusively with muon radiography for volcanic purposes, in which are actually employed Japanese researchers groups headed to Tanaka, DIAPHANE [Gibert 2010; Lesparre 2012c; Marteau 2012] and TOMUVOL [Portal 2012; Carloganu 2013] groups from France, Mu-Ray [Beauducel 2010; Ambrosi 2011] experiment from Italy and other international collaborations. The common scope to all these projects is to improve the methods of analysis and to make the first tomography of a large geological structure, matching the direct image provided by muon radiography with the indirect ones obtained with classical methods and widely used by geophysicists, such as seismic, gravimetric and electromagnetic. On the contrary, as regards the detectors with which it performs radiography, all projects use different technological approaches. This is mostly due to the experimental background of researchers, since they were or are actually involved in other experiment, from whom they have inherited the main technologies.

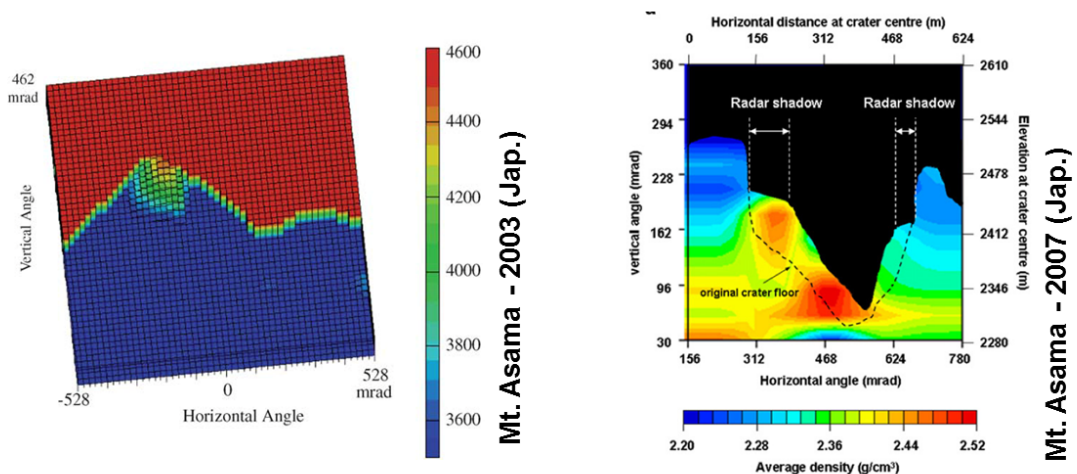


Figure 2.1: Muography obtained at Mt. Asama with electronic detector in 2003 [Tanaka 2003] and with emulsion in 2007 [Tanaka 2007b].

¹ <http://indico.cern.ch/event/186337/material/slides/o?contribId=257&sessionId=11>

² <http://permalink.lanl.gov/object/tr?what=info:lanl-repo/lareport/LA-UR-12-20494>

Since year 2000 Japanese reserachers have tested the methodology of muon radiography in different sites and with different detectors. At the Mt. Asama they used both electronic detector (2003) and nuclear emulsion (2007). As in figure 2.1, the comparison between images shows an impressive resolution in the case of emulsions, but the data reconstruction of an emulsions based detector is very hard and can not furnish real-time information. Because of the low statistic and long data taking, the fast reliability of the data and data quality checks are very important for this kind of experiment. This has prompted researchers to develop electronic detector that would improve the resolution of the image obtained at Mt. Asama by Tanaka in 2003.

DIAPHANE'S ELECTRONIC DETECTOR AT LA SOUFRIÈRE DE GUADELOUPE

During year 2012, DIAPHANE group published, in figure 2.2, the first high resolution image of the average density of a volcano, La Soufrière de Guadeloupe, obtained with an electronic detector [Lesparre 2012c]. The work is very detailed and elaborated density data have been compared with geology, electrical resistivity and gravity data finding an accordance between methods that should encourage further improvements of the techniques and apparatuses for the muon radiography.

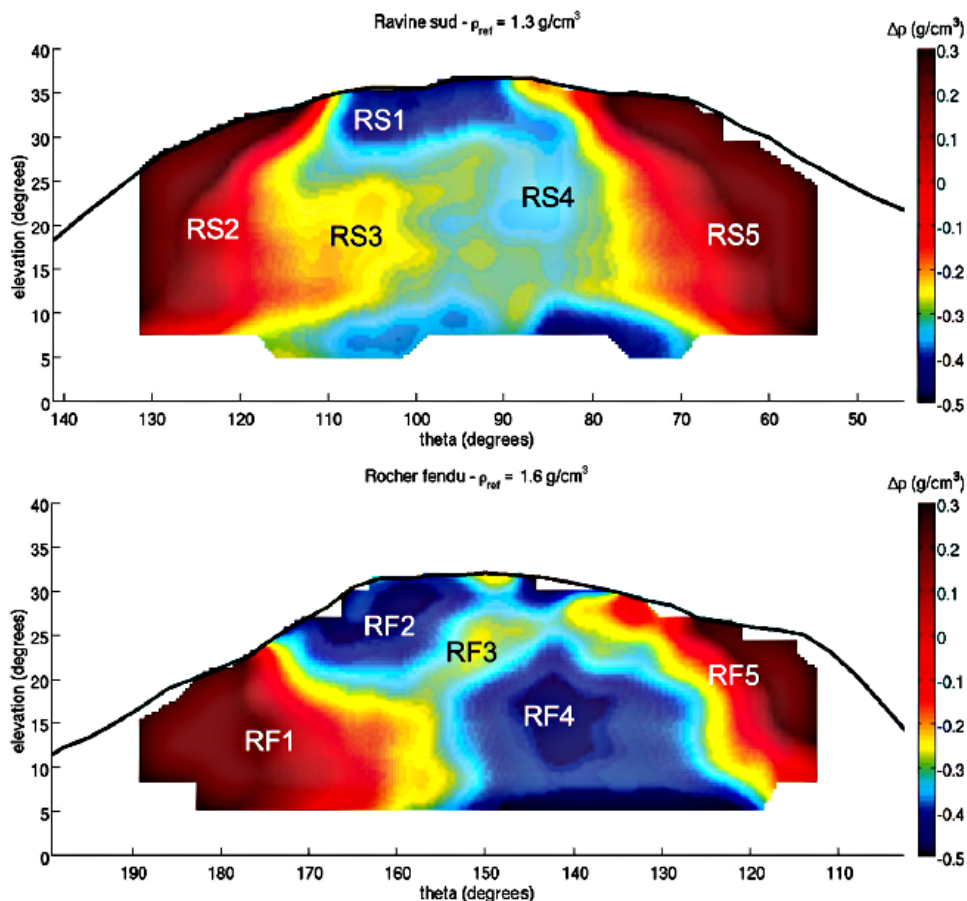


Figure 2.2: La Soufrière de Guadeloupe radiography with electronic detector in two different sites (RS: Ravine Sud, RF: Roche Fendue) [Lesparre 2012c].

The DIAPHANE researchers worked for several months, including about 6 months of data taking, to altitudes of 1163 m at the Ravine Sud site and 1268 m at the Roche

Fendue, respectively located on the south and the eastern side of the lava dome. They moved ~ 800 Kg of instrumentation, using an helicopter to bring equipments on site. The instrumentation included solar panels and accumulators for power supplying functions. Prolonged cloudy periods have caused power failures, where the equipments had 40 W of power consumption and panels experienced power peaks of ~ 700 W. The detector has been equipped with remotely controllable relays to turn on and off the devices and it presented various sensors for the monitoring of environmental and working conditions.

2.1 REQUIREMENTS OF A DETECTOR FOR THE MUON RADIOGRAPHY

Experiments usually run inside laboratories, where it is simple to control environmental conditions and to have electrical power. Moreover the handling of the detectors often happen with the aid of mechanical tools capable to lift heavy loads, the global performances are continuously monitored and broken parts are suddenly substituted. Work in a volcanic area is different from working indoors. The effect of altitude affects the performance of the operators and also weather conditions can hinder the handling of apparatuses. The excessive heat and cold conditions, rain, snow and sometimes hurricanes are quite common in a volcanic area. Therefore, a detector for the muon radiography must be light and easy to transport, rugged and, at occurrence, rainproof.

In order to fulfill all these requirements, the modularity of a muon detector for the radiography of volcanoes is strictly required. It allows for easy transport and handling on site, moreover it represents the best solution for assembly large area detectors. The need to create large area detector is imposed by the low rate of muons in the region of horizontal flow when this appears to be decreased by the presence of the volcano. Since the statistics of the muons gathering is strongly enhanced by a greater collection of events, experimentalists have the possibility to prolong the time of acquisition or to increase the area available to the flow of muons. These are related through the expression, used in 1.12- 1.14,

$$N = \varphi t \epsilon_{fw} \quad (2.1)$$

that gives the number on detected muons as the product of the flux φ passing through the volcano, the time t taken to perform the data taking and the acceptance and efficiency factor of the detector ϵ_{fw} .

Another request, really implicit, is the detector capability to track muons trajectories. Acting as an hodoscope, the detector must be able to record a three-dimensional events using a suitable coordinate system (fig. 2.3 a). The angular resolution is linked to that feature because it determines the ability of the detector to distinguish two different tracks hitting the detector at different angles. But for the muography of volcanoes, instead of an high angular resolution, we will request a good angular resolution. Since, it has been evaluated [Antonioli 1997; Tanaka 2008] that muons passing ~ 3 Kmwe with sufficient energy will be scattered, many times along their path by meaning of multiple scattering, of ~ 10 mrad, a detector must have an angular resolution greater than this value.

2.2 BACKGROUND'S REJECTION AS A FURTHER REQUIREMENT

Working outdoor, every detector experiences a background noise that may be due to accidental coincidences, arising from electromagnetic cascades generated near the detector, or to low energy muons (< 1 GeV) that penetrate the detector from the direction of the target, or e^- and e^+ crossing the detector from every direction. This background blurs the flux of muons and in principle it could affect the measurement irreversibly. A first arrangement, that consists in increasing the spatial segmentation, allows for best background rejection for that kind of noise coming from multiple hitting due to cascades that generate inside the geometrical acceptance of the detector.

Dealing with uncorrelated noise, for example, caused by charged particles that do not pass through the detector, but that affect just a part of it in coincidence of other hits, the accidental coincidences for a two planes detector happens with a rate $A = 2 N_{fw} N_{bw} \tau$ [Eckart 1938] or $A = 4 N_{fw} N_{bw} \tau$ as it is used by Lesparre *et al.* [2012a]. Here N_{fw} and N_{bw} are respectively the rate of hits of the forward and backward planes and τ is the time resolution of the detector trigger. As results from the latter relation, the factor that affects the background rejection is the time resolution. Lower values of τ correspond to a smaller rates of accidental coincidences. For example, Lesparre *et al.* [2012a] estimated a rate of ~ 10 fake tracks per day, where $\tau = 10$ ns. In the case of TOMUVOL detector, $\tau = 250$ ns implies $A \approx 250 \text{ day}^{-1}$.

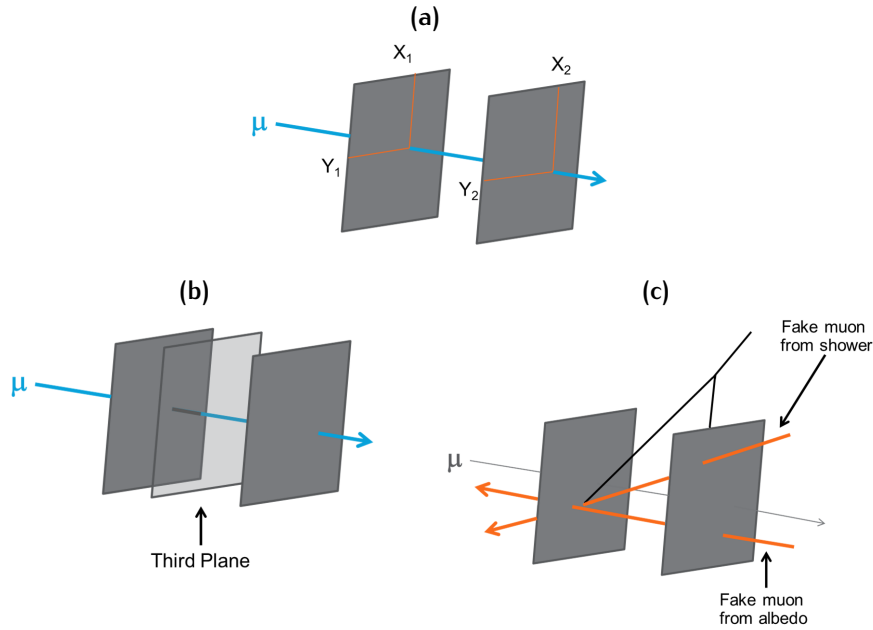


Figure 2.3: Tracking capability and background rejection of a muon detector.

Since this kind of coincidences is mainly due to charged particles hitting just one plane of the detector in coincidence to another hit, another contribution to reject this part of the background is the employment of a third plane (fig. 2.3 b). This arrangement drastically reduce the rate of accidental coincidences of a factor $4 N_{bw} \tau$, if it is evaluated with

the formula $A = 16 N_{fw} N_{md} N_{bw} \tau^2$ [Lesparre 2012a] and in general introduce the constraint that traces align on three points, one for each plane. Despite this, following another argument [Eckart 1938], three planes coincidences are such that, to the number A of accidental coincidences discussed above, one should include also additive factors relative to the recording of an accidental hit combined with a causal coincidence that occurred between the other planes. In our case we can consider only causal coincidences that have developed between neighboring planes and the number of fake tracks is given by the formula $A = 4 N_c N \tau + 3 N^3 \tau^2$, where we assumed on average $N_{fw} = N_{md} = N_{bw} = N$ and N_c represents the number of causalities occurring on average between the forward-middle and backward-middle planes. In those cases in which the contribution of N_c is not negligible and perhaps of the same order of N , the first term may dominates because of the presence of τ at the first power and, in this case, no real background rejection will be available for this kind of noise using this method.

Another source of background comes from electrons, and positrons, having enough energy to be detected. This kind of noise can be easily removed using iron shielding. The presence of a screen stops the low energy component in function of its thickness. The most part of experiments adopted iron shielding, and in for DIAPHANE a 24 mm iron screen to stop charged particles with energy smaller than ~ 100 MeV [Lesparre 2012]. The shielding is also useful to stop the soft component, energy below ~ 65 MeV, of the muon flux.

Finally, the measure of the muon's time of flight has been recently taken into account to reject fake tracks mimicking muons coming from the target. These tracks are muons scattered in the surrounding ground and deflected from their original trajectory, that cross the detector from the back plane to the front one at an angle that makes them look as good tracks (fig. 2.3 c). Different methods have been developed based on time recording technology, depending on availability, employed by various detectors. The detectors that want to implement the time of flight of the muon must also have a high time resolution lower than 1 ns [Ambrosino 2014].

2.3 DETECTORS IN MUOGRAPHY

During years, the modern detectors for muon radiography have been improved and equipped with better technologies to match as possible all these requirements. Since 2000, scientist have used the extensive experience accumulated by high energy Physics in the development and implementation of the detectors. All detectors described below are a specific application of detectors already used in other fields of the Physics.

2.3.1 Japanese Detectors

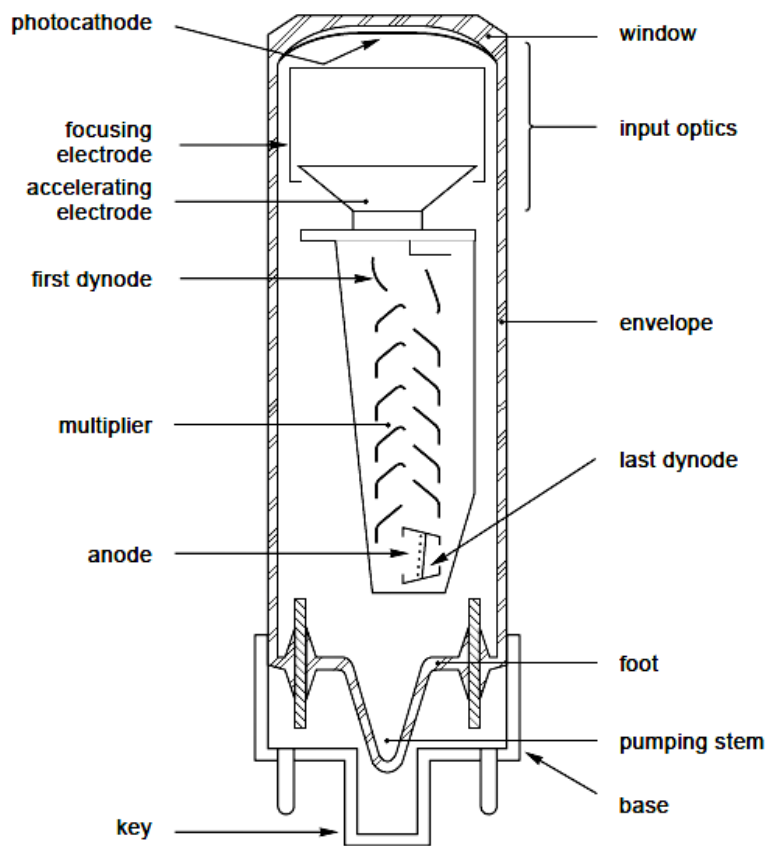
During their campaign, Japanese researchers has employed different detectors, using both electronics and emulsions detectors. The main technologies used for electronic detector are the plastic scintillators and photomultiplier tubes.

PLASTIC SCINTILLATORS COUPLED TO PHOTOMULTIPLIER TUBES

The *plastic scintillators* are object able to detect the passage of ionizing radiation. Once a charged particle penetrates the scintillator, it gives away part of its energy to some of the

fluorescent molecules of organic scintillator dissolved in the solid plastic [Leo 1987]. This absorbed energy is rapidly re-emitted as a flash of light, containing a certain amount of photons, by the excited molecules and the amount of light released is in good approximation linear in respect of the energy deposited by the particles passing through the scintillator. Their response is very fast and decay time is of few ns. This is really important in terms of the resolving time of the detector. Photons thus produced travels the scintillator, that is transparent to the electromagnetic radiation, and the read out of the scintillator is done with a photomultiplier.

The *Photomultiplier tubes* (PMT) are photo sensors sensitive to the single photon (fig. 2.4). Their principles of the detection is the external photoelectric effect. When one or more photon hits the photocathode, made of photoemissive semiconductor material, they generate, with a certain probability, photoelectrons. These are accelerated under the effect of an high electric field and focused on the first dynode. The photoelectrons interact with the dynode producing several new electrons which are accelerated, under the effect of a constant electric field, towards the next dinode. A certain number of dynodes are disposed inside the PMT in such a way to multiply and collect the the most part of electrons produced. The avalanche process goes on until a great number of electrons, of order $10^6 \div 10^7$, flow to the anode, where this current is read. PMT are, in good approximation, linear devices in respect of the number of the hitting photon and works with a power law in respect of the voltage applied as shown in figure 2.5.



MRB100

Figure 2.4: Schematic of a photomultiplier tube [Flyckt 2002].

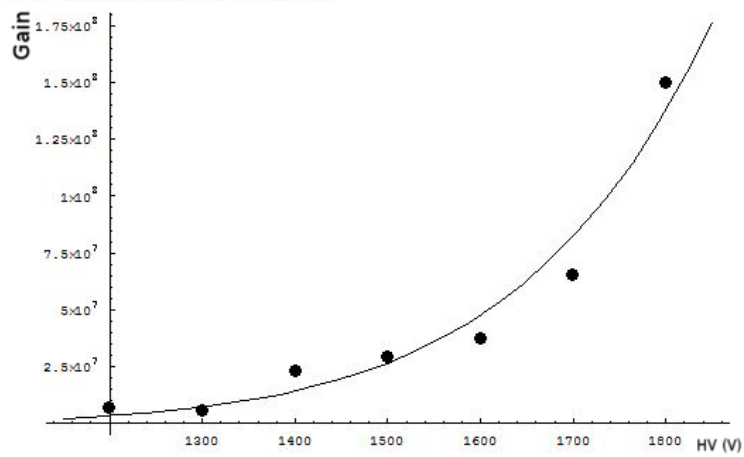
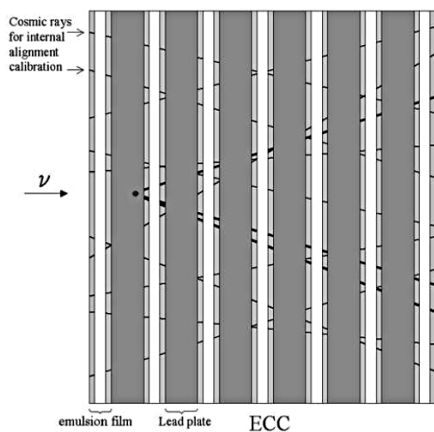


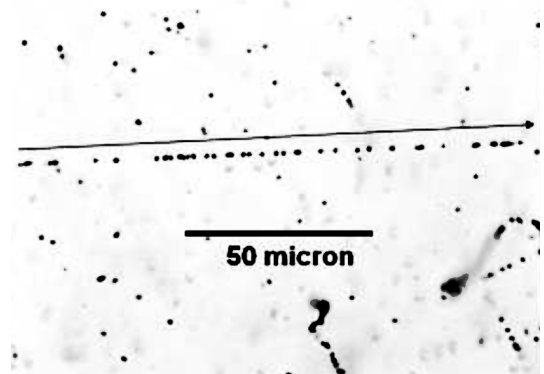
Figure 2.5: Experimental measurement of the gain of a repaired Hamamatsu PMT. The fitting curve has equation $g(v) = 7 \times 10^{-22} v^9$.

NUCLEAR EMULSIONS

The *nuclear emulsions* are radiation detector working in the same way of a photographic film. The passage of a particle is recorded, depending on the incoming direction, as a spot or a line and data are acquired using a microscope (fig. 2.6 b). The emulsion has tens of μm thickness and variable area, for example the OPERA brick has $10.2 \times 12.5 \text{ cm}^2$ area of and is composed by two 44 μm sensitive layer of emulsions separated by a 205 μm plastic base [Di Fernando 2008]. Particles ionize molecules along their paths leaving a black track made of Silver grains. Bricks are separated to each other by 10 mm thickness of iron or lead and they are arranged in a matrix composed by several layers of emulsion (fig. 2.6 a).



(a) Section of a matrix of emulsion bricks showing example tracks [Di Fernando 2008].



(b) Analysis of tracks in OPERA experiment. It also shows a charged particle passed along the film [Fukuda 2009].

Figure 2.6

Emulsions have the higher spatial resolution ($0.3 \mu\text{m}$) actually possible to a particle detector, but data reconstruction is very hard and the background radiation is always recorded in open sky conditions. To avoid data contamination from this kind of noise,

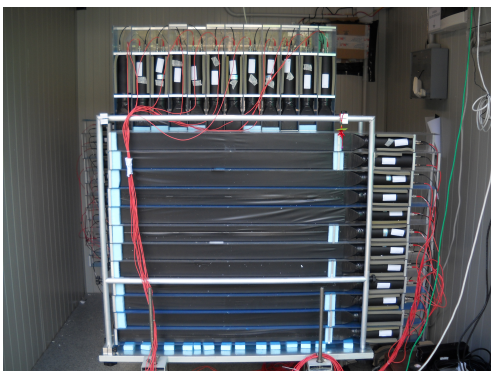
scientists use to assemble and disassemble the matrix of bricks out of acquisition time, so that the recorded tracks are uncorrelated and can be treated as background. A stock of emulsion can be used for a limited period, since the recorded tracks vanish in time depending on environmental condition and quality of the films. Bricks can be reused after they have been refreshed in deep underground laboratories [Fukuda 2009].

2.3.1.1 PAC System at Mt. Asama.

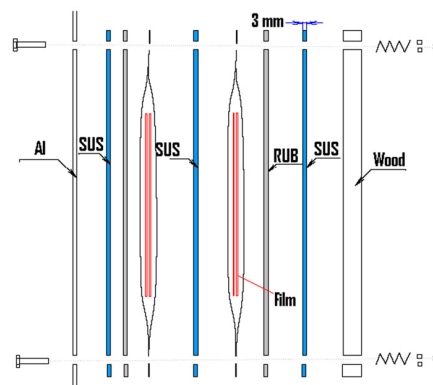
During 2001 Japanese researchers used a couple of detector system to look at the Mt. Asama. Each detection system consisted in a two-station muon detector and each station consisted in two planes scintillators, one for the x coordinate and the other for the y coordinate. Since the basic unit of the detector is a rectangular box including a scintillator coupled to a PMT, it represents the first easy to assemble detector for muon radiography purposes and its name, portable assembly-type cosmic-ray muon imager (PAC), arose on this feature. All scintillators had sizes $100\text{ cm} \times 10\text{ cm} \times 3\text{ cm}$ ($l \times w \times t$) and all planes were composed by 10 Scintillators. The read out of the scintillators were done using PMTs. It result that the segmentation was $10 \times 10\text{ cm}^2$ large. Total detector area was $2 \times 1\text{ m}^2$ and each station was 1.5 m away from each other, the achieved angular resolution was 66 mrad. At a distance of 3 Km from the volcano, the spatial resolution was $200 \times 200\text{ m}^2$. Moreover, to limit the soft component of cosmic rays, two 5 cm iron shields were inserted between stations. The passage of a muon is recognized by the coincidence of four PMT signals, one per plane, in a 100 ns time window.

2.3.1.2 Emulsion Chamber Detector at Mt. Asama and Mt. Usu.

In the second (2006) campaign at Mt. Asama, Japanese researchers used nuclear emulsions assembled in a folded chamber of active area of $40 \times 100\text{ cm}^2$. Two sets of emulsion bricks was arranged in two matrix divided by 3 mm of iron. Two other iron shields were placed to close the uncovered sides of the matrix. A similar detector, 6000 cm^2 active area, was used in 2006 at Mt. Usu. The third campaign took 6 months, while the previous lasted for a couple of months. In both campaigns, the distance from the lava dome of volcano was $\sim 500\text{ m}$.



(a) Japanese PAC detection system during *free sky* acquisition at Mt. Vesuvius in the month of March, 2011.



(b) Schematic of an emulsion chamber used to radiograph the Mt. Asama [Tanaka 2007a].

Figure 2.7

2.3.2 DIAPHANE: RaCoon and MusTang telescopes

During 2010, DIAPHANE group conducted two campaigns, one on the Etna (Sicily, Italy) and the other one at La Soufrière de Guadeloupe (Guadeloupe, France). However they used the same kind of detector in both sites, the MusTang detector, used in Guadeloupe, and the RaCoon, used in Sicily, differs for some features and RaCoon looks like a basic version of MusTang.

Both detectors have planes of plastic scintillator, where each plane is formed by 16×16 scintillators, 16 per view. The scintillator bars are MINERvA type with co-extruded hole, in which it is cemented a wavelength shifting (WLS) optical fiber. Each bar is 80 cm long and has a rectangular section of $5 \times 1 \text{ cm}^2$. Planes have 0.64 m^2 and are arranged at 115 cm distance front to back. The RaCoon detector worked in this original form during the campaign on the Etna. Mustang, started with three planes and a 2.4 cm thick iron shield. The readout of the fibers has been done with a 64 channels multi-anode PMT, having 24 mA of maximum power consumption. Clear optical fibers were adopted to link the WLS output to the photosensors.

The electronics and the acquisition system were developed in part individually and in part inherited from the experiment OPERA. One of the main features is a clock distribution system that synchronize all nodes of the system. It allows for 10 ns of resolving time and after a series of correction due to the delayed propagation of the signals, it assigns a precise time stamp to all recorded events. The analysis of the records lets determine whether the event belongs to a track or not. In principle, this system allows for the measure of time of flight of the muon. Another features are the presence of a self assembled mini-PC, in order to have a good stability during the data taking and to ensure low consumption, and the use of solar panels. Moreover, the detector is equipped with several temperature and humidity sensors read by an off-the-shelf data logger. As regards the mechanical structure, the detector has the possibility to be tilted. This quality allows detect a smaller amount of background, in particular the one coming from backward [Tanaka 2007b].



(a) RaCoon detector at Etna (Ita.) during the month of June, 2012.



(b) MusTang detector at La Soufrière de Guadeloupe (Fr.) during the month of July, 2012.

Figure 2.8

2.3.3 TOMUVOL Muon Tracker

The TOMUVOL Project is a collaboration between the Laboratoire de Physique Corpusculaire (LPC), the Laboratoire Magmas et Volcans (LMV), the Observatoire de Physique du Globe de Clermont-Ferrand (OPGC), the Institut de Physique Nucléaire de Lyne (IPNL) and the Ecole Supérieure des Géomètres et Topographes (ESGT), with head quarter in Clermont-Ferrand (France). They developed a muon detector with glass resistive plate chambers (GRPCs), based on the experience of the CALICE calorimeter. In 2011 they conducted a measurement campaign at Puy de Dôme, from the point of view of Grotte Taillerie with a prototype detector of $\sim 1/6 \text{ m}^2$. After 7 months of data taking, the TOMUVOL collaboration obtained the transmission map in figure 2.10, from which it appeared a dense region in the upper part of the volcano [Carloganu 2013].

GRPC CALICE

GRPCs are avalanche gaseous detectors. As shown in figure 2.9, the gas is sandwiched between two glasses and a couple of graphite electrodes cover the outer part of these. When a charged particle passes and interacts inside the gas, it forms a series of ions along its path. Released electrons are accelerated under the influence of a high electric field and, at every interaction with the gas atoms, they start, with a certain probability, an avalanche. The detection of the charge is based on the difference in the drift velocity of electrons and ions. In fact, the charge released in the avalanche induce a current that is detected by copper pads, while the effect of ions current on the induced current is negligible. The current flowing through a pad is proportional to the number of charge carriers in the corresponding cluster [Bedjidian 2011]. The use of pads allows for direct recording of the event coordinates, while working with the plastic scintillators is required a couple of strips that been crossed to 90° provides the coordinates of a given event.

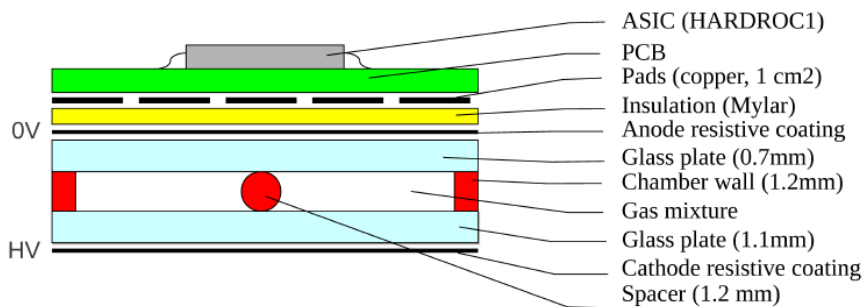


Figure 2.9: Schematic of a GRPC [Bedjidian 2011].

The TOMUVOL detector (fig. 2.11) is composed by 4 planes of 1 m^2 area. It has a great segmentation with ~ 9500 channels per plane and has resolving time of 200 ns. It is a low cost and low power consumption detector. A general clock is distributed to all 48 boards used to detect and record event. Each recorded event reports two coordinates and a precise timestamp. Tracks are reconstructed by putting in time the events and aligning them coordinate values through the 4 planes.

This kind of detector allows for great resolution. Anyway, it could suffer of gas leakages and, due to the use in outdoor condition, the variation of the temperature and humidity conditions has effect on detection performances [Lesparre 2012].

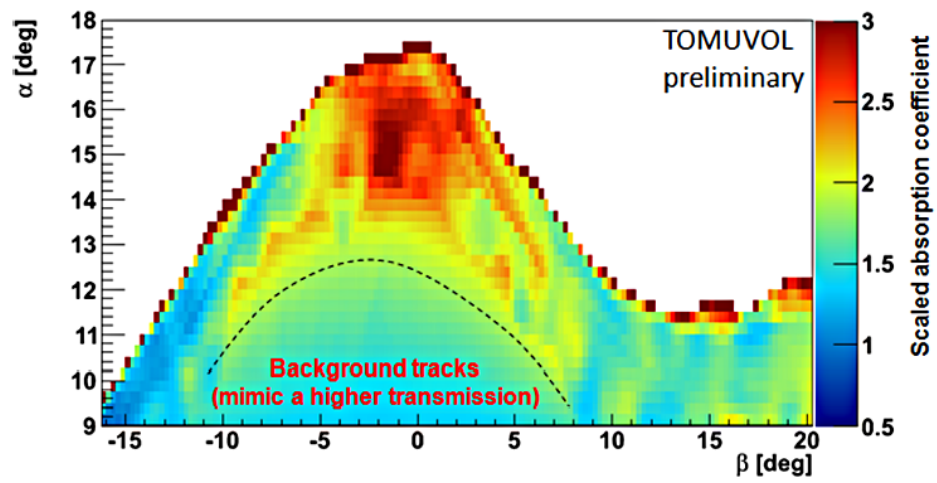


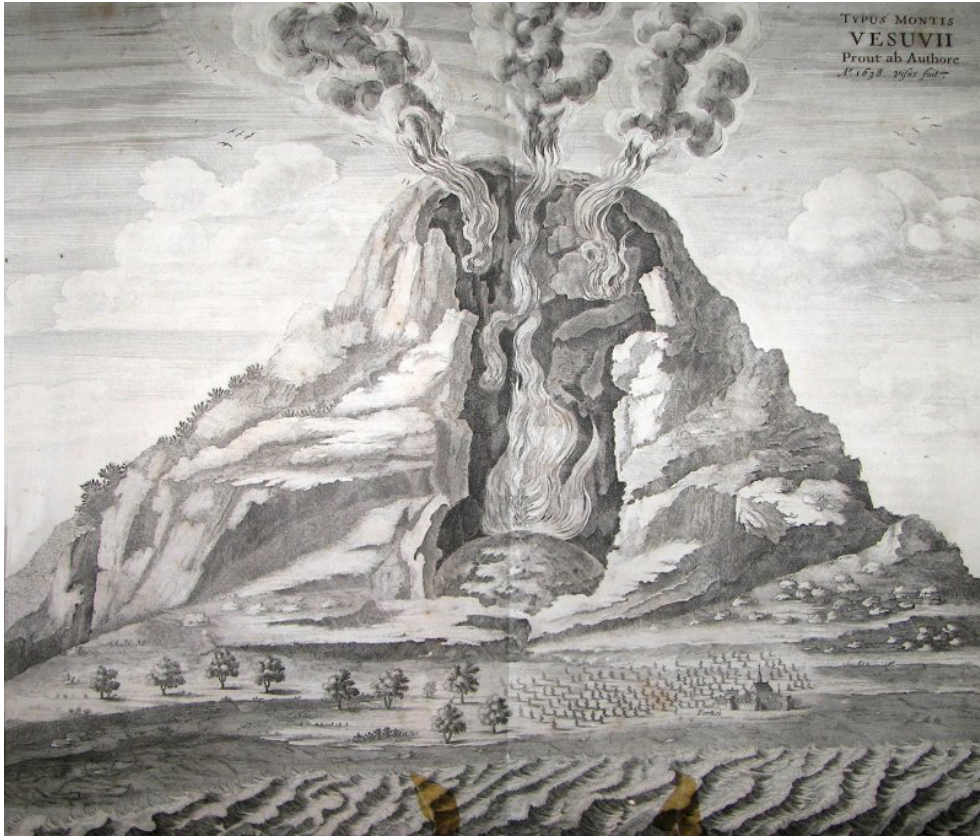
Figure 2.10: Map of the scaled transmission through the Puy de Dôme [Carloganu 2013].



Figure 2.11: The TOMUVOL detector.

Part II

THE MU-RAY MOUN TELESCOPE



3

DETECTOR DESIGN, CONSTRUCTION AND PERFORMANCES

The Mu-Ray experiment aims at the construction of a new kind of particles detector based upon silicon photomultiplier (SiPM). These are a new generation of photosensors, sensitive to a single photon, based on avalanche silicon photodiodes that works in Geiger mode and arranged in arrays of them. With the Mu-Ray detector will be possible to design new technique for tomography, obtaining three-dimensional stratigraphy images of the volcano's edge, and 2D imaging of a wide range of big object, with many applications from geophysics to space Physics and for civil uses.

During the month of April, 2010, we began the preliminary trials to build the test module of the detector Mu-Ray. This first step would help to understand how to assemble together all the parts that form the basic module, defining precise procedure to adopt during the building, and to study its performances, ruggedness and portability. Moreover many tools has been developed to speed and simplify the production line.

The basic module is composed by extruded plastic scintillator coupled with optical fibers. The latter are collected into a connector granting the placement for the readout. The first activities concerned the optimization of the optical coupling between fiber and the scintillator bar. It has been made many tests with different optical epoxy glues, often using different mixing ratio in respect of the original formulas. This phase was crucial to determine what glue gave us best performance in the light collection. Many samples showed poor adhesion of the glue on the container walls and on the fiber and in the most cases, sooner or later, fractures and bubbles were formed (fig. 3.1 a, b, c). These defects have negative effect on the propagation of light in the interface between the scintillator and fibers, which affect the transmission of light to the readout device (fig. 3.1 d, e).

Then, we worked on the coupling between fibers and photosensors. In order to ensure the best detection of light, which is collected and transmitted by optical fibers, we had to check the goodness of the manufacture of optical connectors. It has been designed and realized a test facility that used a digital microscope whereby we checked the quality of all connectors and measured the diameter, alignment and relative displacement of holes delegated to contain the fibers. We determine the alignment of all fibers and their placement inside the connector holes with a precision better than 50 μm .

Moreover, before proceeding to the construction of the detector, it was necessary to work and prepare all the materials we needed. We cut the fibers to the required length, spattered one of the two terminations of each fiber and protected them by applying a solid glue on those endings. We also cut, drilled and washed about 400 scintillators.

From April 2011 until February 2012, the main activities in the Mu-Ray experiment concerned the design, the construction, the test and characterization, and the commissioning of the Mu-Ray detector in two different sites. In 2013, the telescope has been assembled on the Vesuvius to perform a preliminary data taking. Since the first check on the data acquisition is to image the external shape of the volcano [Tanaka 2012], we took the shadow of the Vesuvius (Napoli, Italy) during the first week of acquisition (fig. 3.22). It was a good testing ground for checking the quality of all systems, to recognize malfunctions and to

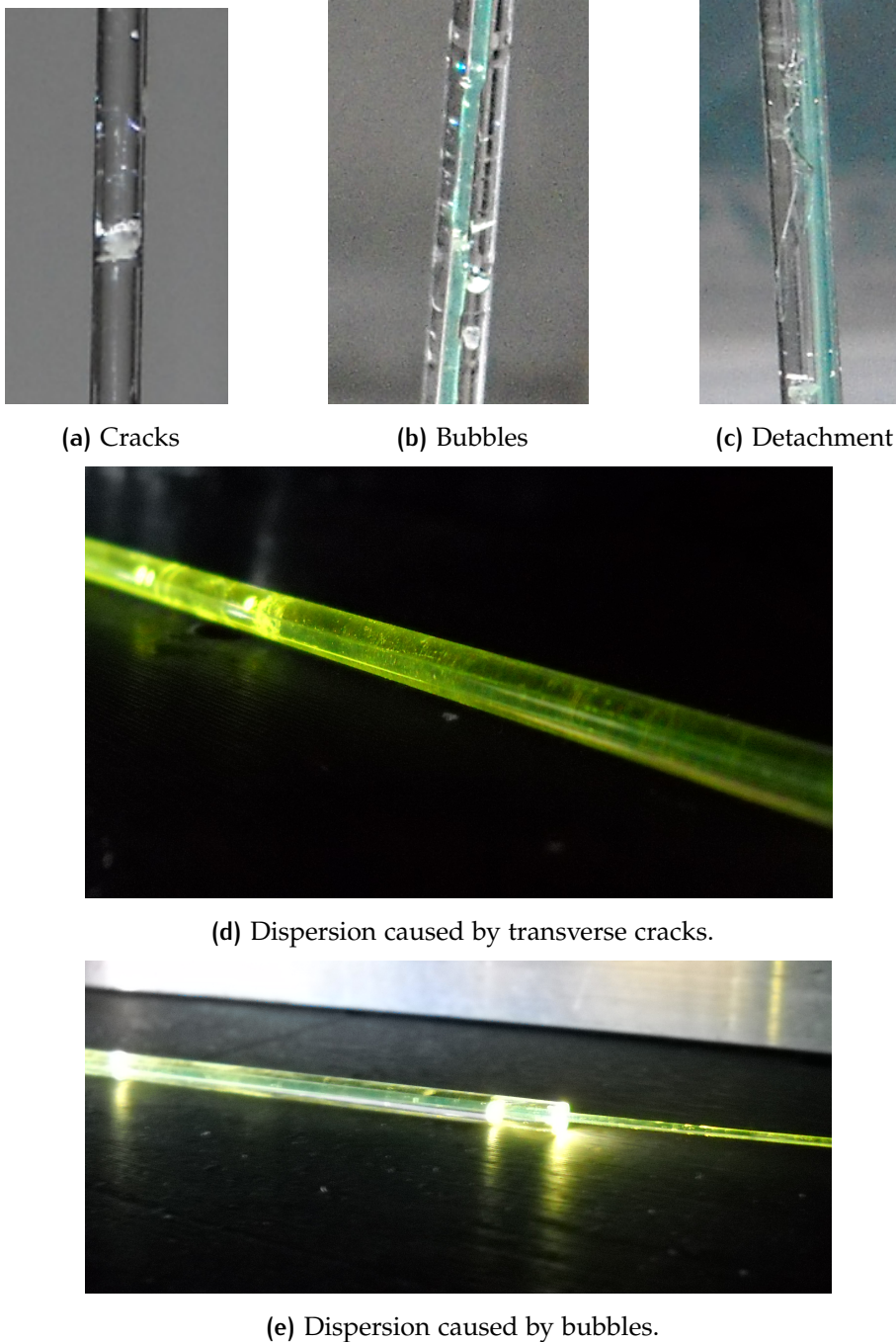
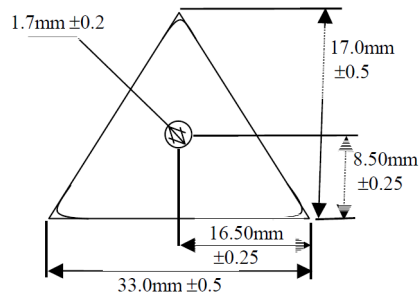
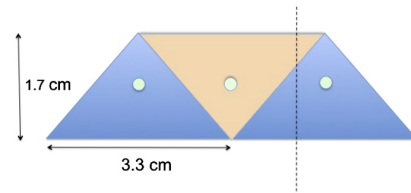


Figure 3.1: Glue's defects and the related effects on light collection.

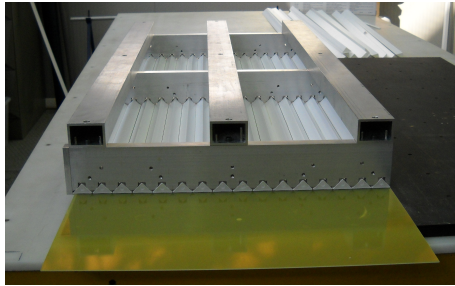
leave the detector without the human intervention. Moreover, due to power cuts and the commissioning of an uninterruptible power source (UPS), we substitute the PC with the System-on-Chip (SoC) based credit-card-sized single-board Raspberry Pi (RPi), that we remotely access with SSH connections. The RPi has been equipped also with Apache 2 and MySQL servers and a web page was made available on the internet to provide real-time information on the status of the data taking and sensors. Finally, in the begin of June we provided to transfer the entire apparatus in France, where we did the muon radiography of the volcano Puy de Dôme from July until the end of November.



(a) Triangular shaped extruded scintillator with co-extruded hole designed for MINERvA experiment.



(b) Scintillators placement.



(c) Tool designed to fasten 16 scintillators on the sheet of vetronite.



(d) Optical glue injected with syringes.

Figure 3.2

3.1 THE BASIC MODULE

The basic module of the Mu-Ray detector is made by 32 plastic scintillators. They are arranged one beside the other and sealed between two sheets of epoxy glass (Vetronite). Within each of them is glued a WLS fiber and all the 32 free terminations are grouped together in a connector of black plexiglass.

We used extruded plastic scintillator with a co-extruded hole (1.8 mm of diameter) and coated with reflective TiO_2 , produced at Fermilab [Bross 2001]. The shape of all scintillators is triangular (fig. 3.2 a). Using the tools conceived during the prototype module assembly, we fix 16 scintillators on a sheet of Vetronite (fig. 3.2 c), then we glued other 16 scintillators, with the base facing upwards, placing each one of them between two scintillator belonging to the pasted plane (fig. 3.2 b). In the meanwhile, we provided to place and secure 32 WLS fibers to the plexiglas housing, called optical connector. Also the attachment of the fibers to the optical connectors has been realized with the aid of a tool designed to ensure the correct positioning of the fibers. The end of each fiber should protrude $\sim 200 \mu\text{m}$ from the hole in which is housed and must not remain inside. Once the two parts of the module are ready, we proceed to insert each of the 32 fibers into the co-extruded holes of the scintillators. The whole assembly is ensured to a vertical plane and the optical connector is fixed to the upper edge of the epoxy glass. We filled the co-extruded hole, injecting with a syringe $\sim 8 \text{ ml}$ of optical glue. The injection happened from the bottom of the scintillators (fig. 3.2 d), stopping when the glue dropped out from the upper part. This procedure grants that the product is bubble free.

Once the glue's cure time passed, we proceeded to fix the optical connector to the Vetronite sheet (fig. 3.3 a) and close the module with another sheet of the same material. The module is completed and must be wrapped with Aluminum adhesive tape, leaving free only the part from which protrude the fibers (fig. 3.3 b). Thus 12 modules were build and stored (fig. 3.3 c), ready to be mounted on the detector's frame.

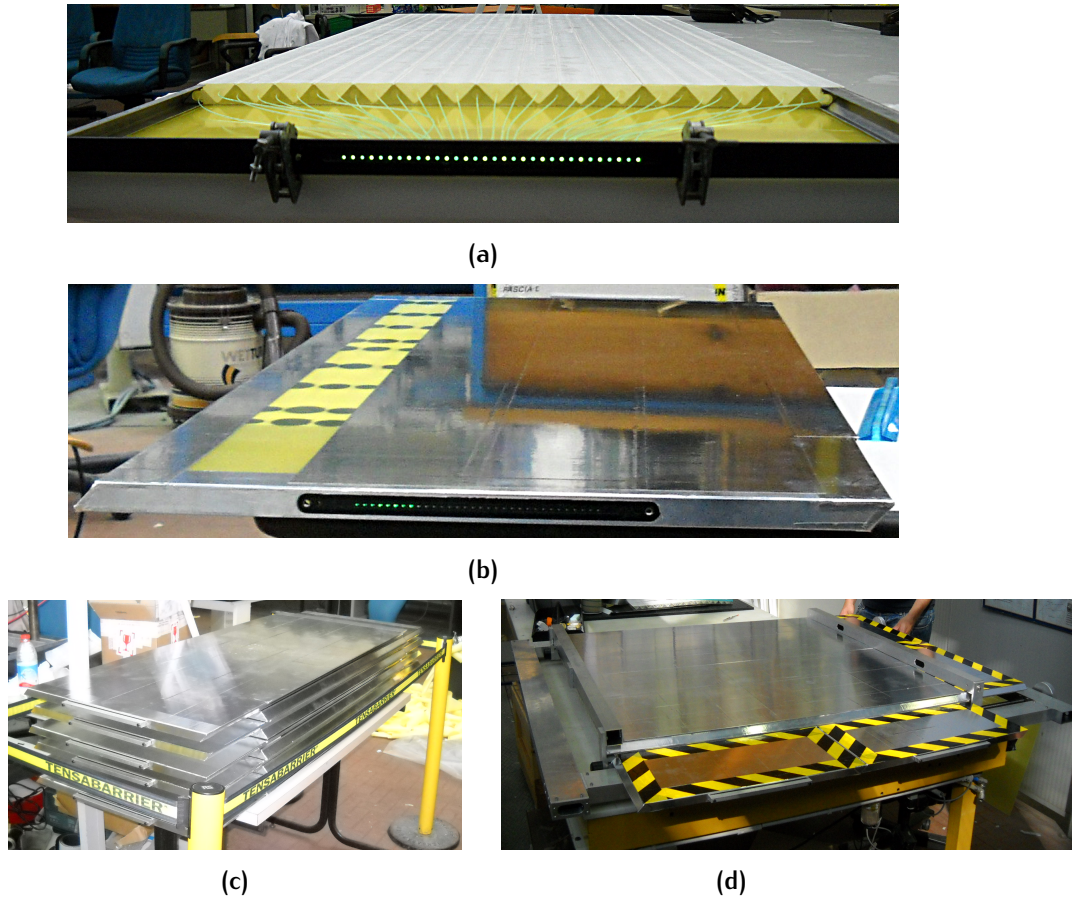


Figure 3.3

3.2 MOUNTING MODULES ON THE CHASSIS

An aluminum chassis has being designed and developed to host 12 modules, arranged in 3 planes. The structure is fully demountable and easy to store in a box for transportation. It is composed by a parallelepipedal frame, resting on a rotating base and wherein the modules are place on three sutable supports. Each support mounts four modules, disposed in two couple forming the X and Y view of the plane (fig. 3.3 d). The chassis also mount a 3 mm thick iron shield. The dimensions of the detector are $156(h) \times 160(l) \times 135(w)$ m³ and the total weight is less than 600 Kg, were each assembled plane is ~ 100 Kg heavy.

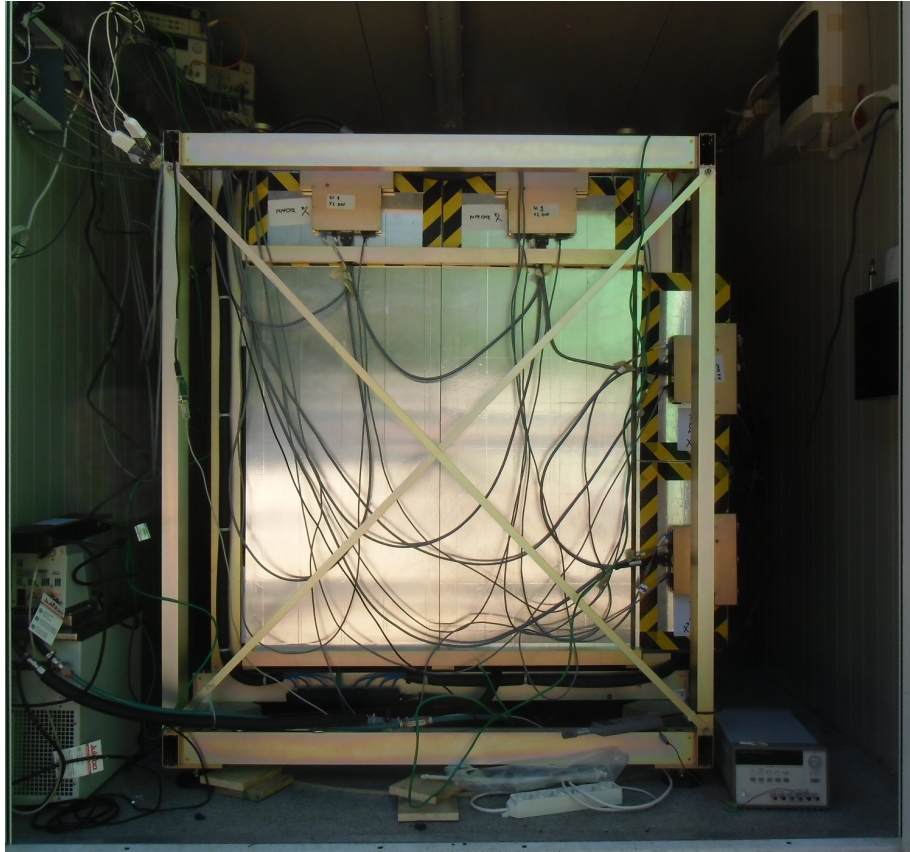


Figure 3.4: Frontal view of the Mu-Ray detector. Modules are mounted on movable stand and disposed to form the X – Y plane.



Figure 3.5: Lateral view of the Mu-Ray detector. In the middle are placed the third plane and the iron shield for low energy charged radiation.

3.3 THE SILICON PHOTOMULTIPLIERS

Like a PMT, the Silicon Photomultipliers are photosensors capable to reveal the single photon, with the advantage to have a lower power consumption than its predecessor. SiPMs are actually employed in a lot of experiments where the robustness, the low-space and low-power consumption, durability and no handling are required.

SiPMs are commonly related to Geiger-mode avalanche photodiodes (GAPD), since they are a matrix of APD linked in parallel and working in Geiger-mode¹ (fig. 3.6). In the absence of light, the SiPM has an applied reverse bias V_{bias} that exceeds the breakdown voltage $V_{breakdown}$. Thus, when an electron-hole couple is created, the avalanche starts giving rise to a plasma flowing through the fired APD. The amount of charge measured at the SiPM terminals is $10^5 \div 10^6$, where the output A depends on the sum of the single APD's signal amplitude. The gain A_i of a single APD is proportional to the overvoltage $V_{ov} = V_{bias} - V_{breakdown}$.

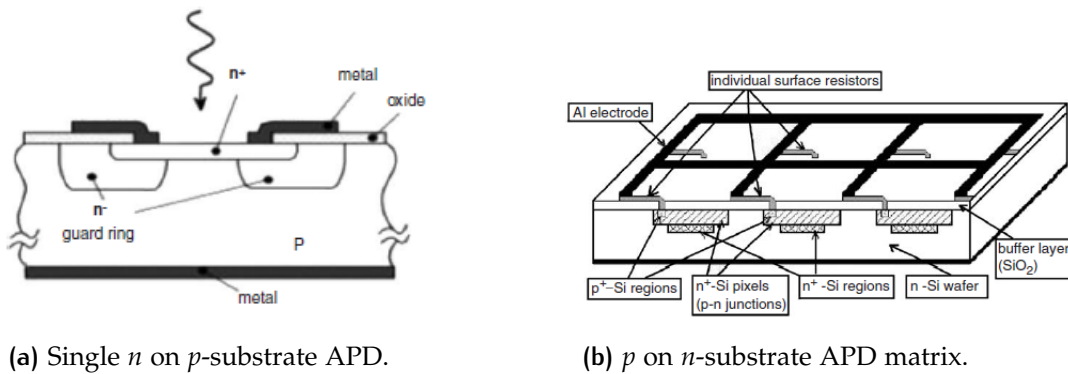


Figure 3.6: SiPM inner structure.

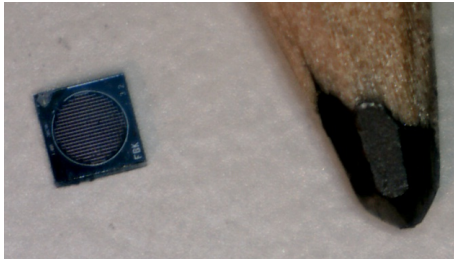
Thermal changes produce variation in the breakdown voltage of about $50\text{mV}/^\circ\text{C}$, the gain and the photon detection efficiency (PDE) vary of some percent per Celsius degree following these changes. Moreover, the so-called dark counts are induced by thermally generated carriers producing a breakdown with a rate of few MHz/mm^2 at 25°C , where the rate increases by a multiplicative factor 2 for each increase of 8°C . Dark counts are produced also by the tunneling of free carriers, which under the effect of the electrical field acquire enough energy to generate an avalanche [Renker 2006].

The PDE is the product of the quantum efficiency, the trigger probability² and the geometric factor. The quantum efficiency depends on the wavelength of the light and the geometric factor has a percent value around the 50%. The percent value of the trigger probability, however, depends on the overvoltage and the position where the first electron-hole generation takes place inside the APD. In the single photon counting regime, the output $A \propto \text{PDE} \times N_{ip}$, where N_{ip} is the number of incident photons.

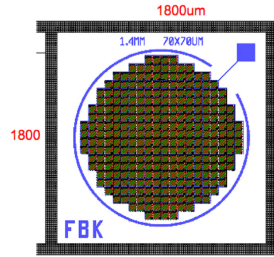
¹ The Geiger-mode is such that, under the influence of the applied reverse bias, charge carriers multiply faster than they are being extracted. This implies an exponential increase of the number of electrons, and also of the number of the holes, able to generate new free charge carriers, until the quenching mechanism stops the flow and resets the single APD.

² The trigger probability is the probability of a photoelectron to generate an avalanche.

The Mu-Ray detector mounts ~ 400 SiPms produced by FBK-IRST (fig. 3.7 a, b). These are compact and robust devices with circular active area of 1.4 mm diameter. Each SiPM has 292 pixel with area of 70 mm^2 and consumes $\sim 10 \text{ }\mu\text{W}$ of power.



(a) Magnification of one of the SiPM produced by FBK-IRST for the experiment Mu-Ray.



(b) Schematic layout of a FBK-IRST SiPM.

Figure 3.7

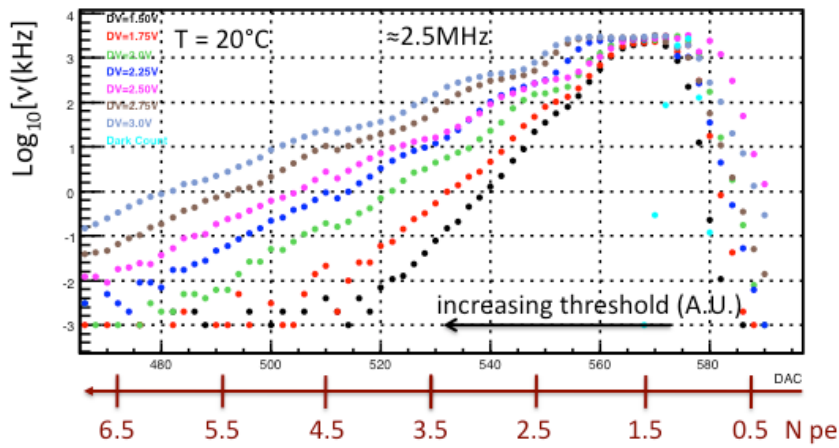


Figure 3.8: Experimental dark counts rate in function of the discriminator threshold fir different overvoltages.

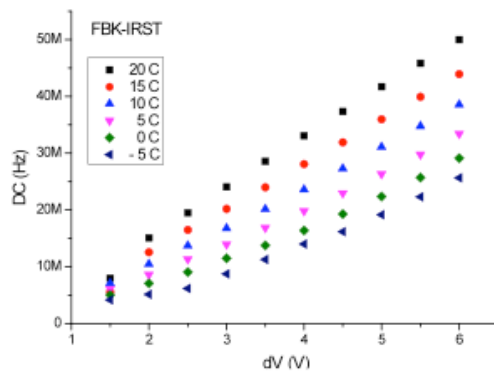


Figure 3.9: Experimental dark counts rate in function of the overvoltage for different temperature.

3.4 HYBRID BOARD FOR SiPMs

A so-called hybrid board has been developed, so that on the same surface are hosted 32 SiPM and 2 temperature sensor Pt1000. The board was realized in capton and G10 and designed to dispose the 32 housed SiPMs in front of the fibers, secured to the optical connector. The necessity to have a single support for more than one SiPM regards the thermal conditioning need of these devices. Tanks to the Pt1000 sensor we can continuously monitor the temperature of the SiPM. Moreover, a series of blind vias conduce the heat between the two sides of the board. On the opposite side to the SiPMs housing, there is a plate of copper that we use to apply the thermal conditioning.

We are able to implement two modes of operation. In a first one, SiPMs work at fixed temperature. This can be done with a chiller or with some other suitable device, like Peltier cells, that balance the internal temperature changes induced by the external conditions, consuming electrical power. The other method is to compensate the temperature variations with bias voltage changes, to keep fixed the overvoltage of the SiPM. Both methods has been tested during laboratory's trails and the measure campaign at Mt. Vesuvius.

3.5 TEMPERATURE CONTROL OF THE SiPMs

A water chiller system has been used during the most part of the activities of the Mu-Ray detector. Its high power consumption, make it suitable for laboratory uses or in situations of use in which it is provided the appropriate distribution of electricity.

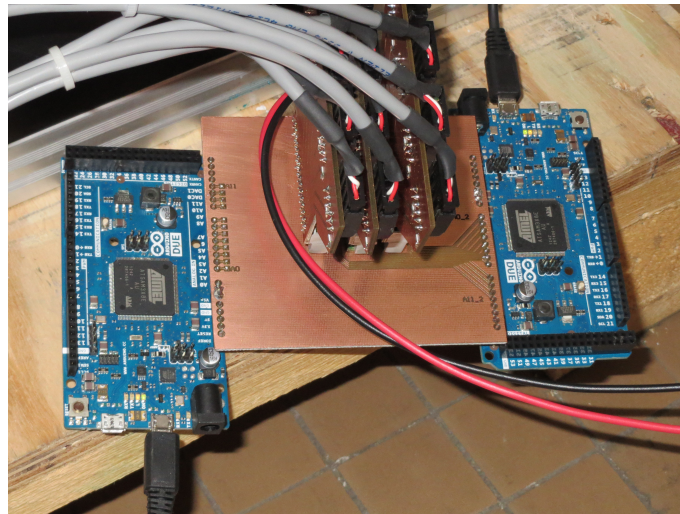


Figure 3.10: In order to monitor the temperature of each SiPM, it has been developed a local monitor board with a couple of Arduino Due boards, an off-the-shelf microcontroller board with 12 ADCs with 10 bit resolution (0.15°C sensitivity).

The entire hydraulic circuit was designed and developed so that the water recycling happen without stagnation. A thermal exchanger (fig 3.11), realized with a copper base to ensure the best heat transmission, has the task of lock the hybrid board against the optical connector. To soften the contact surfaces were used an O-ring on the SiPMs side and a thermal adhesive silicon to couple the heat exchanger with the thermal plate of the hybrid.



Figure 3.11: Top and bottom view of the heat exchanger. It was realized gluing with Araldite an Inox bar with a copper base. The upper part and all sides are caulked with Armaflex insulator.

Figure 3.12

We have carried out several tests to prove the reliability of the cooling system. In particular, we verified that the water flowed to each node of the circuit, determining the placement of the fittings and of the exchangers allowed by the minimum pump pressure of the circulator (fig. 3.15 b). Prior to this, we measured the uniformity in temperature of the SiPMs housings, under thermal conditioning (fig. 3.15 a). We found a good uniformity in temperature measured on the right and left sides and in the middle of the housing plate. As shown in figure 3.14, when the chiller shutdown the system holds the temperature uniform and, due to thermal insulation it takes more than 2 hours to go at equilibrium with the environment. The temperature measured on the hybrid and the temperature of the water, recorded by the chiller, differ up to $\sim 1^\circ\text{C}$ (fig. 3.13). During our campaigns, we recognized the same phenomena, with ΔT reaching sometimes even 2°C .

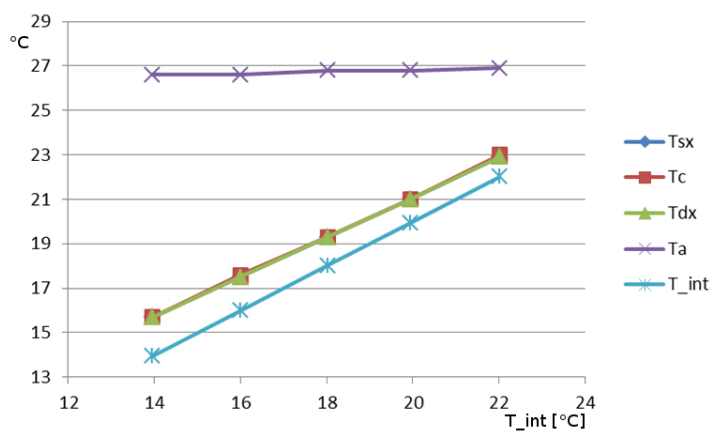


Figure 3.13: Plot of the SiPMs temperature versus the temperature set by the chiller. The test started at the environmental temperature.

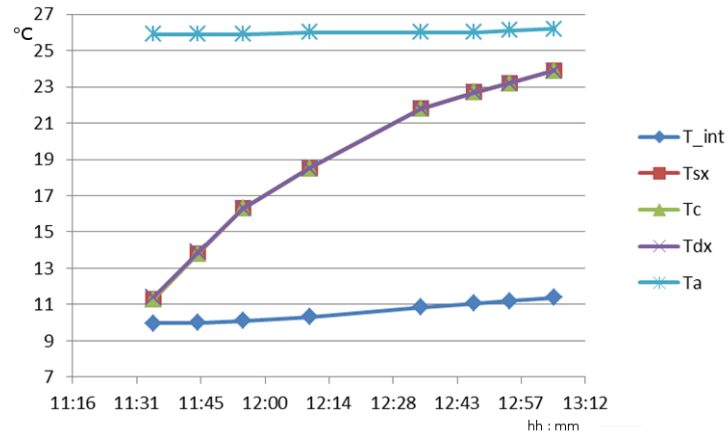
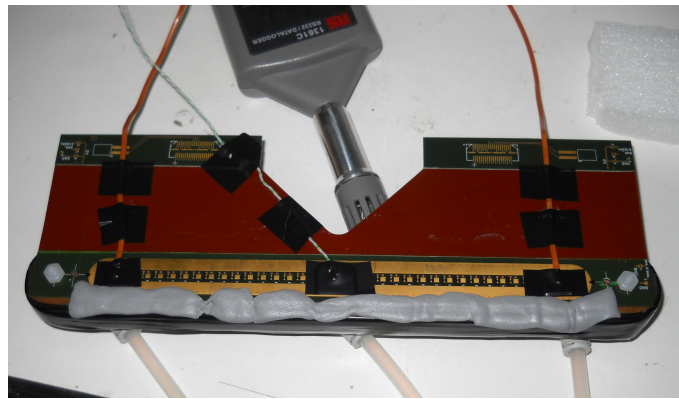


Figure 3.14: Plot of the temperature when the system moves to room temperature, without thermal conditioning.



(a) Experimental setup to check the temperature uniformity of the SiPMs housing plate with water chiller cooling.



(b) Hydraulic circuit test configuration.

Figure 3.15: Laboratory tests for the reliability of the cooling system. The heat exchangers and other parts of the hydraulic circuit were mounted on the chassis.

3.6 FRONT-END ELECTRONICS AND DATA ACQUISITION SYSTEM

The readout of the SiPMs is done with a set of dedicated electronic slave boards (fig. 3.16 a), which mount a SPIROC (Silicon Phomultipliers Integrated Read Out Circuit)³ ASIC [Conforti Di Lorenzo 2013], coordinated by a master board (fig. 3.16 b). Each SPIROC provides to read the set of 32 SiPM hosted by the corresponding module. It allows to setup 32 independent V_{bias} for each SiPM using 8 bit DACs and a common threshold with a 10 bit DAC. Two amplification and formation chains are available for every channel. A first one is used in a logic circuit to produce the trigger signal in the master board; a discriminator gives a logic signal every time the amplitude of at least one SiPM's signal exceed the threshold. The other chain record the maximum tension taken by the signal and store this value in an analog memory using a track and hold circuit. This measures the amount of charge released by the SiPMs. In the case of a trigger sent by the master, the 32 values stored in the SPIROC are converted by an on-board 12 bit ADC and uploaded to the master board's memory. Both master and slaves boards mount a XILINX SPARTAN II FPGA for logic functions.

Each board is provided with a circuit involving the time expansion technique. It is used to measure the TOF of the muons and represents one of the main features of the Mu-Ray Detector. Moreover, the slave boards are low power consuming and it works in two modes, RUN and DIAG, to reduce the power consumption due to the clock. The total power consumption of the front-end electronics is $\sim 20 W$.



(a) Slave board



(b) Master board

Figure 3.16: The Mu-Ray front-end electronic boards.

Finally, after a trigger logic has been satisfied, the master download one by one all slaves buffers and makes them available to be downloaded from a computer. The master board is equipped with a PIC microcontroller implementing a USB 1.1 interface. The communication between the master board and the computer is carried out through this interface. A program, written in c language, allows to configure the front-end electronic for the data taking, reads the master memory and stores all the data in raw format. The latest version of the program features the use of text file data-cards. The latter are really useful because the changes to the run configuration can be applied without recompile the program.

³ <http://omega.in2p3.fr/index.php/products/spiroc.html>

3.7 PERFORMANCES AND CHARACTERIZATION OF THE DETECTOR

The assembly of the module allows to have a segmentation of $\sim 3 \text{ cm}^2$. Since the distance between two neighboring fibers is 16.5 mm and we know that a particle passes between them within a maximum uncertainty of $\frac{16.5 \text{ mm}}{2} \approx 8.3 \text{ mm}$ with respect to the middle point. The distribution of the particles passing in this interval is uniform, thus the statistical error on the hit position is $\frac{8.3 \text{ mm}}{\sqrt{12}} \approx 2.4 \text{ mm}$. Placing the front and back planes at a distance of 1 m the achieved angular resolution is 8 mrad and the spatial resolution, imaging an object 1 km away, is 8 m. Moreover, the power consumption of the detector, tacking into account only the front-end electronics ($\sim 20 \text{ W}$), the SiPMs ($< 1 \text{ W}$), the RPi (3 W) and the slow control ($< 10 \text{ W}$), amounts to $30 \div 40 \text{ W}$.

The use of a fast front-end electronics allows for high time resolution. When a certain logic is satisfied, the master board send a trigger to all slave boards and distribute a 100 MHz clock signal, that corresponds to a period of 10 ns. Since the the Mu-Ray detector measure the TOF by means of a time expansion circuit with expansion factor 30, we found a time resolution of $\frac{10 \text{ ns}}{30} \approx 0.3 \text{ ns}$.



Figure 3.17: The Mu-Ray detector's planes have been mounted in horizontal to make a precise calibration of the detector.

For the characterization of the detector, the 3 planes have been disposed horizontal arranged as in figure 3.17, because of the abundance of the vertical muons flux. After estimating the rate of accidental coincidences and measuring the trigger efficiency, we measured the flux of muons within the detector acceptance in this configuration.

The working point of SiPMs has been set in order to make them dark-rates of few KHz par channel, requiring that the total rate per module is of less 100 KHz. By using the 8 bit and 10 bit DAC we adjusted, respectively, the SiPMs overvoltages and trigger efficiencies and the threshold of the 32 channels. The goal is to maximize the overvoltage in order to have more gain and choose a threshold value small as possible to enhance the trigger rate. But increasing the overvoltage, it also increases the dark-rate and small threshold values imply an increase of the number of events triggered by noise. An underestimation of the rate of accidental coincidences in the configuration of 6 planes trigger, with a resolving

Trigger Logic	counts	RMS	Efficiency [%]
6PTL	1933.60	141.74	-
5PTL - P ₁	2235.40	30.68	87
5PTL - P ₂	2337.20	29.89	83
5PTL - P ₃	2285.80	40.20	84
5PTL - P ₄	2081.00	57.97	93
5PTL - P ₅	2188.60	74.68	88
5PTL - P ₆	1953.60	92.98	99

Table 3.1

time of 40 ns, is $\sim 2^7 (100 \text{ KHz})^6 \times (40 \text{ ns})^5 \approx 10 \mu\text{Hz}$, that is compatible with the experimental value recorded by a test made putting in coincidence sectors of the detector that are not aligned. During this test, lasted 36 hours, we hadn't recorded any event.

To measure the trigger efficiency of the detector, we setup a 6 planes trigger logic and six different 5 planes trigger logic, so that one at a time planes are excluded from the trigger logic and we counted the number of coincidences, for each of the seven configurations. The trigger efficiency of the detector is the product of the efficiency of each plane and the plane efficiency is the ratio of the trigger counts in 6 planes logic to the trigger counts in 5 planes logic, where the plan that is excluded from the trigger logic is precisely the plan we want to evaluate the efficiency. Form table 3.1 we had, using the first generation of SiPMs (2012), a trigger efficiency of about 50% at 2 V overvoltage; the figure 3.18 shown the trend of the efficiency for different overvoltage values. Anyway, SiPMs have been changed during 2013 and the new trigger efficiency is $\sim 78\%$, with planes efficiencies greater than 95% [Ambrosino 2013b].

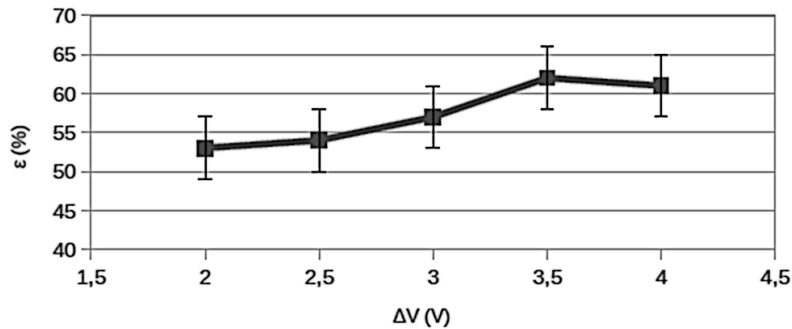


Figure 3.18: Chart of the overall trigger efficiency of the detector, including geometrical acceptance, in function of the SiPMs overvoltage.

Finally, we proceeded to acquired vertical muons in order to study the reconstruction performances. We reconstructed and analyzed the muons tracks that crossed the detector and we compared the zenith angle distribution with the expected one. The latter has been obtained simulating vertical muons according to the theoretical distribution. Their angular distribution has been obtained using the same algorithm of the reconstruction of the tracks. As shown in figure 3.19, the expected and the measured distributions was in agreement.

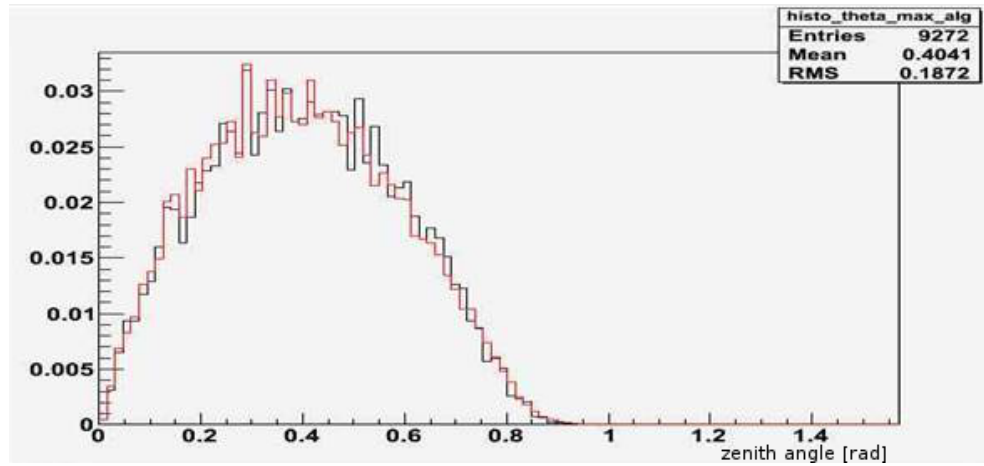


Figure 3.19: The comparison between the measured flux of muons as a function of the zenith angle (black in the chart) and the expected one assuming the $\cos^2\theta$ dependence of the flux on the zenith angle (red) showing a good agreement [Ambrosino 2013b].

3.8 THE REMOTE AUTOMATED SYSTEM MUBOT

In view of the campaigns at Vesuvius and the Puy de Dôme, we developed the remote automated system MuBot. It is installed on the minicomputer RPi and is completely written in python 3 language. The data acquisition system, the slow control and other controls run under the supervision of MuBot as shown in the diagram in figure 3.20.

One of its features regards the implementation of a not-clocked watchdog. A basic watchdog is a timer that waits to recognize a reset signal by the computer; if a failure occurs, the watchdog reaches the timeout and reset the computer. Both the computer and the watchdog are synchronized by the same external clock. Differently from the classic scheme, we equipped our system with a software that has the same behavior, but without use an external clock. In our implementation, the watchdog runs in an autonomous thread and when the timeout is reached, the watchdog checks the timestamp of the last operation. If the timestamp exceed the timeout, then it resets all the front-end electronics and restart the acquisition.

Other features regard the MuBot's capability to control via USB connections all the power supplies used by the detector, to monitor environmental temperature and humidity, to acquire data relative to the SiPMs temperatures from the local monitor board (in figure 3.10), to check the working condition of the water chiller. The system can detect malfunctions which can occur in these activities and report the errors sending mail to the researchers, whenever their intervention would be required. This system has worked continuously during the period of data taking at Vesuvius and the Puy de Dôme, and even when power cuts occurred, the system has rebooted autonomously when the supply of the electrical power was restored.

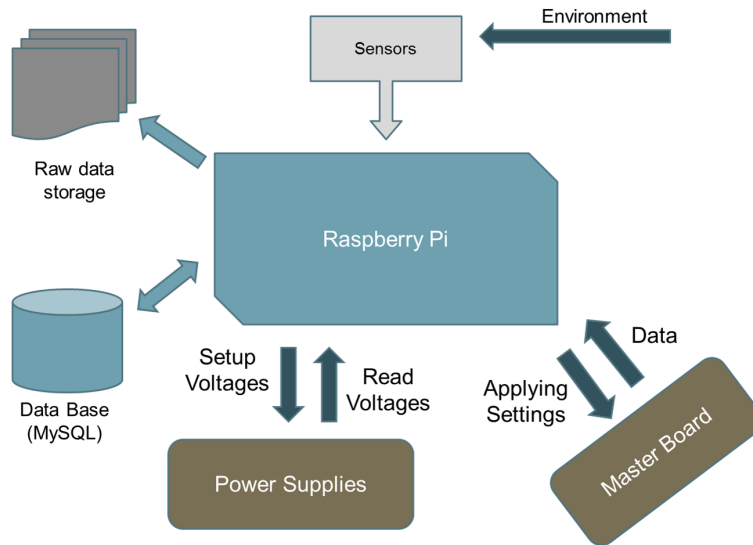


Figure 3.20: Logical schema of the remote automated system MuBot.

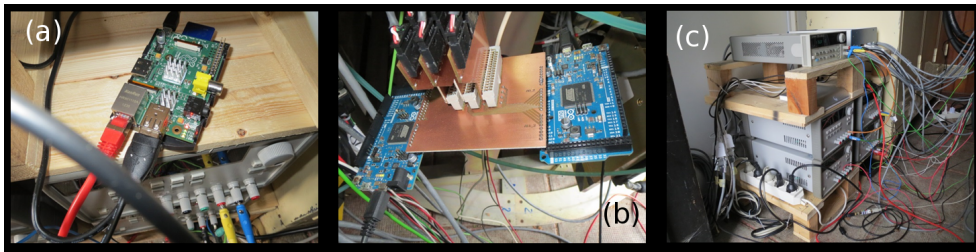


Figure 3.21: Some parts of the remote automatic system used at the Puy de Dôme: (a) the Raspberry Pi computer; (b) Arduino local monitoring board; (c) power supplies.

3.9 CAMPAIGNS AT MT. VESUVIUS AND AT THE PUY DE DÔME

In the month of March, 2013, we started a preliminary tests campaign on the Mt. Vesuvius and then in July we provided to move the apparatus on the Puy de Dôme. The Puy de Dôme has a rock thickness comparable to the geological edifices scanned by Japanese researchers. In both campaigns we transported and assembled the detector in the chosen sites, using a pickup or a small truck. Operations took two or three days each time, depending on the weather conditions, the volume of the transport and the number of operators.

The Mt. Vesuvius was the first employment of the detector in out-of-lab activities. It was assembled in a container with supplied with electrical power (fig. 3.9). Anyway, due to the frequent power cuts, we provided to mount an UPS. During all the data acquisition, supported by the capability of MuBot to adjust by itself the V_{bias} of the SiPM in function of the SiPM temperature variation, we tested the measurement approach which does not require the use of a chiller and , after few days of data taking, we reconstructed the map of the transmission of the volcano (fig. 3.22). Because of some problem occurred in this period, we developed the most part of the automated remote system to avoid malfunctions due to failures regarding the whole system. Often the internet connection wasn't available, not allowing access to the system, even for a few days. In this case it wasn't possible to monitor the data taking and the proper operation of the apparatus.

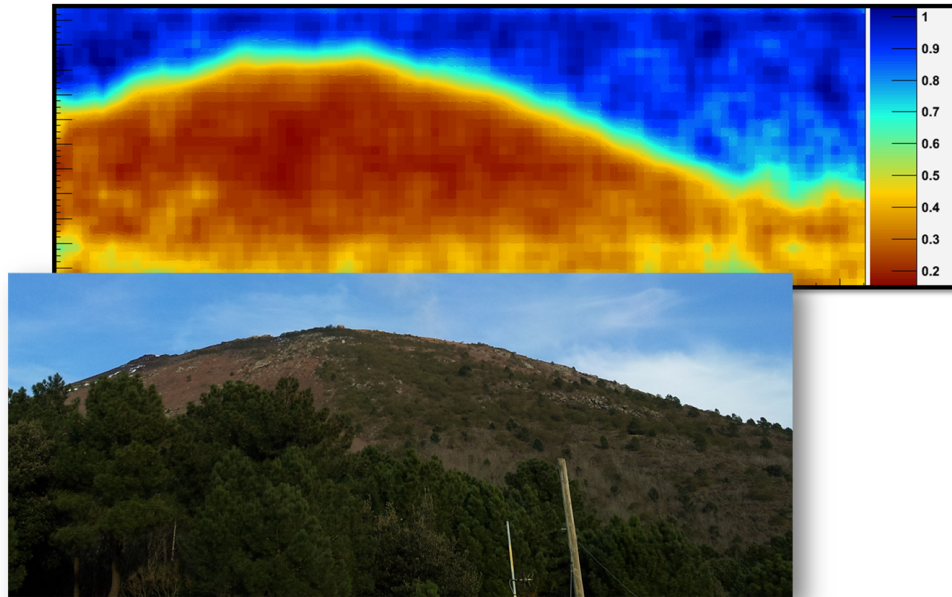


Figure 3.22: The transmission map of the Vesuvius (Napoli, Italy). The shape of the shadow can be compared to the picture of the volcano taken from the observation point.

From the begin of July 2013 until the end of November 2013, we had the measurement campaign on the Puy de Dôme. Differently from the Mt. Vesuvius campaign, we used the water chiller because of the presence of a reliable power source and the location provided a stable ADSL internet connection to access the system from remote locations. The method adopted is to set the working point of the SiPMs in order to have a dark-rate of order of few KHz per channel. In the case of the Mu-Ray detector, due to the use of SiPMs, the contribution of the dark counts to the rate of accidental coincidences is not negligible. So, we need to reduce this rate by finding a proper working point and constantly monitoring the trigger rate. The Mu-Ray system allows to check the quality of data by running specific tasks that once in awhile acquire pedestal and measure the board rate during data acquisition. The stability of the data acquisition has been monitored constantly by measuring the trigger rate (fig. 3.23)

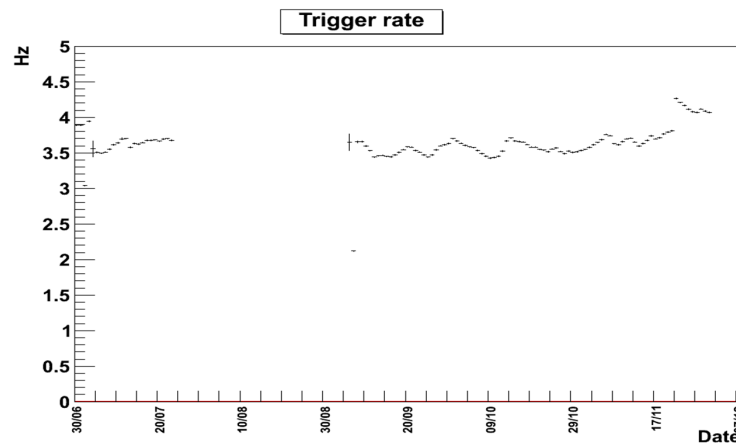


Figure 3.23: Trigger rate during data acquisition at the Puy de Dôme.

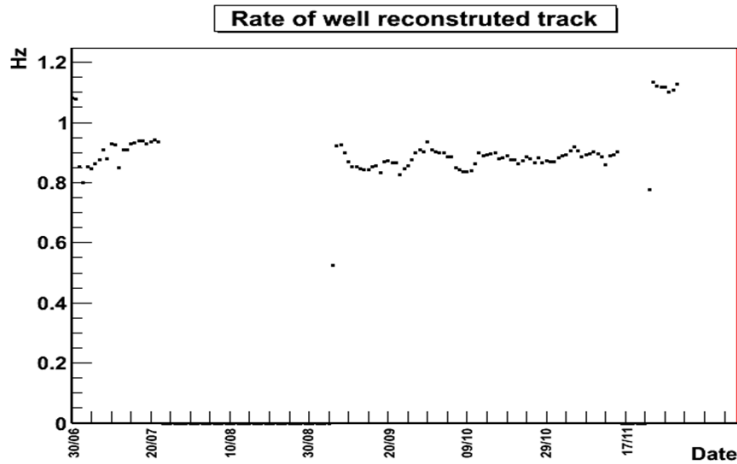


Figure 3.24: The rate of golden tracks.

From the point of view of the Col de Ceysnat (alt. 1078 m), we had about two weeks of *free sky* data taking, one at the begin and the other one at the end of the measurement campaign. The latter lasted about 4 months in which we collected about 30×10^6 trigger events. The number of tracks has been decreased to 6×10^6 by applying the analysis constraints. The survived tracks constitute the so-called *golden tracks* sample and their rates have been reported in figure 3.24. We measured a rate of golden tracks of about 1 Hz. Finally, we map the transmission of the muons flux through the volcano (fig. 3.25).

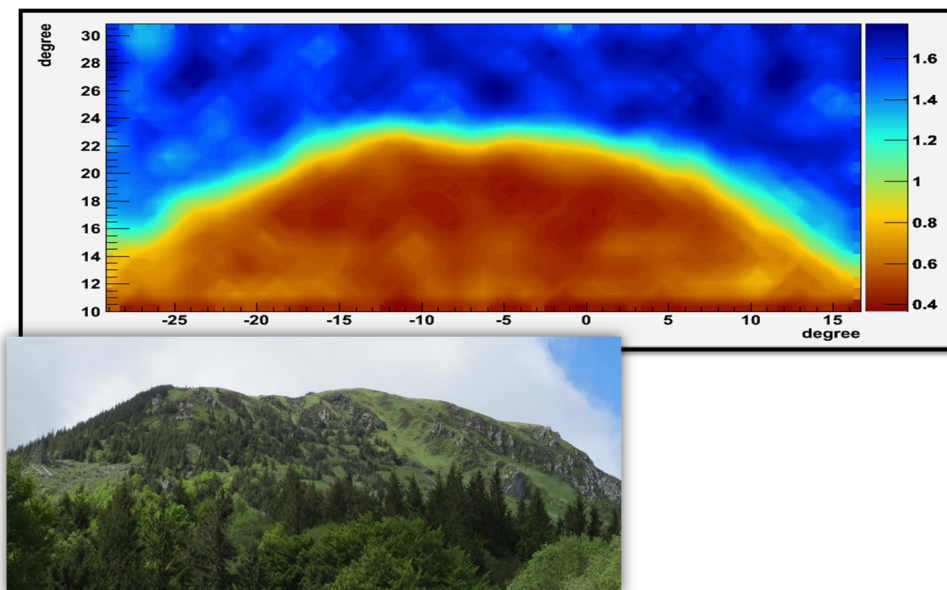


Figure 3.25: The transmission map of the Puy de Dôme (Clermont-Ferrand, France). The shape of the shadow can be compared to the picture of the volcano taken from the Col de Ceysnat observation point.

4 | TECHNOLOGY

The Mu-Ray detector fulfill many of the muography's requests. Those that still need to be improved before a final employment are related to the low power consumption and to the TOF. In this context we need to get rid of the chiller and the most part of power supplies, with their kilowatts consumption, and to improve the electronic, providing it with unique characteristics for this type of applications.

The first upgrade, that we are actually running, is the replacement of the IRST-FBK SiPMs with newer Hamamatsu SiPMs, with sensitive area of $1.3 \times 1.3 \text{ mm}^2$. This is fundamental to reduce the dark rates of the IRST SiPMs, which in principle should amount to few MHz and instead are discovered to be of order 10 MHz. Hamamatsu SiPMs are characterized by dark rates of order 100 KHz.

Encouraged by the availability of a new ASIC belonging to the same family of the SPIROC, in conjunction with the change of the SiPMs, we have provided to upgrade the front-end electronics in order to further reduce the power consumption and to setup best performances for the new SiPMs.

4.1 FRONT-END ELECTRONIC UPGRADES

4.1.1 Improvements to the Slave Boards

The front-end electronic has been upgraded replacing SPIROC mounted on the slave boards with the EASIROC (Extended Analogue SiPM Integrated Read Out Chip)¹. The EASIROC has a simplified structure compared to the first and the register of the slow-control of the SPIROC has 456 bits, compared with 703 bits of the EASIROC. The SPIROC has also internal ADC and TDC, while EASIROC does not have them and the digital part is minimized. This allows to reduce costs and power consumption. The power consumption is further reduced in the EASIROC by the ability to turn off parts of the chip when not in use. Moreover, SPIROC has 36 analog channels while EASIROC has 32 analog channels and the analog block of the latter includes a channel mask in order to have those channel which have gone above the threshold producing a trigger, while in SPIROC is only available the logic OR of the 36 channels, the so-called OR36.

Other features of the new slave boards are

- the substitution of the XILINX SPARTAN II FPGA with the most performant SPARTAN III

¹ <http://omega.in2p3.fr/index.php/products/easiroc.html>

- the capability of using an internal power source for SiPMs thanks to a programmable voltage regulator (MAX1932) that provide supply voltages in the range from 4.5 Volts to 90 Volts (for our purposes, we limit the range to [27, 75] V)
- the ability to use a single power source to supply the entire board given the presence of linear voltage regulators, to provide required voltages for the functioning of the EASIROC and to the on-board FPGA, and switching regulators to provide -5 V and ± 12 V to the board's time expansion circuit
- the switching regulator works with a dedicated ground, to avoid the noise generated by these circuits to propagate throughout the board
- two programmable potentiometers to adjust the hold time and the timeout

In order to validate the new design of the slave boards, we proceeded to setup the 456 bit slow-control register. We characterized, for each channel, the 8 bit DAC response (fig. 4.1 a) by which we adjust the SiPM's overvoltage; the 4 bit high and low gain pre-amplifiers which provide, respectively, amplification in the ranges 10 to 150 and 1 to 15; the 3 bit slow shaper peaking time which provides the charge measurement of the channel, finding a different response (tab. 4.1 b) with respect to the values reported in the EASIROC datasheet; the 10 bit DAC that provides the threshold value common to all 32 SiPMs.

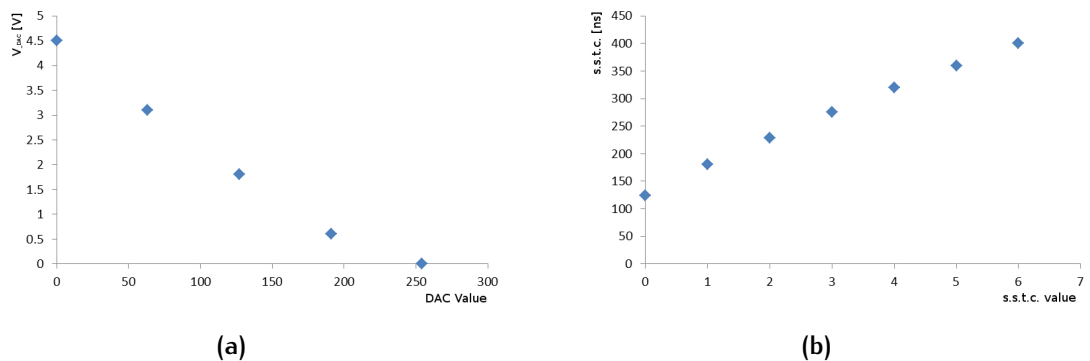


Figure 4.1: 8 bit DAC (a) and slow shaper time constant (b) responses in function of the slow control register settings

Finally we improved the time expansion circuit. Referring to a slave board, the time expansion works in order to record and digitize the time occurred between the production of a local trigger, the hold signal, and the reception of a stop signal, which in our case is sent by the master board and represents a signal common to all slave boards. The time is recorded in the form of the charge stored on a capacitor. The digitization happens by discharging the capacitor and counting the number of clock pulses up to the closing of the enable windows. The time is expanded using a different discharge circuit, with a greater time constant, in respect of the one who charges the capacitor. In the first version of the circuit, the expansion factor $E = \frac{t_{\text{discharge}}}{t_{\text{charge}}}$ was set to 10. With the upgrade we improved the expansion factor to $E = 20$ and eliminated the dead times and malfunctions. In figure 4.2 is reported the entire process.

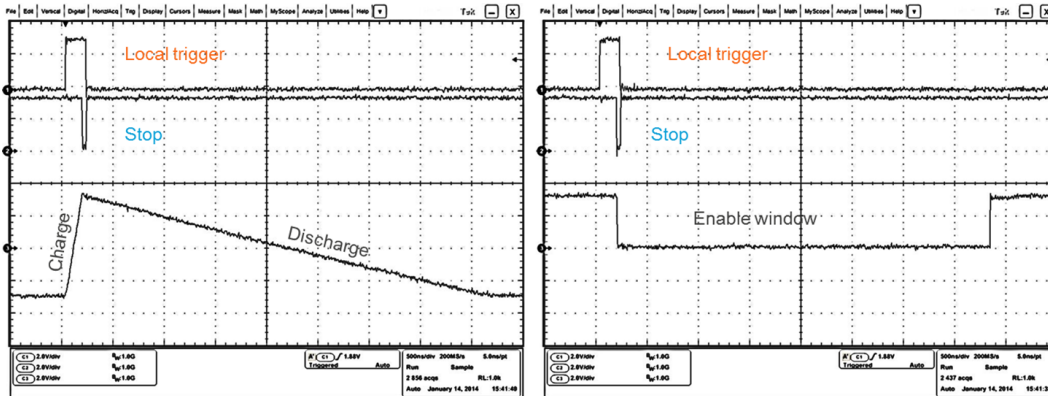


Figure 4.2: Example of the time expansion technique happening through the charge and the discharge of a capacitor (left) and the corresponding enable windows in which the measured time is converted to digital data in terms clock pulses counting.

When sizing this type of circuit, it would be desirable to use low capacitance values, because the steepness of the discharge slices through the threshold. This event determines the closing of the enable window and its jitter is reduced in this case. The small jitter of the enable signal, correspond to a small error in the counts. But small values of capacitance, as seen from figure 4.3, involve in non-linear trend, in dependence of the delay introduced in the line between the production of the local trigger and the stop signal. We made different tests and we decided to use a 100 pF capacitor. The measured RMS was 1.8 counts, that allows for a sub-ns time resolution.

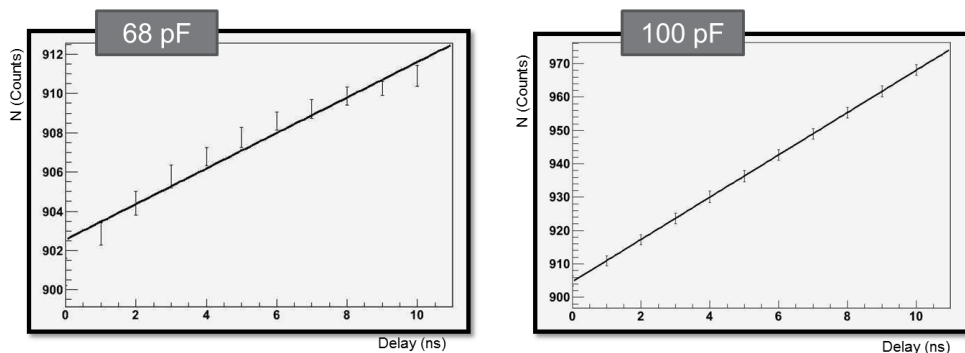


Figure 4.3: Plot of the experimental data of the sizing of the time expansion circuit. The value of the capacitance must be chosen in order to have a TDC linear response.

Moreover the system has been equipped with two programmable potentiometers, which allow to adjust the hold time and the timeout, and both potentiometers have been characterized. The hold signal is produced after at least one SiPM's signal exceeds the threshold (fast-OR signal); the hold potentiometer allows to set the delay between the fast-OR and the production of the hold signals. With the production of the hold signal, the amplitude of the SiPM's signal is recorded. The timeout potentiometer sets the time window in which the board waits to receive a trigger signal from the master board; if the timeout occurs, the charge stored in the capacitor and the hold signal are suddenly reset.

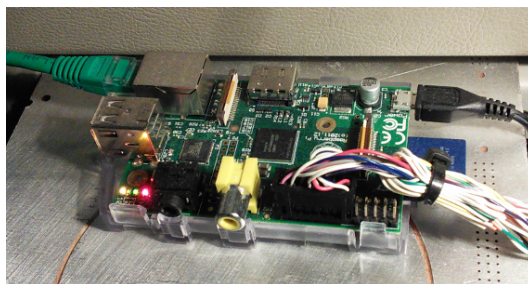
4.1.2 The Master Board-RPi Direct Link

The last upgrade regarding the electronics, concerns the substitution of the USB board, based on a PIC chip, installed on the master board and whereby the computer communicates with the master board. This PIC board allows serial protocol at 1.5 Mbps. Since one of the most interesting features of the RPi is an on board general purpose input output (GPIO) unit, we decided to implement a protocol that allows for the direct link with the master board (fig. 4.4). We obtained a link speed of 20 Mbps, which is equivalent to a serial communication at 20 MHz, the maximum frequency supported by the RPi.

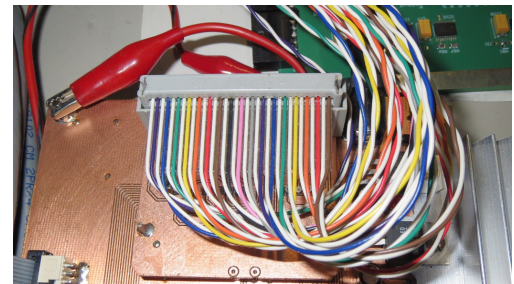
The protocol works in a way that

- the data acquisition starts when the RPi set in RUN mode the slave boards
- when a trigger occurs, the RPi stops the acquisition and sets the slave boards in DIAG mode
- the events are managed at low level by the RPi as hardware interrupts
- the RPi receives 32 bit packet from the master board FIFO, sending 32 clock pulses per time up to the FIFO is empty
- a handshaking procedure is ran at the end of every communication

and it is written in c language, using GPIO native libraries. Another important feature used during data acquisition, is the possibility to set the number of events which must be collected before being stored. In this way, since the RPi isn't a real time processing device, the software stores the data acquired from the master board inside the RAM; when the acquisition stops, the program runs a separated thread that writes the data in the USB hard disk drive. In the same time program can restart the acquisition and the dead time, of several ms, due to the drive access is mediated by the processor tasks management.



(a)



(b)

Figure 4.4: The Raspberry Pi (a) wired in direct link to the master board (b).

4.2 MEASURE OF THE TIME OF FLIGHT

4.2.1 The TOF model

Without loss of generality, we consider a simplified scheme involving only two slave boards, one for each plane we consider. After a muon hits a plane and the light propagates

through the fiber, the involved slave board a fast-OR. In the same time, say $t_{\text{start}}^{(A)}$ an on board capacitor start charging and the muon continue its path. A second fast-OR will be produced by a second board after the muon passed about 1 meter (or half a meter if one takes into account the middle plane) through the detector, the light travels to SiPMs in to inner fibers and the electronic signal generates it. So the time in which the second fast-OR will be produce is

$$t_{\text{start}}^{(B)} = t_{\text{start}}^{(A)} + t_p \quad (4.1)$$

where t_p takes into account the whole propagation history of the muon until it's detected. At this time, a second capacitor starts charging.

When a certain trigger logic is satisfied, the master board produces a trigger at the time t_{stop} . Now starts the discharge of all capacitors, through a circuit different from the charge one, such that the respective time constants results $\tau_{\text{discharge}} > \tau_{\text{charge}}$. For the i -th slave board it results $t_{\text{exp}}^{(i)} = (t_{\text{stop}} - t_{\text{start}}^{(i)}) \times E_i$, where E_i is the expansion coefficient of the i -th board.

By simple calculation and taking into account the relation 4.1, the difference in time Δt_{exp} between the two hits is

$$t_{\text{exp}}^{(A)} - t_{\text{exp}}^{(B)} = (t_{\text{stop}} - t_{\text{start}}^{(B)}) \times (E_A - E_B) + t_p \times E_A \quad (4.2)$$

when a muon passes through first plane A , *i.e.* comprising board A , and then through plane B . On the other hand, for every symmetric event, moving the same direction and passing through plane B then through A , one has

$$t_{\text{exp}}^{(B)} - t_{\text{exp}}^{(A)} = (t_{\text{stop}} - t_{\text{start}}^{(A)}) \times (E_B - E_A) + t_p \times E_B \quad (4.3)$$

where, in first approximation, the first term in the second member of the two expressions differs for a minus sign.²

The problem is to distinguish muons coming from different point but lying on the same track. This simple model gives us the capability to discriminate between tracks reconstructing trajectories of the cosmic rays coming from the sky and albedo muons traveling along the same direction but having opposite momenta. Focusing on the case in which the muons have horizontal trajectory and on the one in which their trajectory have the maximum slope allowed by the detector, we can hypothesize how the time distribution shape could be.

In the case of horizontal tracks, as shown in figure 4.5 (a), when the board A is triggered, it plays the role of the start or of the wake depending where the muon come from. In terms of counts, each situation will present its own time distribution (fig. 4.6 a) centered on a time value that is greater in case of the board A acts as start. Similarly, the board B will present the same behavior but in opposition (fig. 4.6 b), since it will be the wake for A acting as start. The propagation time t_p is assumed to be the same in both situations, and this justify our previous assertion.

For transverse tracks (fig. 4.5 b), can happen that in both situation the board A is the start and B the wake. This is due to the time taken by light to travel about 1 meter of fiber, in which its speed is considered to be about half of the speed of the light c . So, also in this

² Note that, for simplicity, we used same names in both expressions 4.2 and 4.3, but we can't compare them. To avoid this mistake we may add some apex and capitalize some letter, as we do in the following.

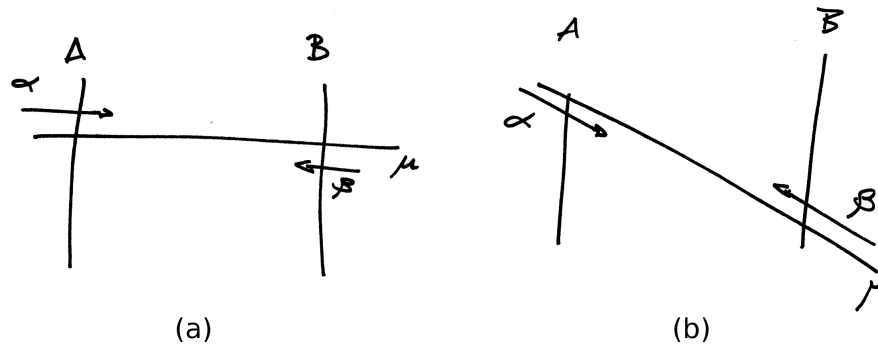


Figure 4.5: Example of the trajectories and directions of the muons crossing a 2 planes detector.

case, the counts distribution of the board A will present two separated peaks with one advance in respect to the other. Since B act always as wake, its counts measure the time offset between the wake signal and the trigger one sent by the master board, it expected to have only one large peak.

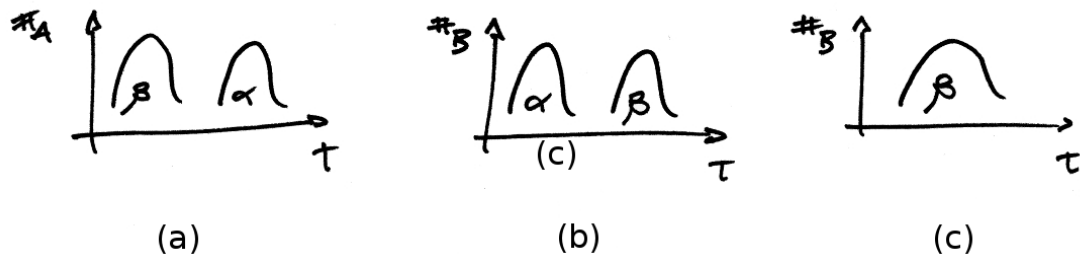


Figure 4.6: Expected distributions for the plane A (a) and for the plane B for horizontal (b) and transverse (c) tracks. .

The expected time distributions, for what concerns our model, are shown in figure 4.6, respectively for bi-peaked situations and single peak time distribution related to wake boards in high angle trajectories.

Finally, we can fix a TOF model for the MU-RAY telescope, and in my opinion, that can be applied to all detectors similar to it. Since the $t_{start}^{(A)}$ is the real origin of our event time scale, we can put it to zero, so the relation 4.1 becomes $t_{start}^{(B)} = t_p$ and the relation 4.2 becomes

$$t_{exp}^{(A)} - t_{exp}^{(B)} = (t_{stop} - t_{flight}) \times (E_A - E_B) + t_{hold} \times E_A \tag{4.4}$$

where we have changed $t_{start}^{(B)}$ with t_{flight} without any loss of generality. Moreover, since t_{flight} will depend on the position in (x, y) coordinate where the muon strikes the plane B, we can fix two indexes and consider t_{flight}^{ij} instead of t_{flight} , for i and j from 0 to the total number of clusters N .

In this picture, it results $t_{\text{flight}}^{ij} = t_m^{ij} + t_l \times \tau^{ij} + t_d$, where t_m^{ij} is the muons' time of flight inside the detector and it can be consider more or less constant over all the range of angles of incidence and where t_d is the electronic delay that, for now, we assume it as constant. Moreover, while the time $t_l \cong 1.7/c \times 1\text{m}$ represents the time required to pass 1m inside the fiber, in which the speed of light is about $c/1.7$, the τ^{ij} are the coefficients associated to the net path³ of the light inside the fibers and they have values in the range $[0, 1]$.

Stated to that and taking into account relation 4.4, one has

$$t_{\text{exp}}^{(A)} - t_{\text{exp}}^{(B)} = t_{\text{flight}} \times E_B - t_{\text{stop}} \times (E_A - E_B) \quad (4.5)$$

and if we impose the expansion coefficients be the same, it reduces to the relation

$$t_{\text{exp}}^{(A)} - t_{\text{exp}}^{(B)} = t_{\text{flight}} \times E_B. \quad (4.6)$$

4.2.2 A simple toy Monte Carlo for the TOF model

In order to validate this model, we wrote a toy Monte Carlo in c++ language that uses root libraries. The program simulate the flux of muons, with PDF plotted in 1.7, crossing a two plane 1 m² area detector. Each plane has X-Y view, so that a trigger of 4 plane must be intended as the condition in which a muon pass through both planes of the detector and all views enter in the trigger logic. Differently, we say that a 2 planes trigger occurs, when only the both X, or eventually Y, views of the two detector's planes participate in the trigger logic.

The coordinates of a point on the plane A are generated at random. From this point, the program propagates a muon moving at zenith angle, generated by meaning of the muon flux PDF, and at azimuthal angle, generated at random, checking if the ray intercepts the plane B. The generated events has been 10⁹ and the produced flux within the acceptance of the toy detector is plotted in figure 4.8.

```

xp_gen = gen->Rndm()* 1.0725;
yp_gen = gen->Rndm()* 1.0725;
xp = gen->Gaus(xp_gen,res);
yp = gen->Gaus(yp_gen,res);

thetaGen = pdfT->GetRandom();
histoTheta->Fill(thetaGen);
phiGen = gen->Rndm()*dupepi;
histoPhi->Fill(phiGen);

rho = dz/sin(thetaGen)/sin(phiGen);
xhit_gen = xp+rho*sin(thetaGen)*cos(phiGen);
yhit_gen = yp+rho*cos(thetaGen);
xhit = gen->Gaus(xhit_gen,res);
yhit = gen->Gaus(yhit_gen,res);

if((xhit<= pos_max) && (yhit<= pos_max)
    && (xhit>= pos_min) && (yhit>= pos_min)){
    ...
    histoPhiReco->Fill(phi);
    histoThetaReco->Fill(theta);
}

```

³ Muons having the same angle of incidence, imply that the produced light have the same net path. The two boundaries are related respectively to horizontal tracks and 45 deg tracks.

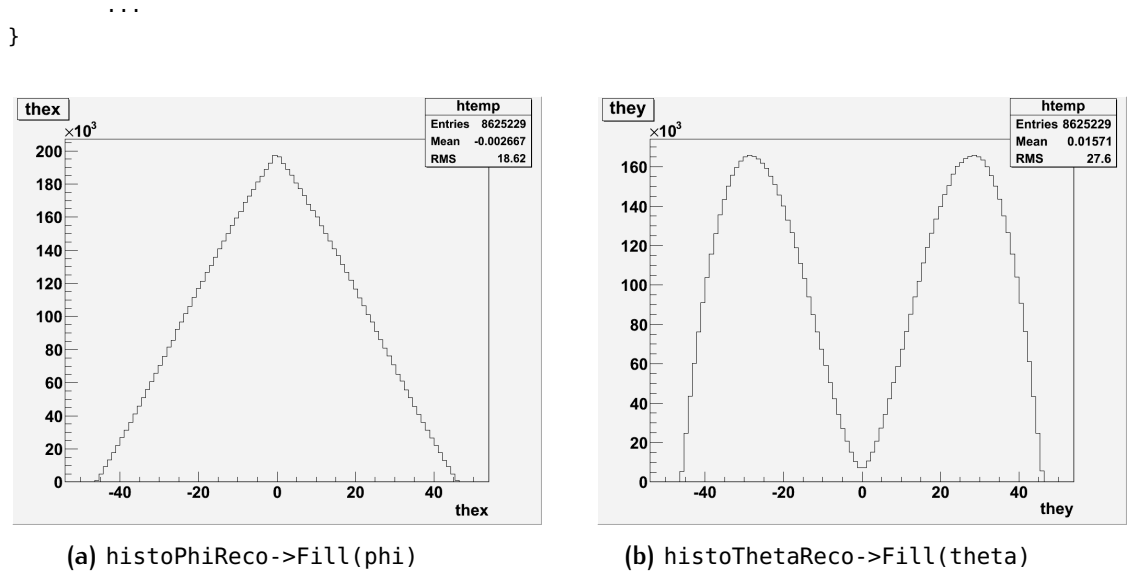


Figure 4.7: Histograms of events with respect of azimuth (a) and zenith (b) angles.

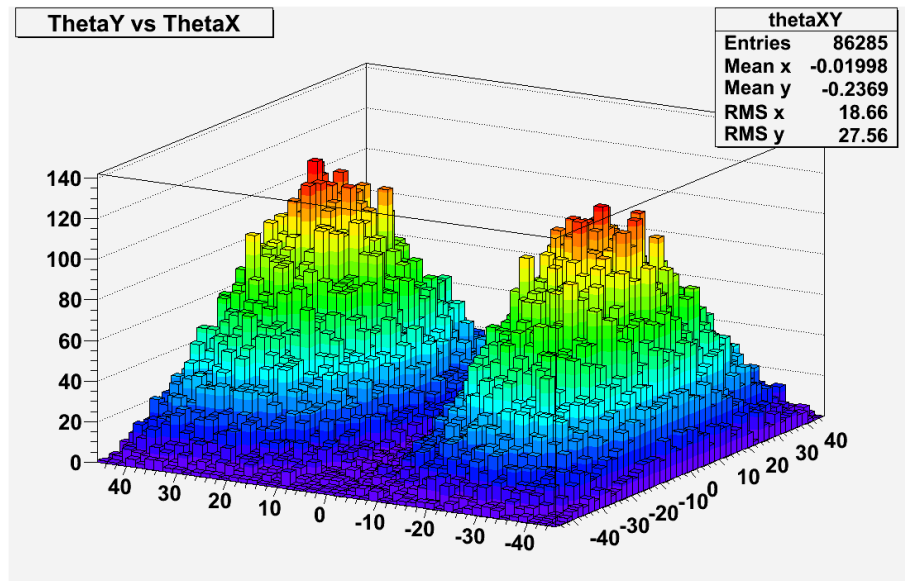


Figure 4.8: Histogram of the number of events recorded in each bin, obtained combining the azimuth and theta distribution reported in figure 4.7.

In correspondence of a ray within the acceptance of the detector, are simulated four light signals propagating, from the generated points, inside the fibers. The calculated time values are spread with respect to the light propagation uncertainty, amounting to 700 ps and the direction, first A then B or vice versa, is assigned at random. Once generated, any information about the direction is lost.

```

tXtop_gen = getTime(yp);
tYtop_gen = getTime(xp);
tXdw_gen = getTime(yhit);
tYdw_gen = getTime(xhit);
tXtop = gen->Gaus(tXtop_gen,resScintFibra);
tYtop = gen->Gaus(tYtop_gen,resScintFibra);
tXdw = gen->Gaus(tXdw_gen,resScintFibra);

```

Figure	Peak Identifier	Counts Mean Value	σ
fig. 4.10 (a)	A1	400.2	3.13
	A2	417.2	5.71
fig. 4.10 (b)	B1	400.2	3.10
	B2	417.2	5.42

Table 4.1

```

tYdw = gen->Gaus(tYdw_gen, resScintFibra);

//Mu Back-Forw o Forw-Back
double tof = rho/vlux;
bool FBorBF = (gen->Rndm())<0.5? true: false; //true TOP->DW

if(FBorBF){
    tXdw += tof;
    tYdw += tof;
    albedo = 0;
}
else{
    tXtop += tof;
    tYtop += tof;
    albedo = 1;
}

```

We simulated both trigger logic and respective time values has been spread for a TDC resolution of 600 ps. By mean of the time expansion method, we calculate ADC counts simulating the number of clock cycles until the capacitors discharge is finished for each board.

We expect that the overall counts distribution for each slave board is different in the two trigger logic. The problem related to the 4 plane approach is that parallel rays in the acceptance of the detector lead to different trigger instances, while in the 2 plane trigger logic they imply only one possible instance. This effect can be verified in figure 4.9.

By making angular cuts that represent the limit situations illustrated in figure 4.5, we find the predicted distributions. In figure 4.10 are reported the counts distribution, in the case of the 2 planes trigger logic, for muons traveling at zenith angle $-1^\circ < \theta < 1^\circ$ and azimuth $-1^\circ < \varphi < 1^\circ$. We have done four gaussian fits, one per peak, with the software ROOT. From the data reported in table 4.1, we found a good agreement with the expected value $TOF_{exp} = \pm \frac{1.03 \text{ m}}{c} = 3.43 \text{ ns}$, being the plane-to-plane distance used in the simulation equal to 1.03 m.

Using the equation 4.6, we have $TOF = \pm \frac{(417.2-400.2) \times 4 \text{ ns}}{20} = \pm 3.4 \text{ ns}$, with the minus sign for events propagating from B to A.

Similarly, in order to have the situation illustrated in figure 4.5 (b), we made angular cuts $42^\circ < \theta < 44^\circ$ and azimuth $-1^\circ < \varphi < 1^\circ$, obtaining the distributions shown in figure 4.12. Another time, the distributions shapes our as expected from our model and the values calculated with Gaussian fit are reported in table 4.2.

Thus we have $TOF_{forward} = \frac{(455.4-400.2) \times 4 \text{ ns}}{20} = 11.04 \text{ ns}$ for muons coming at these angles and $TOF_{backward} = \frac{(408.6-400.2) \times 4 \text{ ns}}{20} = 1.68 \text{ ns}$ for albedo muons. By meaning of t_{flight}^{ij} these values must be adjusted for the time took by light inside the fiber, where the net path is 0.96 m. Thus, $T_l = 6.4 \text{ ns}$ and the times of flight of the muon in the two cases are respectively $T_{muon} = TOF_{forward} - 6.4 \text{ ns} = 4.64 \text{ ns}$ and

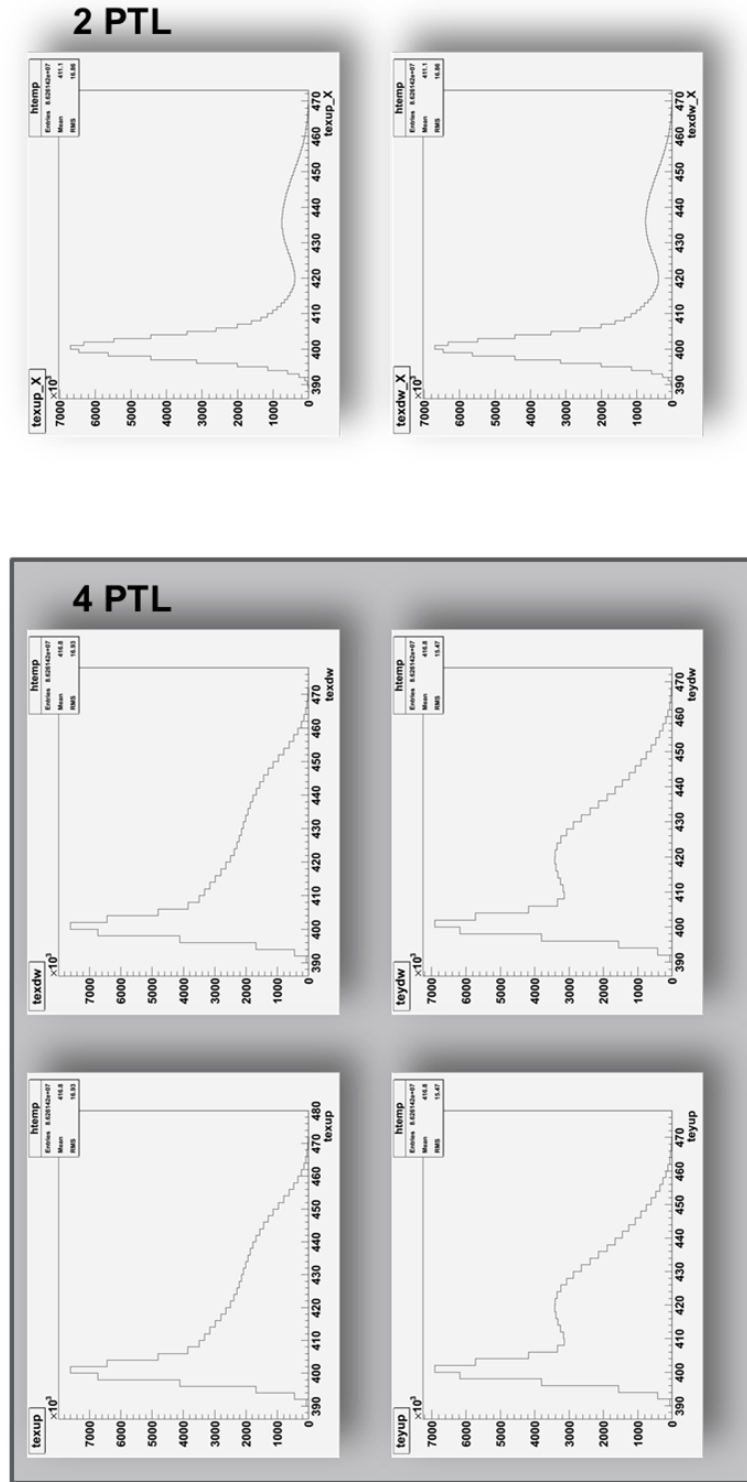


Figure 4-9: Comparison between counts distributions in 4 planes trigger logic (4PTL) and 2 planes trigger logic (2PTL). Due to the variability of the trigger board and unlike 2PLT distributions, 4PTL distributions don't show net trends.

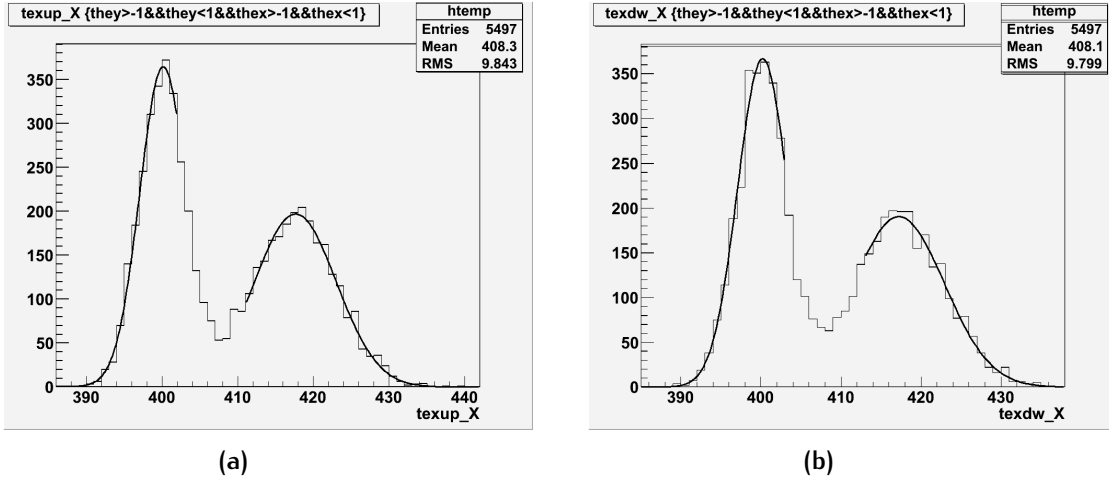


Figure 4.10: Reconstructed counts distributions for the plane A (a) and the plane B (b) in a 2 planes trigger logic for horizontal tracks.

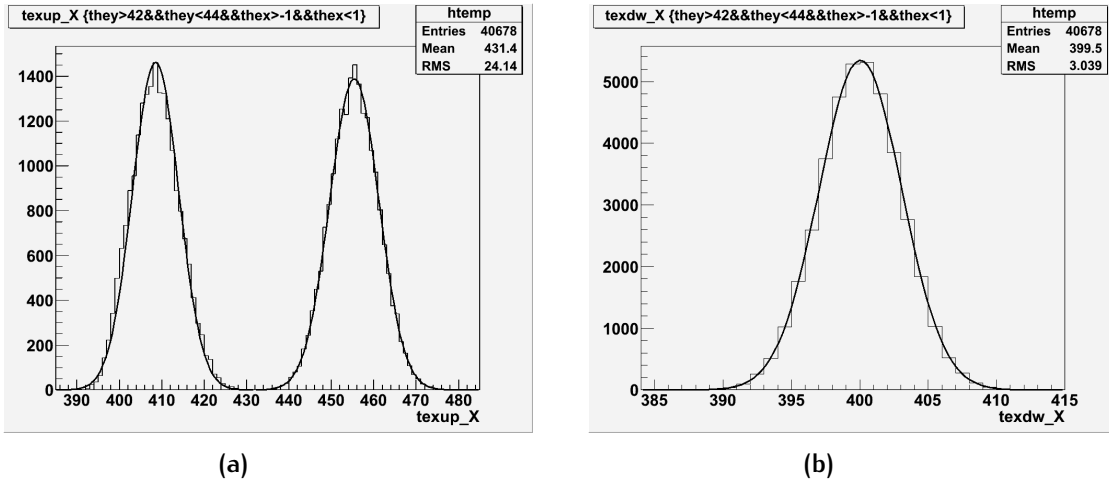


Figure 4.11: Reconstructed counts distributions for the plane A (a) and the plane B (b) in a 2 planes trigger logic for transverse tracks.

$T_{\text{albedo}} = \text{TOF}_{\text{backward}} - 6.4 \text{ ns} = -4.72 \text{ ns}$ that are in good agreement with $\text{TOF}_{\text{exp}} = \pm \frac{1.41 \text{ m}}{c} = 4.7 \text{ ns}$.

The same analysis has been also done for the 4 planes trigger logic and, except for the values of the TOF calculated for horizontal muons, they differ from the expected one more than 2 ns. Moreover looking at distributions (fig.), It could be sometimes difficult the check their Gaussianity and proper values should be estimated in different way. The 4 plane configuration can furnish a statistical estimation of the muon's TOF when the flux is unidirectional or when, in the case of bidirectional flux, is recorded the last board that precedes the generation of the trigger, making possible the kinematic reconstruction of all events which entered in the trigger logic.

Finally, we have to point out, that the simulated detector represents a rough approximation of the Mu-Ray detector, but the proposed model could be useful to do some hypotheses analyzing the data taken during measure campaigns.

Figure	Peak Identifier	Counts Mean Value	σ
fig. 4.12 (a)	A1	408.6	5.46
	A2	455.4	5.81
fig. 4.12 (b)	B	400.2	3.03

Table 4.2

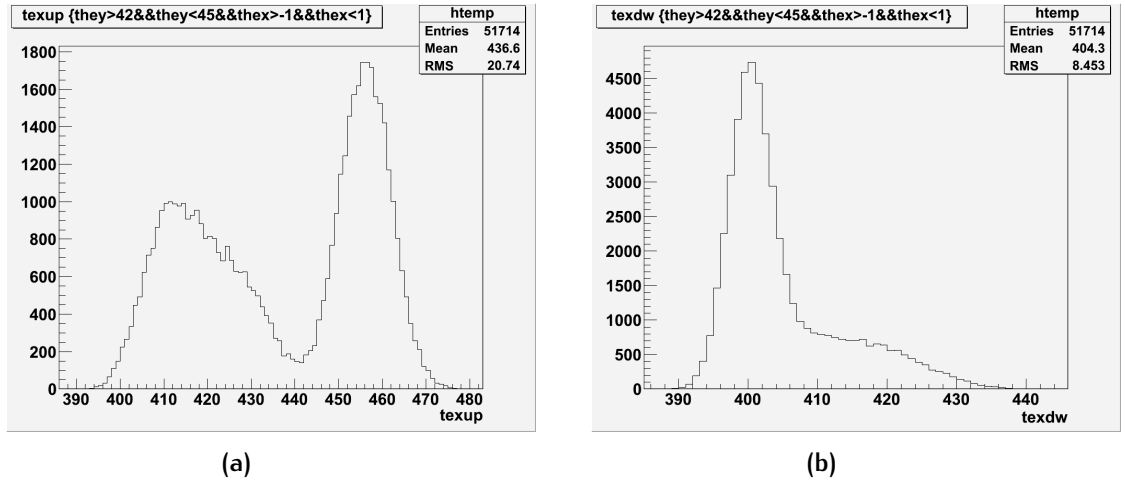


Figure 4.12: Reconstructed counts distributions for the plane A (a) and the plane B (b) in a 4 planes trigger logic for transverse tracks.

4.3 PELTIER CELLS TEMPERATURE CONTROL SYSTEM

The latest improvement in the pipeline is the development of a thermal control system with a very low power consumption. We choose to develop a prototype that use Peltier cells and study the best equipment to be supplied to it.

The Peltier cells are semiconductor devices based on the Peltier effect that works as a heat pump. Known since 1864, the Peltier effect states that an electric current flowing through a junction of heterogeneous conductors, produces an absorption of heat by the same, at the expense of the materials in contact. The effect is the converse of the Seebeck effect that expects an electric current flow inside the junction, when this is heated.

A Peltier cell (fig. 4.13) absorbs at the cool side an amount of heat that is given by

$$Q_c = \alpha I T_c - \left[\frac{1}{2} I^2 R + \kappa (T_h - T_c) \right] \quad (4.7)$$

where I is the current that flows inside the device, R is the resistance of the same, κ is the Boltzmann constant, T_h and T_c are respectively the temperatures of the hot and of the cool side [Richmond 1966]. The coefficient $\alpha = \frac{\Delta V}{\Delta T}$ is the thermoelectric power. The two terms in square brackets are the heat produced for Joule effect at the cold junctions and the heat conduced back to the cool side (Furier Effect), respectively. Their contributions must be as small as possible, in order to maximize the heat absorption at cool side.

In the first tests we used small Peltier cells of area $9 \times 9 \text{ mm}^2$ and 2.9 W maximum power consumption. The tests concerned the study of the Peltier cells without cooling and sandwiched between a couple of insulators. The insulators were laid on the ceramic plates of the device, being careful to not create a thermal short circuit, closing it completely between them. The results are reported in tables 4.3, where in both cases the ΔT values

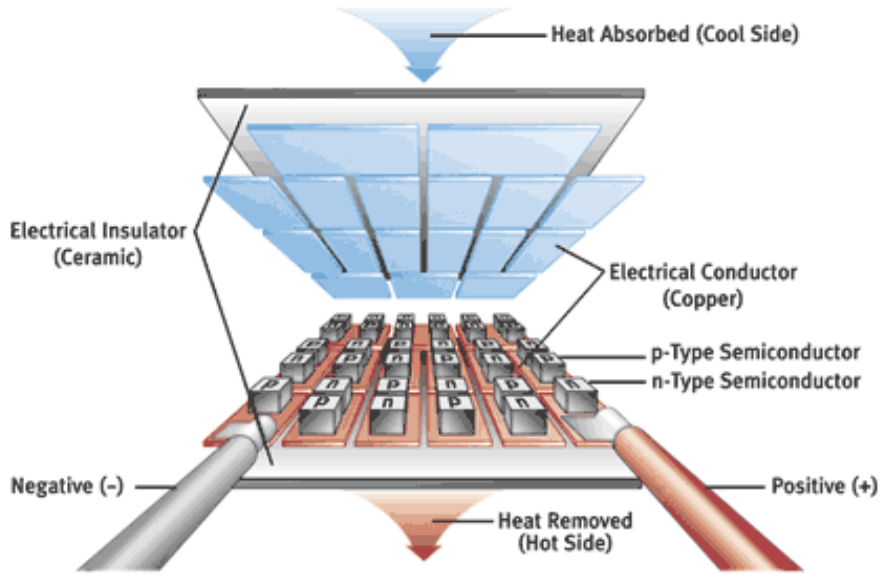


Figure 4.13: Illustration of the internal structure of a peltier. An electron, during the passage through a *p*-type semiconductor under the effect of the applied electrical field, loses part of its kinetic energy; a certain amount of energy is recovered inside the *p*-metal junction, in the form of heat absorbed by the electron. Here, the electron has enough energy to continue its movement inside the *n*-type semiconductor. It issues the excess of energy by heating the *n*-metal junction.

I [A]	T _h [°C]	T _c [°C]	ΔT [°C]	ΔV [V]
0.001	24.9	24.8	0.1	0.000
0.092	26.2	23.3	2.9	0.100
0.183	28.2	22.3	5.9	0.200
0.269	32.8	23.5	9.3	0.300
0.343	37.8	25.6	12.2	0.400
0.432	40.5	26.0	14.5	0.500

I [A]	T _h [°C]	T _c [°C]	ΔT [°C]	ΔV [V]
0.001	24.9	24.9	0.0	0.000
0.092	26.8	24.3	2.5	0.100
0.178	28.2	23.9	4.3	0.200
0.262	32.2	25.3	6.9	0.300
0.328	36.5	29.6	6.9	0.400
0.410	39.3	31.3	8.0	0.500

Table 4.3

increase with the temperature of the hot side, while the temperature of the cold side first decreases and then increases. This reversal is due to the fact that the cell tries to absorb more and more heat from the insulator, increasing the power with which it operates. This causes the increase of the heat injected into the entire device due to Joule and Fourier effects. Both test ended with the breakup of the cell.

In the second test, we used two Peltier cells, arranged on a 8 mm thick copper bar as in figure 4.14 (a). The Peltier cells were placed at 1/4 and 3/4 of the bar’s length (18.5 cm), and we measured the temperature in the central point of the lower side of the bar. The hot sides of the Peltier cells were coupled with a big aluminum heat sinks and only the lower part of the bar was insulated. We decided to study this arrangement after a test made on the hybrid, in which we disposed the Peltier cells in the same configuration but on the thermal plate of the hybrid and the temperature sensor for the measurement on the central point of the side of the SiPMs housing. We hadn’t measured any variation of the temperature in a wide range of power consumes and we attributed this to the small thickness of the copper that constitutes the thermal plate. Thus, by increasing the section of the copper, we expected an increase in transverse heat conduction. The data of the

I [A]	T _{env} [°C]	T _c [°C]	ΔT _{env} [°C]	ΔV [V]
0.001	25.6	25.7	-0.1	0.000
0.098	25.6	24.9	0.7	0.100
0.195	25.5	24.2	1.3	0.200
0.295	25.4	23.8	1.6	0.300
0.396	25.3	22.8	2.5	0.400
0.497	25.2	22.1	3.1	0.500
0.598	25.0	21.7	3.3	0.600
0.699	24.8	21.2	3.6	0.700
0.799	24.7	20.8	3.9	0.800
0.896	24.6	20.5	4.1	0.900
0.991	24.5	20.2	4.3	1.000
1.083	24.5	19.9	4.6	1.100
1.172	24.5	19.9	4.6	1.200
1.258	24.5	19.9	4.6	1.300
1.342	24.5	20.0	4.5	1.400
1.420	24.5	20.1	4.4	1.500

Table 4.4

second test are reported in table 4.4 and they confirmed the expected increase in heat conduction due to the presence of the copper bar.

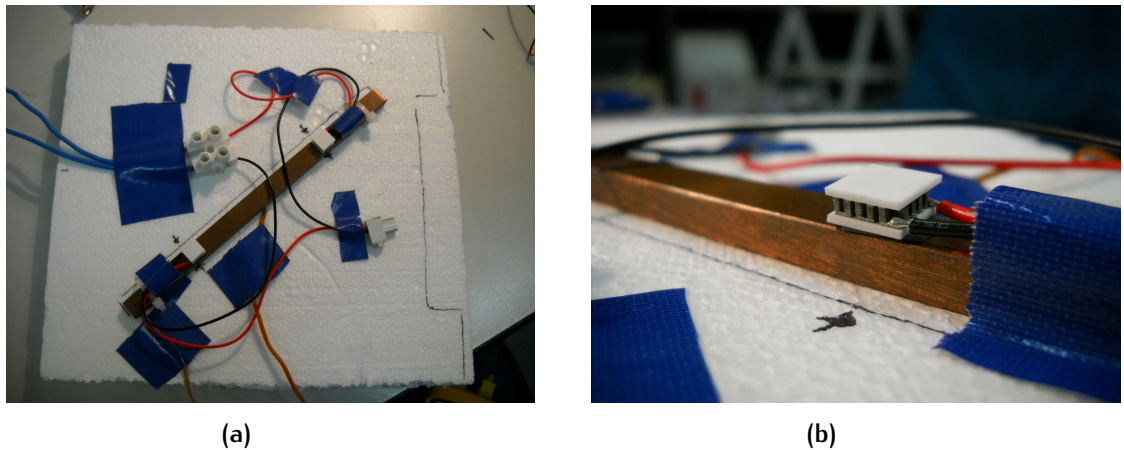


Figure 4.14: Experimental setup used for the measure of the temperature on the lower side of the copper bar during the second test.

The third test was made to prove temperature uniformity of the SiPMs housing. We also tried to improve the heat extraction by setting up a dummy mask made of polystyrene, cut so as to contain the copper bar and the part of the hybrid which must be isolated, and using an additional Peltier cell, with respect to the previous test, placed at 1/2 of the bar length. Five temperature sensors were placed as in figure 4.15 on the SiPMs housing side of the hybrid. We measure an agreement, within 0.2°C , of the temperature values recorded by sensor for increasing power up to $\Delta T_{\text{env}} \approx 5^{\circ}\text{C}$.

We have done the same tests using a copper bar with an height of 0.2 mm, but obtaining worse results compared to the 0.8 mm thick bar. Moreover, we have conducted other tests to choose best coupling materials, according to which we decided to use thermally conductive gum and graphite sheets, and to try active cooling instead of the passive one in order to pull out efficiently the heat from the hot side. Since active cooling imply more power consumption, where our target is 2 W per hybrid, we chose aluminum heat sink for

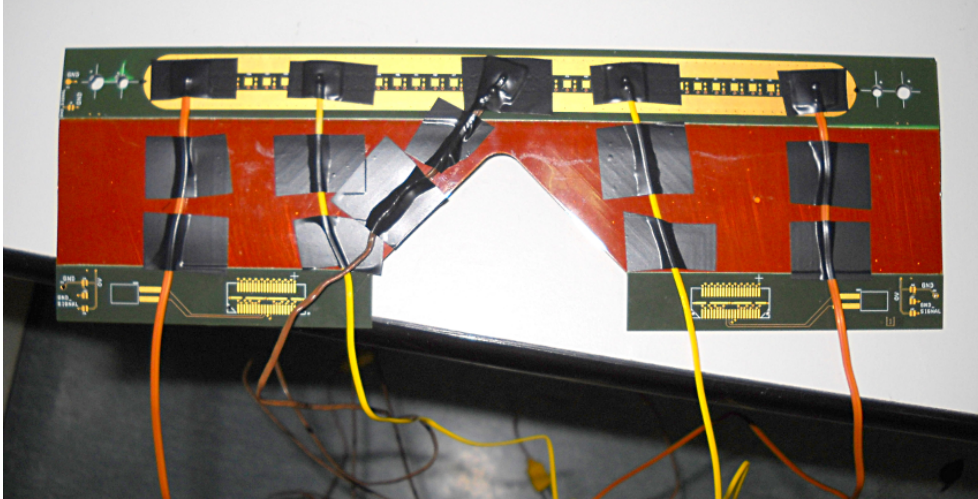


Figure 4.15: Arrangement of the temperature sensors on the SiPM housing pad. We measured the uniformity of the temperature in 5 different points.

natural convection⁴, suitable for low air speed environments and with thermal resistance $< 1^{\circ}\text{C}/\text{W}$.

In the final version of the temperature control system we substituted the set of Peltier cells used during tests with only one bigger ($30 \times 15 \text{ mm}^2$) Peltier cell (fig. 4.16) that has the same max power consumption of the series but a better coefficient of performance (COP), greater than 1. The COP of a Peltier cell can be estimated by graphic method and in the case of the series of the three cells, used during first tests, we calculated a $\text{COP} \approx 1$.

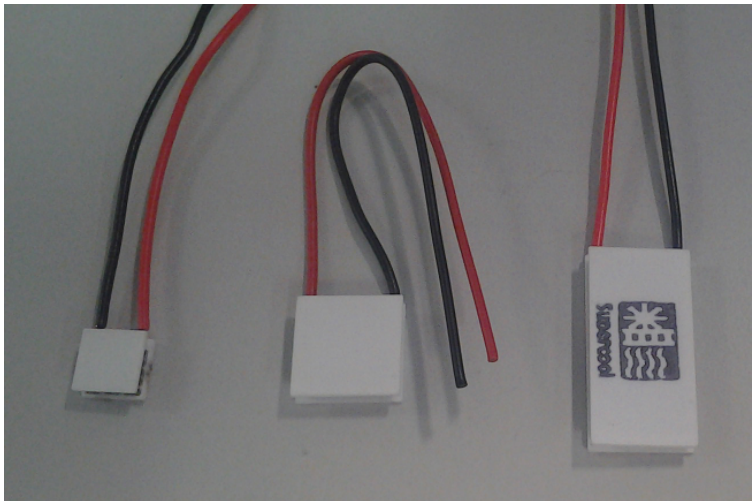


Figure 4.16: Different models of Peltier cells. During the early tests we use the smaller one (on the left), while for the development of the temperature control system we use the rectangular cell (on the right).

Finally, a mask has been made with a 3D printer and its interior features a honeycomb structure in order to isolate, by air cells, the parts arranged in its compartments. The assembly hosted by the mask, from the heat sink to the thermal plate of the hybrid, is composed by

⁴ <http://www.coolinnovations.com/products/heatsinks/natural-convections/>

- a reverse aztec pyramid shaped copper piece, whose top is in direct contact with the base of the heat sink
- a pad of thermally conductive gum coupling the edge of the copper piece with the hot side of the Peltier cell
- a Peltier cell
- a sheet of graphite
- a $8(h) \times 185(l) \times 15(w)$ mm³ copper bar
- a pad of thermally conductive gum coupling the copper bar with the thermal plate of the hybrid

where the role of the thermally conductive gum and graphite sheets is to enhance, respectively, the coupling between surfaces in contact and the heat transport along the bar.

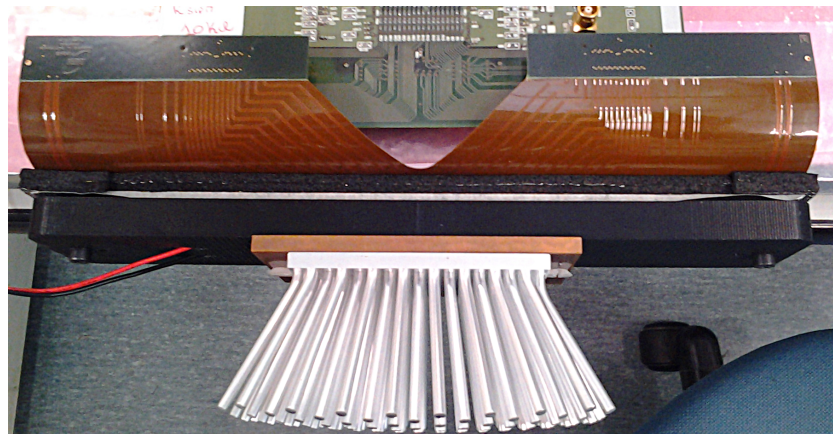


Figure 4.17: The temperature control system mounted on the dummy module.

With this system, attached to an aluminum dummy module (fig. 4.17), we obtain a ΔT_{env} of about 8°C , that, given the presence of the small thermal resistance dummy module, represents the worst case with a power consumption of about 2 W (fig 4.18). Since a module offers an higher thermal resistance, because of the presence of plastic and air, we we believe that this result can be improved without increasing power consumption. The total power consumption due to twelve temperature control systems will be $< 30\text{ W}$. This upper value, added to the other consumption, makes possible the use of solar panels.

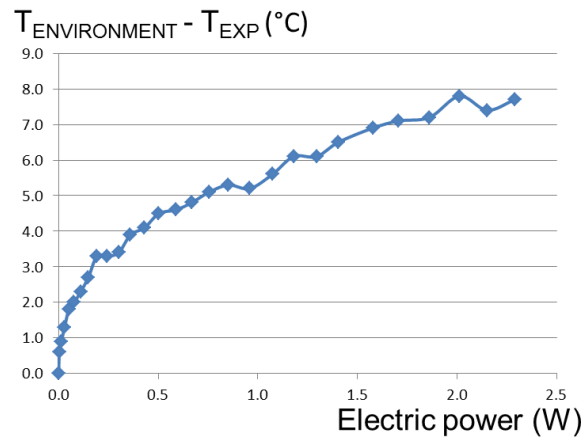


Figure 4.18: Chart of the ΔT_{env} in function of the electric power showing the good performance of the temperature control system.

CONCLUSIONS

We have shown how cosmic ray muons can be used to make the radiography of a large geological edifice, like a volcano. Muons have a wide energy spectrum and using those muons having enough energy to pass through the volcano, we are able to reconstruct its the density map. With the muon radiography technique we measure the absorption of the muons flux through a given target. During years many trials and experiment have developed both the technique and the detectors to implement the muography. The modeling of the muons flux and the study of the phenomenology connected to the cosmic ray muons, have helped us to understand the feasibility and the limits of this technique. Nevertheless, thanks to these models we can analyze the data and make appropriate assumptions to better understand its capabilities.

Since year 2000 the methodology was used with success by japanese researchers. During years many results have been achieved, from the feasibility of this methodology to the possibility to obtain, within a short time, the variations of the density of the volcano to act promptly in case of pre-eruptive activities [Tanaka 2014]. In 2007, Tanaka reported about appreciable post-eruptive changes in the upper part of Mt. Asama after an eruption occurred in 2004 [Tanaka 2007b]. Also The DIAPHANE and TOMUVOL collaboration applied with success the methodology to other volcano. We must mention the discovery of an high density region in the upper part of the Puy de Dôme made by the TOMUVOL collaboration.

The employment of different detectors in different situations has allowed to understand and trace the line to build detectors suitable for this kind of application. The advent of new technologies and the better understanding of the nature of the background noise, led to development of rugged muon trackers capable of high angular resolution and high background rejection. When one deals with the radiography of geological object, have to employ detector capable of operating in outdoor environments. The strength and portability of the equipments are strictly required. The muons flux of few Hz imply the need to build large area detectors, up to few tens of m^2 , in order to improve the statistics. The capability to assemble large sensitive surfaces is also required.

Actually the detectors used in muon radiography are designed in order to use the technical know-how that comes from major experiments like OPERA, ATLAS and other. They fulfill part of the requirements needed by muon radiography. In particular, only the DIAPHANE detectors can in principle take advantage of the time of flight measurement to have a better background rejection. Summarizing, the characteristics of the detectors currently in use, are

- **Japanese collaborations** : 2 plane, 50 channels (scintillator bars, PMT)
- **DIAPHANE** : 3 planes, 96 channel, TOF capability (scintillator bars with WLS fibers inside, multianode PMT)
- **TOMUVOL** : 4 planes, 10000 channels (GRPC Calice)

- **Mu-Ray** : 3 planes, 384 channels, TOF (triangular shaped scintillator bars with WLS fibers inside, SiPM)

Different from other, the Mu-Ray detector is a brand-new detector. It satisfies all the requirements for the muon radiography. Moreover it is equipped with a sophisticated automatic system which makes it able to work in almost total autonomy. It should take into account that a machine could work without human intervention, each time the site of interest is far away from the lab. In this context, it is desirable to devote more resources and expertises to the development of intelligent systems.

The Mu-Ray detector has been designed to ensure the best performance and to lend to any purpose other than volcanological, requiring high spatial/angular resolution, high resolving time, high resolution time of flight measurements, use in extreme environment.

During the construction, has been developed all the procedure, tools and facilities to grant the good manufacture of the detector. We spend many time to improve light collection, from the production of light inside the scintillator to its the detection by the SiPM. We glued the WLS fibers inside the co-extruded holes of the scintillator bars with an optical epoxy glue and realized the optical connector to place the fibers in front of the SiPM. All couplings have been studied and produced with the highest skill. All the parts of the basic module were subjected to meticulous quality check before being employed.

Once the planes of scintillators have been assembled, including electronic and chiller system, we characterize the detector in the search of the working point. During these laboratory tests, we started improving it by studying solutions to the problems we encountered. Thus we developed the automated remote system MuBot, prototyped the low power consumption temperature control system using the Peltier cells and designed the Arduino based local monitoring board.

In order to make better and better the performance of the detector, we have worked to upgrade many parts of the system. Changes included the replacement of the silicon photomultipliers, the realization of the Peltier cells based temperature control system for silicon photomultipliers, the replacement of the ASIC chips for the readout of the silicon photomultipliers, the improvement of the time expansion circuit for the measurement of the muon's time of flight, the development of a model of time of flight suitable for bidirectional flux when no information about the board that has triggered are available, the development of a low level protocol for the direct link between the master board and the Raspberry Pi computer.

We theorized a time of flight model to trace the direction of the muons that cross the detector. To prove its validity, we have run a toy Monte Carlo simulating $\sim 10^7$ bidirectional events inside the acceptance of the detector. Then, we reconstructed the statistical distributions of the expanded times, recorded in the coincidences of the 4 planes trigger logic and the 2 planes trigger logic. By making appropriate angular, we have measured the expected time of flight of the muons in the case of the 2 plane trigger logic, while for the 6 plane trigger logic this was not always possible. In this latter case the values didn't follow a Gaussian statistic and often it has been difficult to determine their mean values. By virtue of this, it is desirable the use of a trigger logic simplified if the

number of accidental coincidences can be reduced, for example, using SiPMs with a lower dark-rate.

The temperature control system has been realized after a series of tests designed to prove the uniformity in temperature of the hybrid, the quality of the thermal coupling and heat insulation of the mask, the ability of the Peltier cells to work with passive dissipation. Finally, during a worst-case test, we were able to have a stable temperature of the SiPM housings, $\sim 8^\circ\text{C}$ under the environmental temperature. We plan to improve this performance, going to ΔT_{env} below 10°C having the same power consumption.

In the 2013 we had two measurement campaigns. The first one at the Mt. Vesuvius (Napoli, Italy), which lasted one month, and the second longer at the Puy de Dôme (Clermont-Ferrand, France). During the Vesuvius campaign we tested the systems with which the detector is equipped and assessed the reliability during the data taking, in anticipation of the campaign in France. The measurement campaign at the Puy de Dôme has been more interesting because, on the one hand, has been conducted in a European collaboration between our group and the TOMUVOL collaboration, and on the other, thicknesses traversed by the muons in the volcano are comparable to those measured in the other experiments and therefore lend themselves to a direct comparison. Actually the data analysis is in progress and the first results are expected in the coming months.

Part III

APPENDIX

LISTINGS

We report the listings of the programs written to implement, in order, the remote automatic system MuBot, the toy Monte Carlo simulation to validate the TOF model and the new data acquisition software that uses the Raspberry Pi's GPIO.

1 MUDOG.PY

```
import sys
import os
import time
import serial
import subprocess
import pymysql
import datetime
import binascii
from math import log
from time import strptime, strftime
import threading
import psutil

print ('\n\nMuDog (MuBot ver 4.0) - MuRay Experiment')
print ('Copyright 2013(C) 19LC77 (email : luigi.cimmino@na.infn.it)')
print ('.....\n')

print ("* LOADING SYSTEM")

dbELMB = pymysql.connect(host='localhost', user='*****', passwd='*****', db='elmb_rd')

out_a = [b'\x00',b'\x00',b'\x00',b'\x00',b'\x00',b'\x00',b'\x00',b'\x00']
cont_a = 0

flag = 1

V_ref = 13.90 #Volt
R_ch_mean = 6.80 #kOhm

T_ext = '0.00'
H_ext = '0.00'
Hp = '0.00'

T_mean_st = 20
T_mean_new = 20
V35 = 38.500
V18 = 14.500

cont = 0
inp=''
out=''

serc = serial.Serial(
port='/dev/ttyTRS',
baudrate=9600,
parity='N',
stopbits=1,
bytesize=8
)
serA = serial.Serial(
port='/dev/tty35V',
baudrate=9600,
parity='N',
stopbits=2,
bytesize=8
)
serJ = serial.Serial(
port='/dev/ttyJul',
baudrate=38400,
parity='E',
stopbits=1,
bytesize=7,
```



```

out_sx = [0,0,0,0,0,0,0,0,0,0,0,0]
if (i == 24):
T_ch00 = round(3383.81-865.8*(15.274+0.00231*(1000-
(R_ch_mean/(V_ref/(round(out_dx[0]/(i-4),0)*3.3/4095)-1))*1000))*0.5, 1)
...
T_ch23 = round(3383.81-865.8*(15.274+0.00231*(1000-
(R_ch_mean/(V_ref/(round(out_sx[11]/(i-4),0)*3.3/4095)-1))*1000))*0.5, 1)

if (ID != ID_start - 5) :
time.sleep(10)

try :

serArdDx.write(bytes('S', 'UTF-8'))
for j in range(12) :
out_byte = str(serArdDx.readline())
outs = out_byte.strip("\b")
outs = outs[:-4]
out_dx[j] = out_dx[j] + int(outs)

j = 0
serArdSx.write(bytes('S', 'UTF-8'))
for j in range(12):
out_byte = str(serArdSx.readline())
outs = out_byte.strip("\b")
outs = outs[:-4]
out_sx[j] = out_sx[j] + int(outs)
except :
print('Skipping one row...')
OK = 1
if (OK == 0) :
i+=1
j = 0
outs=''

print ('\n-----\n')

print ('Measure #',ID,':')
print ('\t T_ch00 :\t' + str(T_ch00) + "\t°C")
...
print ('\t T_ch23 :\t' + str(T_ch23) + "\t°C")

T_ref = str(round((T_ch00+T_ch01+T_ch02+T_ch03+T_ch04+T_ch05+T_ch06+T_ch07+T_ch08+
T_ch09+T_ch10+T_ch11+T_ch12+T_ch13+T_ch14+T_ch15+T_ch16+T_ch17+T_ch18+T_ch19+
T_ch20+T_ch21+T_ch22+T_ch23)/24, 1))

print ('\n\n' + TimeS + ' @PuyDeDome')
print ('-----\n')

serc.close()
serc.open()
serc.isOpen()

time.sleep(1)
cont_a = 1

terms_flag = 1
while (serc.inWaiting() > 0):
out_a[0] = serc.read()
if out_a[0] == b'\x02':
while (serc.inWaiting() > 0 and cont_a < 7):
out_a[cont_a] = serc.read()
cont_a = cont_a + 1
T_ext = str(round((int(bytes.decode(binascii.hexlify(out_a[4])), 16)*256 +
int(bytes.decode(binascii.hexlify(out_a[5])), 16))/100 - 50, 2))
H_ext = str(round((int(bytes.decode(binascii.hexlify(out_a[2])), 16)*256 +
int(bytes.decode(binascii.hexlify(out_a[3])), 16))/100 + 0.2, 2))
a = 17.271
b = 237.7
Hp = str(round(b * ((a * float(T_ext))/(b + float(T_ext)) + log(float(H_ext)/100))/
(a - ((a * float(T_ext))/(b + float(T_ext)) + log(float(H_ext)/100))), 2))
if out_a[0] == b'\x02' and out_a[6] == b'\x03' :
break

print ('Room temperature : \t\t' + T_ext + "\t°C")

msg_j = 'in_pv_00'

for i in range (len(msg_j)) :
serJ.write(str.encode(msg_j[i]))
serJ.write(str.encode(chr(0x0D)))

time.sleep(1)
while serJ.inWaiting() > 0 :
out_byte = serJ.read()
if (bytes.decode(out_byte) != '\n' and bytes.decode(out_byte) != '\r') : out += bytes.decode(out_byte)
if (out != '') :
T_bath = out

```

```

print ('Bath temperature : \t\t' + T_bath + "'C")
out=''
else :
T_bath = '0.00'

msg_j = 'in_pv_01'

for i in range (len(msg_j)) :
serJ.write(str.encode(msg_j[i]))
serJ.write(str.encode(chr(0x0D)))

time.sleep(1)
while serJ.inWaiting() > 0 :
out_byte = serJ.read()
if (bytes.decode(out_byte) != '\n' and bytes.decode(out_byte) != '\r') : out += bytes.decode(out_byte)
if (out != '') :
P_bath = out
print ('[ ' + P_bath + '% of total power used by chiller ]')
out=''
else :
P_bath = '0'
print ("*** WARNING : Julabo is not responding!\n")

print ('Relative humidity : \t\t' + H_ext + '%')
print ('Dew Point : \t\t\t' + Hp + "'C\n")
serc.close()
serJ.close()

T_mean_new = round((int(bytes.decode(binascii.hexlify(out_a[4])), 16)+256 +
int(bytes.decode(binascii.hexlify(out_a[5])), 16))/100 - 50, 2)

if ((T_mean_new > T_mean_st + 0.5) or (T_mean_new < T_mean_st - 0.5)):
V35 = 38.500 + 0.07*(T_mean_new - 20)
T_mean_st = T_mean_new

#serA.open()
#
#inp1 = 'OUTP OFF'
#for i in range (len(inp1)) :
# serA.write(str.encode(inp1[i]))
#serA.write(str.encode('\n'))
#time.sleep(1)
#
#inp1 = 'VOLT ' + str(V35)
#for i in range (len(inp1)) :
# serA.write(str.encode(inp1[i]))
#serA.write(str.encode('\n'))
#time.sleep(1)
#
#inp1 = 'OUTP ON'
#for i in range (len(inp1)) :
# serA.write(str.encode(inp1[i]))
#serA.write(str.encode('\n'))
#time.sleep(1)
#
#serA.close()
#
#print ('VOLTAGE --> ' + str(V35) + 'V! RUNNING MURAY...\n\n')

V_old = str(V35)
V_new = str(V35+V18)

cursor = dbELMB.cursor()
sql = "INSERT INTO Temperature (id, T_bath, P_bath, T_ext, H_ext, Hp, T_Ch01, ..., T_Ch24, TimeS)
VALUES (" + str(ID) + ", " + T_bath + ", " + P_bath + ", " + T_ext + ", " + H_ext + ", " + Hp + ", " +
str(T_ch00) + ", " + ... + ", " + str(T_ch23) + ", " + TimeS + ")"
cursor.execute(sql)
cursor.close()
dbELMB.commit()

cursor = dbELMB.cursor()
sql = "INSERT INTO Voltages (id, T_ext, T_ref, TimeS, V_old, V_new)
VALUES (" + str(ID) + ", " + T_ext + ", " + T_ref + ", " + TimeS + ", " + V_old + ", " + V_new + ")"
cursor.execute(sql)
cursor.close()
dbELMB.commit()

print ('-----\n')
cont = cont + 1
print ("Current measure : ", cont, "\n")
# args = ['./MURAY', 'DTC/Configuration_OR32_Vfollower.dtc']
args = ['./MURAY', 'DTC/Configuration_OR32_ADC_Vfollower.dtc']
try :
subprocess.call(args)
except :
print ('*** Waiting System Reboot...')
time.sleep(120)
print ('--> Ready to go!')
serJ.open()

```

2 SIMULAZIONEDETECTORMOD.CPP

```

#include <vector>
#include <utility>
#include <iostream>
#include <stdio.h>
#include <math.h>
#include "TMath.h"
#include "TRandom.h"
#include "TRandom3.h"
#include "TH2D.h"
#include "TH1D.h"
#include "TF1.h"
#include "TFile.h"
#include "TTree.h"

using namespace std;

const double plane_length = 1.0725;
const double vlux = 3*pow(10,8);
const double vFibra = vlux*0.5;
const double res = 0;
const double resScintFibra = 700*pow(10,-12);
const double off = 80*pow(10,-9);
const double Doff = 5*pow(10,-9);
const double resTDC = 600*pow(10,-12);
const double espanTemporale = 20;

int getStrip(double hit){
    double mezzaStrip = 0.0165;
    int half = (int)(hit/mezzaStrip) + 1;
    double strip_avanti_pos = half*mezzaStrip;
    double strip_dietro_pos = (half-1)*mezzaStrip;

    double distAvanti = fabs(hit-strip_avanti_pos);
    double distDietro = fabs(hit-strip_dietro_pos);
    int strip;
    if(distAvanti<distDietro) strip = half;
    else strip = half-1;
    if(strip == 0) strip = 1;
    if(strip == 65) strip = 64;
    return strip;
}

int getScheda(double hit, int view, int plane){
    int scheda = 9999;
    double halfPlane = plane_length*0.5;
    if(view == 1 && plane == 1)scheda = (hit < halfPlane)? 7: 3;
    if(view == 2 && plane == 1)scheda = (hit < halfPlane)? 13: 15;

    if(view == 1 && plane == 2)scheda = (hit < halfPlane)? 11: 4;
    if(view == 2 && plane == 2)scheda = (hit < halfPlane)? 5: 6;

    if(view == 1 && plane == 3)scheda = (hit < halfPlane)? 9: 8;
    if(view == 2 && plane == 3)scheda = (hit < halfPlane)? 12:2;

    return scheda;
}

double getTime(double hit){
    double time = -999.;
    time = (plane_length-hit)/vFibra;
    return time;
}

double getTimeExp(double dt){
    double clock = 4*pow(10,-9);
    double texp = dt*espanTemporale/clock;
    return texp;
}

int getMaxIdx(vector<double> vec){//mi da l'indice del minimo
    int indice = 0;
    double max = vec[0];
    int size = vec.size();
    for (int i = 1; i<size; i++){
        if(vec[i]>= max){
            max = vec[i];
            indice = i;
        }
    }
    return indice;
}

int main(int argc, char * argv[]){
    int oo;
    char* endPtr;

```

```

int n = 1;
while ((oo = getopt(argc, argv, "n:h")) != EOF) {
    switch(oo) {
        case 'n':
            n = strtoul(optarg, &endPtr, 10);
            break;
        case 'h':
            cout << " -n : 10^n (default n = 6)" << endl;
            break;
        default:
            break;
    }
}
const double factor = 180/TMath::Pi();

int NposGen = pow(10,n) ;//numero di eventi generati
int event = 0;
int nEvt_ok = 0;
int nEvt_okFlat = 0;
cout << "Genero 10^" << n << " eventi" << endl;
const double pos_min = 0.;
const double pos_max = 1.0725;
const double dz = 1.03;

double sum = 0;
double rho = 0;
const double duepi = 2*TMath::Pi();
const double pimez = TMath::Pi()/2;
const double cento = (100./180.)*TMath::Pi();
TFile * pdfFile = new TFile("PDFtheta.root");
TH1D * pdfT = (TH1D*)pdfFile->Get("pdfTheta");
TFile * rootFile = new TFile("simulazioneDetector.root", "RECREATE");
TTree * Tree = new TTree("tree", "Analisi t_exp");
double thex, they;
int texup, teyup, texdw, teydw;
int texup_X, teyup_Y, texdw_X, teydw_Y;
double xup, xdwn, yup, ydwn, zup, zdwn;
int sxup, sxdw, syup, sydw;
int albedo;

Tree->Branch("sxup", &sxup, "sxup/I");
Tree->Branch("syup", &syup, "syup/I");
Tree->Branch("sxdw", &sxdw, "sxdw/I");
Tree->Branch("sydw", &sydw, "sydw/I");
Tree->Branch("texup", &texup, "texup/I");
Tree->Branch("teyup", &teyup, "teyup/I");
Tree->Branch("texdw", &texdw, "texdw/I");
Tree->Branch("teydw", &teydw, "teydw/I");

Tree->Branch("texup_X", &texup_X, "texup_X/I");
Tree->Branch("texdw_X", &texdw_X, "texdw_X/I");
Tree->Branch("teyup_Y", &teyup_Y, "teyup_Y/I");
Tree->Branch("teydw_Y", &teydw_Y, "teydw_Y/I");

Tree->Branch("thex", &thex, "thex/D");
Tree->Branch("they", &they, "they/D");
Tree->Branch("xup", &xup, "xup/D");
Tree->Branch("xdwn", &xdwn, "xdwn/D");
Tree->Branch("yup", &yup, "yup/D");
Tree->Branch("ydwn", &ydwn, "ydwn/D");
Tree->Branch("zup", &zup, "zup/D");
Tree->Branch("zdwn", &zdwn, "zdwn/D");

Tree->Branch("albedo", &albedo, "albedo/I");

TH1D * histoTheta = new TH1D("histoThetaGen", "Theta generated", 100, 0., cento);
TH1D * histoThetaReco = new TH1D("histoThetaReco", "ThetaReco distribution", 100, 0., cento);
TH1D * histoPhi = new TH1D("histoPhiGen", "Phi generated", 180, 0, duepi);
TH1D * histoPhiReco = new TH1D("histoPhiReco", "PhiReco Distribution", 180, 0, duepi);

TRandom3 * gen = new TRandom3(0);
double xp, yp, xhit, yhit;
double xp_gen, yp_gen, xhit_gen, yhit_gen;
int schedaxtop, schedaytop;
int schedaxdw, schedaydw;
double phiGen;
double thetaGen;
double txtop, tytop;
double txdw, tydw;
double txtop_gen, tytop_gen;
double txdw_gen, tydw_gen;
double timeScXup, timeScYup, timeScXdw, timeScYdw;
for(int i = 0; i < NposGen; i++){
    if(!(event%100000)) cout << event << endl;
    event++;

    xp_gen = gen->Rndm()* 1.0725;
    yp_gen = gen->Rndm()* 1.0725;
    xp = gen->Gaus(xp_gen, res);

```

```

yp = gen->Gaus(yp_gen,res);

thetaGen = pdfT->GetRandom();
histoTheta->Fill(thetaGen);
phiGen = gen->Rndm()*duepi;
histoPhi->Fill(phiGen);

rho = dz/sin(thetaGen)/sin(phiGen);
xhit_gen = xp+rho*sin(thetaGen)*cos(phiGen);//posizione X sul secondo piano
yhit_gen = yp+rho*cos(thetaGen);//posizione Y sul secondo piano
xhit = gen->Gaus(xhit_gen,res);
yhit = gen->Gaus(yhit_gen,res);

if((xhit<= pos_max) && (yhit<= pos_max) && (xhit>= pos_min) && (yhit>= pos_min)){

    nEvt_ok++;

    double dx = xp - xhit;
    double dy = yp - yhit;
    double rho = TMath::Sqrt(dx*dx + dy*dy + dz*dz);
    double theta;
    if(dy>=0) theta = TMath::ACos(dy/rho);
    else theta = TMath::ACos(-dy/rho);

    double phi;
    if(dy>0){
if(dx>0) phi = TMath::ATan(dz/dx);
if(dx<0) phi = TMath::Pi()-TMath::ATan(dz/-dx);
    }else{
if(dx>0) phi = duepi- TMath::ATan(dz/dx);
if(dx<0) phi = TMath::Pi()+TMath::ATan(dz/-dx);
    }
    double tx,ty;

tx = atan(dx/dz)*180/TMath::Pi();
ty = atan(dy/dz)*180/TMath::Pi();
histoPhiReco->Fill(phi);
histoThetaReco->Fill(theta);
tXtop_gen = getTime(yp);
tYtop_gen = getTime(xp);
tXdw_gen = getTime(yhit);
tYdw_gen = getTime(xhit);
tXtop = gen->Gaus(tXtop_gen,resScintFibra);
tYtop = gen->Gaus(tYtop_gen,resScintFibra);
tXdw = gen->Gaus(tXdw_gen,resScintFibra);
tYdw = gen->Gaus(tYdw_gen,resScintFibra);

//Mu Back-Forw o Forw-Back
double tof = rho/vlux;
bool FBorBF = (gen->Rndm())<0.5)? true: false;

if(FBorBF){
    tXdw += tof;
    tYdw += tof;
    albedo = 0;
}
else{
    tXtop += tof;
    tYtop += tof;
    albedo = 1;
}

    vector<double> tempi;
    tempi.push_back(tXtop);
    tempi.push_back(tYtop);
    tempi.push_back(tXdw);
    tempi.push_back(tYdw);
    vector<double> tempi_vistaX;
    tempi_vistaX.push_back(tXtop);
    tempi_vistaX.push_back(tXdw);
    vector<double> tempi_vistaY;
    tempi_vistaY.push_back(tYtop);
    tempi_vistaY.push_back(tYdw);

    int indMaxT = getMaxIdx(tempi);
    double trigger = tempi[indMaxT] + off;

    double dtxtop = trigger - tXtop;
    double dtytop = trigger - tYtop;
    double dtxdw = trigger - tXdw;
    double dtydw = trigger - tYdw;
    dtxtop = gen->Gaus(dtxtop, resTDC);
    dtytop = gen->Gaus(dtytop, resTDC);
    dtxdw = gen->Gaus(dtxdw, resTDC);
    dtydw = gen->Gaus(dtydw, resTDC);
    double texpXtop = getTimeExp(dtxtop);
    double texpYtop = getTimeExp(dtytop);
    double texpXdw = getTimeExp(dtxdw);

```

```

double texpYdw = getTimeExp(dtydw);

int indMaxTX = getMaxIdx(tempi_vistaX);
double triggerX = tempi_vistaX[indMaxTX]+ off ;
double dtxtopX = triggerX - tXtop;
double dtxdwX = triggerX - tXdw;
dtxtopX = gen->Gaus(dtxtopX, restDC);
dtxdwX = gen->Gaus(dtxdwX, restDC);
double texpXtopX = getTimeExp(dtxtopX);
double texpXdwX = getTimeExp(dtxdwX);

int indMaxTY = getMaxIdx(tempi_vistaY);
double triggerY = tempi_vistaY[indMaxTY]+ off;
double dtytopY = triggerY - tYtop;
double dtydwY = triggerY - tYdw;
if(indMaxTX == 0) dtytopY = gen->Gaus(dtytopY, restDC);
if(indMaxTX == 1) dtydwY = gen->Gaus(dtydwY, restDC);
double texpYtopY = getTimeExp(dtytopY);
double texpYdwY = getTimeExp(dtydwY);

schedaXtop = getScheda(xp,1,1);
schedaYtop = getScheda(yp,2,1);
schedaXdw = getScheda(xhit,1,3);
schedaYdw = getScheda(yhit,2,3);

sxup = schedaxtop;
syup = schedaytop;
sxdw = schedaxdw;
sydw = schedaydw;
xup = xp;
yup = yp;
xdw = xhit;
ydw = yhit;
zup = 0;
zdw = 1.03;
thex= tx;
they= ty;
texup = texpXtop;
teyup = texpYtop;
texdw = texpXdw;
teydw = texpYdw;
texup_X = texpXtopX;
texdw_X = texpXdwX;
teyup_Y = texpYtopY;
teydw_Y = texpYdwY;
Tree->Fill();
}

}

rootFile->Write();
rootFile->Close();

return 0;
}

```

3 MUBOTIRQ.C

```

#include <stdio.h>
#include <string.h>
#include <errno.h>
#include <stdlib.h>
#include <fcntl.h>
#include <time.h>
#include <sys/mman.h>
#include <unistd.h>
#include <sys/time.h>
#include <pthread.h>
#include "map.h"
#define PAGE_SIZE (4*1024)
#define BLOCK_SIZE (4*1024)

int mem_fd;
void *gpio_map;
#define BCM2708_PERI_BASE 0x20000000
#define GPIO_BASE (BCM2708_PERI_BASE + 0x2000000)

volatile unsigned *gpio;

#define INP_GPIO(g) *(gpio+((g)/10)) &= ~(7<<(((g)%10)*3))
#define OUT_GPIO(g) *(gpio+((g)/10)) |= (1<<(((g)%10)*3))
#define SET_GPIO_ALT(g,a) *(gpio+(((g)/10))) |= (((a)<=3?(a)+4:(a)==4?3:2)<<(((g)%10)*3))

#define GPIO_LEV *(gpio+13)

#define GPIO_SET *(gpio+7)
#define GPIO_CLR *(gpio+10)

struct arg {
    unsigned int *buffer;
    int size_buffer;
    int n;
};
typedef struct arg arg;

void setup_io();
void ciclo_clock();
void delay_clock(int delay);
void set_pin_output(unsigned short pin);
unsigned int read_easy(void);
unsigned int trig(unsigned short pin);
void send_word(int GPIOpin, unsigned short word_to_send);
void reset();
void* fileDownload(void *ptr);

char *time_stamp(){

char *timestamp = (char *)malloc(sizeof(char) * 16);
time_t ltime;
ltime=time(NULL);
struct tm *tm;
tm=localtime(&ltime);

printf(timestamp,"%04d%02d%02d%02d%02d", tm->tm_year+1900, tm->tm_mon,
tm->tm_mday, tm->tm_hour, tm->tm_min, tm->tm_sec);
return timestamp;
}

static volatile int thrdTot = 10;
pthread_t tid;

FILE *f;

int main (void)
{
setup_io();
set_pin_output(DLAY_CLK);
set_pin_output(READ_PIN);
set_pin_output(DTK);
GPIO_CLR = 1 << READ_PIN;
set_pin_output(CHPSEL);
GPIO_CLR = 1 << CHPSEL;
set_pin_output(MOSI);
send_word(MOSI, CMD_CTRLWD);
send_word(MOSI, CMD_RUN);
GPIO_SET =1 <<CHPSEL;
GPIO_SET =1 <<READ_PIN;
set_pin_output(START_FIFO);
INP_GPIO(MISO);

int gotOne22, gotOne24, pin, i, k, kk;
int myCounter22, myCounter24, size_buff;
int err[thrdTot];
int tr = 0;
int count = 0;

```

```

unsigned int *temp;
unsigned int **buff = (unsigned int **) malloc(thrdTot *sizeof(unsigned int));

kk = 0;
k = 0;

for (;;) {
gotOne22 = 0 ;
size_buff = 0;
buff[tr] = (unsigned int*) malloc(sizeof(unsigned int));
for (;;) {
if (trig(TRG_IRQ) == 1) {
k++;
GPIO_CLR = 1 << READ_PIN;
GPIO_CLR = 1 << CHPSEL;
send_word(MOSI, CMD_CTRLWD);
send_word(MOSI, CMD_DIAG);
delay_clock(500);
send_word(MOSI, CMD_EASY);
send_word(MOSI, CMD_READ);
GPIO_SET =1 <<CHPSEL;
GPIO_SET =1 <<READ_PIN;

for(i=0;i<4; i++)
GPIO_SET = 1 << START_FIFO;
GPIO_CLR = 1 << START_FIFO;
gotOne24 = 0 ;

for (;;) {
if (trig(FIFO_READY) == 1) {
buff[tr][size_buff]=read_easy();
++gotOne24;
}
if (gotOne24 != 0)
break ;
}
temp = realloc(buff[tr], (2*size_buff+1)*sizeof(unsigned int));
if (temp != NULL)
buff[tr] = temp;
++size_buff;
gotOne24 = 0;
for (;;) {
buff[tr][size_buff]=read_easy();
temp = realloc(buff[tr], (2*size_buff+1)*sizeof(unsigned int));
if (temp != NULL)
buff[tr] = temp;
++size_buff;
if (trig(FIFO_READY) == 0) {
++gotOne24;
}
if (gotOne24 != 0)
break ;
}
++count;
err[tr] = pthread_create(&(tid), NULL, &fileDownload, &(arg){buff[tr], size_buff-1, 1});
pthread_join(tid,NULL);
if (err[tr] != 0)
printf("\nCan't save datas creating thread :[%s]", strerror(err[tr]));
else {
tr++;
if (tr > thrdTot-1) tr = 0;
}
GPIO_CLR = 1 << READ_PIN;
GPIO_CLR = 1 << CHPSEL;
send_word(MOSI, CMD_CLR);
send_word(MOSI, CMD_CTRLWD);
send_word(MOSI, CMD_RUN);
GPIO_SET =1 <<CHPSEL;
GPIO_SET =1 <<READ_PIN;
++gotOne22;
kk++;
}

if (gotOne22 != 0)
break ;
}
if (kk >= 100000)
break;
}
pthread_exit(NULL);
return 0 ;

}

void set_pin_output(unsigned short pin)
{
INP_GPIO(pin);
OUT_GPIO(pin);
}

unsigned int read_easy()

```

```

{
    int i;
    unsigned int buffer=0;
    unsigned int value;
    unsigned char pin_value ;

    for(i=0; i<4; i++)
GPIO_SET = 1 << DTK;
GPIO_CLR = 1 << DTK;
GPIO_CLR = 1 << CLK;
    for (i = 31; i>=0; i--)
        {
            ciclo_clock();
            value = GPIO_LEV;
            pin_value = ((value & (1 << MISO)) != 0);
            buffer|=((pin_value&1)<<i);
        }
    return(buffer);
}

void setup_io()
{
    if ((mem_fd = open("/dev/mem", O_RDWR|O_SYNC) ) < 0) {
        printf("Error no /dev/mem \n");
        exit(-1);
    }

    /* mmap GPIO */
    gpio_map = mmap(
        NULL,
        BLOCK_SIZE,
        PROT_READ|PROT_WRITE,
        MAP_SHARED,
        mem_fd,
        GPIO_BASE
    );

    close(mem_fd);

    if (gpio_map == MAP_FAILED) {
        printf("mmap error %d\n", (int)gpio_map);
        exit(-1);
    }
    gpio = (volatile unsigned *)gpio_map;
}

void ciclo_clock() {
    GPIO_SET = 1<<CLK;
    GPIO_SET = 1<<CLK;
    GPIO_CLR = 1<<CLK;
}

void send_word(int GPIOpin, unsigned short word_to_send) {

int bit[16];
int i = 0;
int modulo;
int quoziente;

for (i=0; i<16; i++)
bit[15-i] = ((word_to_send & 1<<i)>>i);

GPIO_CLR = 1<<GPIOpin; //DOpening

for (i=0; i<16; i++) {
switch (bit[i]) {
case 0:
GPIO_CLR = 1<<GPIOpin;
break;
default :
GPIO_SET = 1<<GPIOpin;
break;
}
}
ciclo_clock();
}

GPIO_CLR = 1<<GPIOpin;
}

void reset() {
/* Reset board */
set_pin_output(RST);
GPIO_CLR = 1 << RST;
GPIO_SET = 1 << RST;
GPIO_SET = 1 << RST;
GPIO_CLR = 1 << RST;
GPIO_CLR = 1 << DTK;
}

void delay_clock(int delay) {

```

```

int j;
for (j = 0; j < delay; j++) {
GPIO_SET = 1<<DLAY_CLK;
GPIO_CLR = 1<<DLAY_CLK;
}

}

unsigned int trig(unsigned short pin)
{
    unsigned int value;
    unsigned char pin_value ;

    INP_GPIO(pin);
    value = GPIO_LEV;
    pin_value = ((value & (1 << pin)) != 0);
    //GPIO_SET = 1 << CHPSEL;
    return(pin_value);
}

void* fileDownload(void *ptr)
{
pthread_t id = pthread_self();

char name[20];
int i;
arg *x = ptr;
sprintf(name, "slaveDatas%d", x->n);

    f = fopen(name, "a+");

while (i <= x->size_buffer) {
fprintf(f, "%x\t", x->buffer[i]);
++i;
}
fprintf(f, "\n");
fclose(f);
return NULL;
}

```

4 MAP.H

```

#define MISO 9
#define MOSI 10
#define CHPSEL 7
#define READ_PIN 25
#define START_FIFO 18

#define RST 8
#define CLK 11
#define DLAY_CLK 4
#define ACK 23
#define FIFO_READY 24
#define DTK 17
#define TRG_IRQ 22

// Command words
#define CMD_CLR 0x000D
#define CMD_CTRLWD 0x000E
#define CMD_MUX0 0x0001
#define CMD_MUX1 0x0002
#define CMD_MUX2 0x0003
#define CMD_MUX3 0x0004
#define CMD_MUX4 0x0005
#define CMD_EASY 0x000B
#define CMD_RST_RR 0x0160
#define CMD_RST_PR 0x0240
#define CMD_RST_SCR 0x0260

#define CMD_RUN 0x0001
#define CMD_DIAG 0x0000
#define CMD_READ 0x00C0

typedef struct command_std
{
    unsigned short cmd;
    unsigned short data;
}cmd_std;

typedef struct command_easyrock
{
    unsigned short cmd;
    unsigned short *data;
}cmd_easy;

```

BIBLIOGRAPHY

- [1] Antonioli P., Ghetti C., Korolkova E.V., Kudryavtsev V.A., Sartorelli G., (1997). A Three-Dimensional Code for Muon Propagation Through the Rock: MUSIC, *arXiv:hep-ph/9705408v2*
- [2] Ambrosi G. *et al.* (2011). The MU-RAY project: Volcano radiography with cosmic-ray muons, *Nucl. Instr. Methods A*, **628**, 120–123.
- [3] Ambrosino F. *et al.* (2013a). The MU-RAY experiment. An application of SiPM technology to the understanding of volcanic phenomena, *Nucl. Instr. Methods A*, **718**, 134–137.
- [4] Ambrosino F. *et al.* (2013b). The MU-RAY detector for muon radiography of volcanoes, *Nucl. Instr. Methods A*, **732**, 423–426.
- [5] Ambrosino F. *et al.* (2014). The MU-RAY project: detector technology and first data from Mt. Vesuvius, *Jour. Instr.*, **9**, C02029.
- [6] Alvarez L.W., Anderson J.A., Bedwei F.E., Burkhard J., Fakhry A., Girgis A., Goneid A., Hassan F., Iverson D., Lynch G., Miligy Z., Mousaa A.H., Sharkawi M., Yazolinio L. (1970). Search for hidden chambers in the pyramids, *Science*, **167**, 832–839.
- [7] Ave M., Vazquez R.A., Zas E., Hinton J.A., Watson A.A. (2000a), The rate of cosmic ray showers at large zenith angles: a step towards the detection of ultra-high energy neutrinos by the Pierre Auger Observatory, *Astroparticle Physics*, **14**, 109–120.
- [8] Ave M., Vazquez R.A., Zas E. (2000b), Modeling horizontal air showers induced by cosmic rays, *Astroparticle Physics*, **14**, 91–107.
- [9] Barrett P.H., Bollinger L.M., Cocconi G., Eisenberg Y., Greisen K. (1952). Interpretation of Cosmic-Ray Measurements Far Underground, *Rev. Modern Phys.*, **24**, 133–178.
- [10] Beringer J., *et al.* (Particle Data Group) (2012). *Phys. Rev.*, **D86**.
- [11] Beauducel F. *et al.* (2010). The MU-RAY project: Summary of the round-table discussions, *Earth Planets Space*, **62**, 2, 145–151.
- [12] Bedjidian M. *et al.* (2011). Performance of Glass Resistive Plate Chambers for a high-granularity semi-digital calorimeter, *Journ. Inst.*, **6**, P02001.
- [13] Bross A.D., Pla-Dalmau A., Spangler C.W. (1993). New fluorescent compounds for plastic scintillator applications, *Nucl. Instr. Methods A*, **325**, 168–175.
- [14] Bross A.D., Pla-Dalmau A., Mellott K.L. (2001). Low-cost extruded plastic scintillator, *Nucl. Instr. Methods A*, **466**, 482–491.
- [15] Carloganu C., Niess V., Bene S., Busato, E., Dupieux P., Fehr F., Gay P., Miallier D., Vulpescu B., Boivin P., Combaret C., Labazuy P., Laktineh I., Lenat J.-F., Mirabito L., Portal A. (2013). Towards a muon radiography of the Puy de Dôme, *Geosci. Instrum. Method.*, **2**, 55–60.

- [16] Conforti Di Lorenzo S., Callier S., Fleury J., Dulucq F., De la Taille C., Martin Chasard G., Raux L., Seguin-Moreau N. (2013). SPIROC: design and performances of a dedicated very front-end electronics for an ILC Analog Hadronic CALorimeter (AHCAL) prototype with SiPM read-out, *Journ. Inst.*, **8**, C01027.
- [17] Cronin J., Gaisser T.K., Swordy S.P. (1997). *Sci. Amer.*, **276**, 44.
- [18] De Pascale M.P. *et al.* (1993). Absolute spectrum and charge ratio of cosmic ray muons in the energy region from 0.2 GeV to 100 GeV at 600 m above sea level, *J. Geophys. Res.*, **98**, 3501–3507.
- [19] Di Fernando D. *pp* OPERA Collaboration (2008). Nuclear emulsions in the OPERA experiment, *arXiv:0812.0451v1 [physics.ins-det]*.
- [20] Eckart C., Shonka F.R. (1938). Accidental Coincidences in Counter Circuits, *Phys. Rev.*, **53**, 752–756.
- [21] Flyckt S., Marmonier C. (2002). *Photomultiplier Tubes: Principles and Application*, Photonis, Brive, France.
- [22] Fukuda T. *pp* OPERA Collaboration (2009). The Nuclear Emulsion Technology and the Analysis of the OPERA Experiment Data, *arXiv:0910.3274v1 [hep-ex]*.
- [23] Gaisser T.K. (1990). *Cosmic rays and particle physics*, Cambridge Univ. Press, Cambridge.
- [24] Gibert D., Beauducel F., Déclais Y., Lesparre N., Marteau J., Nicollin F., Tarantola A. (2010). Muon tomography: Plans for observations in the Lesser Antilles, *Earth Planets Space*, **62**, 153–165.
- [25] Golden R.L., Stephens S.A., Stochaj S.J., Webber W.R., Brunetti M.T., Codino A., Grimani C., Menichelli M., Salvatori I., De Pascale M.P. *et al.* (1995). Measurement of the energy spectra of cosmic ray electron component and protons at ground level, *J. Geophys. Res.*, **100**, 23515–23522.
- [26] Grieder P.K.F. (2001). *Cosmic rays at Earth: researcher's reference manual and data book*. Elsevier Science, Amsterdam.
- [27] Gibert D., Beauducel F., Déclais Y., Lesparre N., Marteau J., Nicollin F., Tarantola A. (2010). Muon Tomography: Plans for Observations in the Lesser Antilles, *Ear. Plan. Spa.*, **52**, 153–165.
- [28] Groom D.E., Mokhov N.V., Striganov S.I. (2001). Muon stopping power and range tables 10 MeV to 100 TeV, *Atom. Data Nucl. Data Tabl.*, **78**, 183–356.
- [29] Hansen P., Gaisser T.K., Stanev T., Sciutto S.J. (2005). Influence of the geomagnetic field and of the uncertainties in the primary spectrum on the development of the muon flux in the atmosphere, *Physical Review D*, **71**, 083012.
- [30] Hayakawa S. (1969). *Cosmic Ray Physics*, Wiley, Interscience, New York.
- [31] Hebbeker T., Timmermans C. (2002v). A compilation of high energy atmospheric muon data at sea level, *Astroparticle Physics*, **18**, 107–127.

- [32] Kedar S., Tanaka H.K.M., Naudet C.J., Jones C.E., Plaut J.P., Webb F. H. (2013). Muon radiography for exploration of Mars geology, *Geosci. Instrum. Method. Data Syst.*, **2**, 157–164.
- [33] Kudenko Y.G., Littenberg L.S., Mayatski V.A., Mineev O.V., Yershov N.V. (2001). Extruded plastic counters with WLS fiber readout, *Nucl. Instr. Methods A*, **469**, 340–346.
- [34] Kudryavtsev V.A. (2009). Muon simulation codes MUSIC and MUSUN for underground physics, *Comp. Phys. Comm.*, **180**, 339–346.
- [35] Leo W.R. (1987). *Techniques for Nuclear and Particle Physics Experiments*, Springer Verlag, Berlin, Heidelberg.
- [36] Lesparre N., Gibert D., Marteau J., Déclais Y., Carbone D., Galichet E. (2010). Geophysical muon imaging: feasibility and limits, *Geophys. J. Int.*, **183**, 1348–1361.
- [37] Lesparre N., Marteau J., Déclais Y., Gibert D., Carlus B., Nicollin F., Kergosien B. (2012a). Design and Operation of a Field Telescope for Cosmic Ray Geophysical Tomography, *Geosci. Instrum. Method. Data Syst.*, **1**, 33–42.
- [38] Lesparre N., Gibert D., Marteau J. (2012b). Bayesian Dual Inversion of Experimental Telescope Acceptance and Integrated Flux for Geophysical Muon Tomography, *Geophys. J. Int.*, **188**, 490–497, doi: 10.1111/j.1365-246X.2011.05268.x.
- [39] Lesparre N., Gibert D., Marteau J., Komorowski J.-C., Nicollin F., Coutant O. (2012c). Density Muon Radiography of La Soufrière of Guadeloupe Volcano: Comparison with Geological, Electrical Resistivity and Gravity data, *Geophys. J. Int.*, **190**, 1008–1019.
- [40] Mahon D.F. *et al.* (2013). A prototype scintillating-fibre tracker for the cosmic-ray muon tomography of legacy nuclear waste containers, *Nucl. Instr. Methods A*, **732**, 408–411.
- [41] Malmqvist L. *et al.* (1979). Theoretical studies of in-situ rock density determinations using underground cosmic-ray muon intensity measurements with application in mining geophysics, *Geophysics*, **44**, 1549–1569.
- [42] Marteau J., Gibert D., Lesparre N., Nicollin F., Noli P., Giacoppo F. (2012). Muons tomography applied to geosciences and volcanology, *Nucl. Instr. Meth. A*, **695**, 23–28.
- [43] Matsuno S., Kajino F., Kawashima Y., Kitamura T., Mitsui K., Muraki Y., Ohashi Y., Okada A., Suda T., Minorikawa Y., Kobayakawa K., Kamiya Y., Nakamura I., Takahashi T. (1984). Cosmic-ray muon spectrum up to 20 TeV at 89° zenith angle, *Phys. Rev. D*, **29**, 1–23.
- [44] Morris C.L. *et al.* (2012). Obtaining material identification with cosmic ray radiography, *AIP Advances*, **2**, 042128.
- [45] Nagamine K. (1995). Geo-tomographic observation of inner-structure of volcano with cosmic-ray muons, *J. Geography*, **104**, 998–1007.
- [46] Nagamine K. (2003). *Introductory Muon Science*, 208 pp, Cambridge University Press, Cambridge UK.

- [47] Nagamine K. *et al.* (1995). Method of probing inner-structure of geophysical substance with the horizontal cosmic-ray muons and possible application to volcanic eruption prediction, *Nucl. Instr. Meth. A*, **356**, 585–595.
- [48] Okubo S., Tanaka H.K.M. (2012). Imaging the density profile of a volcano interior with cosmic-ray muon radiography combined with classical gravimetry, *textitMeas. Sci Technol.*, **23**, 042001.
- [49] Perry J. *et al.* (2013). Imaging a nuclear reactor using cosmic ray muons, *Jou. App. Phys.*, textbf113, 184909.
- [50] Pla-Dalmau A., Bross A.D., Mellott K.L. (2001). Low-cost extruded plastic scintillator, *Nucl. Instr. Meth. A*, **466**, 482-491.
- [51] Portal A., Béné S., Boivin P., Busato E., Carloganu C., Combaret C., Dupieux P. , Fehr F. , Gay P. , Labazuy P., Laktineh I. , Lenat J.-F., Miallier D., Mirabito L., Niess V., Vulpescu B. (2012). Inner structure of the Puy de Dôme volcano: cross-comparison of geophysical models (ERT, Gravimetry, Muonic Imagery), *Geoscientific Instrum. Methods Data Systems*, **2**, 703–717.
- [52] Renker D. (2006). Geiger-mode avalanche photodiodes, history, properties and problems, *Nucl. Instr. and Meth. A*, **567**, 48–56.
- [53] Richmond P.E. (1966). The Peltier effect, *Phys. Edu.*, **1**, 145–152
- [54] Shinohara H., Tanaka H. (2012). Conduit magma convection of a rhyolitic magma: Constraints from cosmic-ray muon radiography of Iwodake, Satsuma-Iwojima volcano, Japan, *Earth and Planet. Sci. Lett.*, **349–350**, 87–97.
- [55] Tanaka H., Nagamine K., Kawamura N., Nakamura S.N., Ishida K., Shimomura K. (2001). Development of the cosmic-ray muon detection system for probing internal-structure of a volcano, *Hyperfine Interact.*, **138**, 521–526.
- [56] Tanaka H.K.M. *et al.* (2003). Development of a two-folded segmented detection system for near horizontally cosmic-ray muons to probe the internal structure of a volcano, *Nuc. Inst. Meth. A*, **507**, 657–669.
- [57] Tanaka H.K.M., Nagamine K., Nakamura S.N., Ishida K. (2005). Radiographic measurements of the internal structure of Mt. West Iwate with near horizontal cosmic ray muons and future developments, *Nucl. Instrum. Methods A*, **555**, 164–172.
- [58] Tanaka H.K.M., Nakano T., Takahashi S., Yoshida J., NiwaK. (2007a). Development of an emulsion imaging system for cosmic-ray muon radiography to explore the internal structure of a volcano, Mt. Asama, *Nuc. Instr. Meth. A*, **575**, 489–497.
- [59] Tanaka H.K.M. *et al.* (2007b). High resolution imaging in the inhomogeneous crust with cosmic-ray muon radiography: The density structure below the volcanic crater floor of Mt. Asama, Japan, *Earth Plan. Sci. Lett.*, **263**, 104–113.
- [60] Tanaka H., Uchida T., Tanaka M., Shinohara H., Taira H. (2009). Cosmic-ray muon imaging of magma in a conduit: Degassing process of Satsuma-Iwojima Volcano, Japan, *Geophys. Res. Lett.*, **36**, L01304.

- [61] Tanaka H.K.M., Uchida T., Tanaka M., Shinohara H., Taira H. (2010). Development of a portable assembly-type cosmic-ray muon module for measuring the density structure of a column of magma, *Earth Planets Space*, **62**, 119–129.
- [62] Tanaka H.K.M. (2013). Subsurface density mapping of the earth with cosmic ray muons, *Nuc. Phys. B (Proc. Suppl.)*, **243-245**, 239-248.
- [63] Tanaka H.K.M., Kusagaya T., Shinohara H. (2014). Radiographic visualization of magma dynamics in an erupting volcano, *Nature Comm.*, **5**, 3381.
- [64] Tang A., Horton-Smith G., Kudryavtsev V.A., Tonazzo A. (2006). Muon simulation for Super-Kamiokande, KamLAND, and CHOOZ, *Phys. Rev. D*, **74**, 053007.
- [65] Thomson M.G. *et al.* (1975). The production spectra of the parents of vertical cosmic ray muons, *J. Phys. G: Nucl. Phys.*, **1**, L48–L50.